Range Assisted Inertial Navigation System for Multi-Rotor Micro Aerial Vehicles

by

© Hondanaidelage C. T. Eranga Fernando

A thesis submitted to the School of Graduate Studies
in partial fulfillment of the requirements for the degree of

Doctor of Philosophy

Faculty of Engineering and Applied Science
Memorial University of Newfoundland

August 2022
St. John's, Newfoundland

Abstract

Pose estimation of multi-rotor micro-aerial vehicles (MAVs) in indoor environments is a key challenge in the development of autonomous MAV applications. The main focus of this research is to develop robust, and accurate localization systems for MAVs utilizing the least number of sensors. This research develops three range assisted inertial navigation system (RINS) designs for quadrotor MAVs. Range measurement is selected as the key measurement due to the robustness, accuracy of the emerging ranging technologies, and ease of deployment in various types of environments even under challenging conditions.

The first part of this thesis presents the development of a RINS that utilizes three or two range measurements along with the accelerometer and gyroscope measurements. The proposed RINS incorporates the effects of aerodynamic drag forces on MAV, which allows the RINS to operate without using a velocity sensor. A nonlinear observability study is carried out to evaluate the feasibility, and identify the limitations of the proposed RINS. The observability analysis is conducted based on two cases. *Case 1*: RINS with three range measurements, and *Case 2*: RINS with two range measurements. For each case, the analysis shows that the RINS is locally weakly observable for a generic trajectory. Additionally, several specific trajectories are identified that render the RINS unobservable. The unobservable directions for each unobservable trajectory are determined analytically and validated through numerical simulations. The performance of the proposed RINS during an observable trajectory is validated through experiments conducted on a quadrotor MAV.

The second part of this thesis analyzes the consistency of the error-state extended Kalman filter (EKF) implementation of the proposed two and three range assisted INS. The analysis shows that the EKF-RINS suffers from inconsistencies when the MAV is flying on the unobservable trajectories identified through the observability study. The consistency of the estimator under unobservable trajectories is improved by applying observability constraints during the estimation process. The novelty of the proposed approach is that the observability constraints are dependent on the unobservable scenarios and applied only during any unobservable trajectory. A Monte Carlo analysis is performed to validate the improvement of the localization performance of EKF-RINS achieved through selectively applying the observability constraints.

Finally, this thesis presents two RINS designs that use a single range measurement. The first design uses just the range measurement. However, the observability analysis shows that this design is unobservable under any trajectory. In order to develop a locally weakly observable trajectory, the second design incorporates heading information in addition to the single range measurement. The observability study identified several unique trajectories under which the magnetometer and single range assisted INS (M-RINS) becomes unobservable. Performance evaluation of the M-RINS and the validation of unobservable directions are carried out using numerical simulations.

I dedicate this thesis
to my baby daughter
Mirelli.

Acknowledgements

I would like to acknowledge and thank my supervisors, Dr. George Mann, Dr. Oscar De Silva, and Dr. Ray Gosine, for their support and guidance. I also express my most profound appreciation for their patience, motivation, and persistence. I would also like to thank Dr. Thumeera Wanasinghe for his immense support in and out of the academic work.

I would like to acknowledge the financial support provided by my supervisors, the Natural Science and Engineering Research Council of Canada (NSERC), and the Memorial University of Newfoundland. Without the financial support, this research would not have been possible. I would like to extend thanks to all the colleagues of the ISLab for their assistance and support. It was a privilege to have such a diverse group to work with.

I would like express my sincere gratitude my parents and siblings for their love, support, and encouragement throughout my life. Last but not least, I would like to express my most profound appreciation for my wife, Janani, for her unwavering support and for being the pillar during the ups and downs of my life.

Table of Contents

List of Tables

List of Figures

List of Abbreviations

CGR	Cayley-Gibbs-Rodriguez.
DOF	Degree of Freedom.
EKF	Error-state Extended Kalman Filter.
EKF-RINS	Error-state Extended Kalman Filter based Range assisted Inertial Navigation System.
GNSS	Global Navigation Satellite System.
IMU	Inertial Measurement Unit.
INS	Inertial Navigation System.
M-RINS	Magnetometer and Single Range assisted Inertial Navigation System.
MAE	Mean Absolute Error.
MAV	Micro Aerial Vehicle.
MEMS	Micro-electromechanical system.
NEES	Normalized Estimation Error Square.
RIEKF	Right Invariant error extended Kalman filter.
RINS	Range assisted Inertial Navigation System.

RMSE	Root Mean Square Error.
ROS	Robot Operating System.
RSS	Received Signal Strength.
SLAM	Simultaneous Localization and Mapping.
TDOA	Time difference of Arrival.
TOA	Time of Arrival.
UWB	Ultra-Wideband.
VINS	Visual-Inertial Navigation System.
VIO	Visual-Inertial Odometry.
VSLAM	Visual Simultaneous Localization and Mapping.

Chapter 1

Introduction

1.1 Research Motivation

Multi-rotor micro aerial vehicles (MAV) are rotorcrafts that generate lift using more than two rotors. Due to the vertical take-off and landing capability, high maneuverability, and ability to operate in confined environments, multi-rotor MAVs have been adapted for various indoor and outdoor applications. In practice, the payload requirement of the application is a key factor that determines the type of MAVs to use. Hexacopter and octocopter, which has six and eight rotors, respectively, are used for applications that require a high payload capacity. Quadrotor MAVs with four rotors are preferred for more general applications with small payloads. A few years back, commercially available MAVs[1] were predominantly used by enthusiasts and hobbyists for entertainment purposes. However, the MAVs have been adapted for professional and industrial applications in recent years. Some applications include aerial photography [1], aerial surveillance [2], package delivery [3,4], visual art performances [5] and infrastructure inspection [6]. Most of the MAV related applications are carried out

---

[1] In the rest of the thesis, MAV refers to the quadrotor multi-rotor micro-aerial vehicle. Otherwise, the type of vehicle will be specified.

with a skilled pilot manually controlling the MAV. This limits the broad adaptation of MAVs in applications that can benefit from their unique properties. One of the main challenges of developing autonomous MAVs is estimating accurate six DOF pose (position and orientation)[2] of the MAV.

Micro-electromechanical system (MEMS) based Inertial Measurement Unit (IMU) is a key component of any MAV, and IMU measurements are generally used to estimate the orientation of the MAV [7]. In contrast, there are various techniques to estimate the position of the MAV. Global Navigation Satellite System (GNSS) provides accurate position information and is widely used in outdoor applications [8]. However, GNSS position information becomes unreliable or sometimes unavailable in indoor or in cluttered environments. Therefore several techniques have been developed to estimate the position in GNSS denied environments.

Simultaneous Localization and Mapping (SLAM) is a widely used localization technique capable of estimating the pose and generating a map of the operating environment using various sensor readings [9]. VSLAM is a sub category of SLAM that uses vision sensors (mono cameras, stereo cameras, depth cameras) to detect features and landmarks in the environment [10]. For most of the applications, the objective is to estimate the pose of the MAV, and therefore, map building is not always necessary. A visual inertial navigation system (VINS) localizes the MAVs without generating a map of the environment. VINS incorporates vision information with the inertial measurements of the MAV obtained through the IMU [11].

One of the main drawbacks of the aforementioned vision based localization techniques is error accumulation, leading to drift in the estimation over time. Existing drift minimization techniques are computationally expensive and require additional computational resources on top of the high processing power required to perform local-

---

[2] In this thesis, the term *pose* is used to represent the 3D position and the orientation of the MAV.

ization in real-time. Furthermore, vision based techniques require detectable features to perform localization. Some operating environments may lack detectable features, and therefore the localization performance might be impacted.

On the other hand, range based localization techniques provide global position estimates and do not suffer from drift over time. These techniques are less computationally demanding and, therefore, can be implemented without significant computational overhead. Additionally, depending on the ranging technology, range based localization can be used in a wide variety of environments [12]. Range based localization can be categorized into two categories range only localization and range assisted localization. As the name suggests, range only localization uses only the range measurements and requires a minimum of four distinct range measurements to calculate the position of the MAV [13]. Range assisted localization techniques utilize other sensor measurements in addition to the range measurements to estimate the pose of the MAV [14].

Despite having additional information, almost all of the range assisted localization studies carried out for MAVs have used four or more range measurements. Requiring four or more distinct range measurements at any given time can be challenging in practical applications. For example, deploying sufficient range sensors to cover a building while maintaining minimum visibility of four range sensors at all times can be challenging. If contingencies are taken to overcome sensor failures or dynamic occlusion of sensors, the number of sensors required would increase significantly.

The few studies that have used less than four range measurements have used IMU, velocity, and height measurements to aid in the estimation process. The performance of the height and velocity sensors available for MAVs are highly dependent on the operating conditions. Optical flow and visual inertial odometry (VIO) are two key velocity measurement techniques used for MAV applications. The optical flow technique provides velocity measurements based on the apparent motion in a visual scene seen by the sensor. VIO techniques visual features and inertial measurements to estimate the velocity of the MAV. Both techniques require detectable features, and optical flow sensors require a structured surface to provide accurate velocity measurements. Similarly, ultrasound and time-of-flight height sensors require a structured environment to produce accurate height measurements.

Hence, developing a range-assisted localization technique for MAVs that use only range and IMU measurements and require fewer range measurements can reduce the total number of range sensors needed and overcome the limitations of the velocity and height measurements.

1.2 Thesis Problem Statement

The main focus of this research study is to develop a range assisted inertial navigation system (RINS) for MAVs using IMU and less than four range measurements. Special attention is given to the unique drag forces acting on the multi-rotor MAV during flight and incorporated into the development of the RINS [15]. Throughout this research study, it is assumed that there is no wind in the operating environment.

1.2.1 Problem 1: RINS with Three and Two Range Measurements

An inertial navigation system (INS) tracks a robot's pose using the accelerometer and gyroscope measurements relative to an initial pose and velocity. The orientation is calculated by integrating the angular velocity measured by the gyroscope. The linear velocity is calculated by integrating the linear acceleration measured by the accelerometer and the position by integrating the velocity. However, the calculated pose can drift over time due to the noise in the measurements. Instead of integrating the measurements, in practical application, filtering techniques such as Kalman filtering are used to estimate the pose of the robot. Attitude estimation by fusing accelerometer and gyroscope measurements has shown more accuracy over the simple integration [7]. However, additional information is required to obtain an accurate position estimate.

It is straightforward to show that it is possible to obtain a unique solution for the robot's position with a minimum of four range measurements to known locations. Hence, this information can be used to calculate the position and incorporate it in the INS as a loosely coupled estimator [16] or use the range information directly in a tightly coupled INS [17]. However, there is no unique solution for the position with three or two range measurements.

The first problem this thesis address focuses on developing a RINS for MAVs with three and two range measurements. The designed RINS does not use any additional sensors other than range and IMU sensors. Additionally, this design incorporates the unique drag force dynamics of the MAVs into the mechanization equations of the RINS. Furthermore, a detailed observability study is carried out to determine the feasibility and limitations of the proposed RINS.To the best of the author's knowledge, no other study has developed a RINS of this nature for multi-rotor aerial vehicles.

Experiments are conducted to validate the performance of the proposed three and two range assisted INS. The experimental setup consists of an AscTec Hummingbird quadrotor MAV flying in an arena populated by decaWave DWM1001 modules. IMU data are obtained using the onboard IMU of the Hummingbird MAV, and a DWM1001 module (*Tag*) on the MAV is used to measure the distance between the DWM1001 modules (*Anchors*) placed at known locations in the arena. The estimated pose information is compared with the ground truth pose information obtained through a

Mocap motion capture system.

1.2.2 Problem 2: Consistency Improvement of the Three and Two Range Assisted INS

The proposed RINS with three and two range measurements, is implemented using the error-state extended Kalman filter (EKF[3]) formulation. A key factor when selecting the estimation technique was the computational efficiency of the algorithm. Compared to the optimization based techniques, filtering techniques are computationally efficient, so filtering is chosen to implement the RINS. Similarly, the EKF formulation is chosen over other nonlinear filtering techniques such as the unscented Kalman filter and Cubature Kalman filter due to the computational efficiency in the EKF implementation. [18, 19].

Based on the observability analysis carried out for the developed RINS with three and two range measurements, the RINS is locally weakly observable during a generic trajectory. However, there are certain trajectories that render the RINS unobservable. Even though the number of unobservable trajectories is few, they can occur in practical applications. In such instances, the EKF implementation of the RINS (EKF-RINS) can become inconsistent. It is crucial to determine and address inconsistencies to achieve better performance under unobservable conditions.

A consistent estimator has zero-mean estimation errors, and the estimated error covariances closely resemble the true error covariances calculated by the filter [20]. For nonlinear systems, there are several potential sources of inconsistency. One such source is the mismatch between the unobservable modes of the actual nonlinear system and the linearized model used for the estimator implementation [21].

Consistency of VSLAM and VINS has been studied extensively in the litera-

---

[3] Through out the thesis EKF stands for the error-state extended Kalman filter.

ture [22,23]. 3-D global position and the yaw angle are the four unobservable states, also known as unobservable modes of VSLAM and VINS. These unobservable modes are independent of the trajectory and, therefore, always present. Hence, consistency improvement techniques developed are applied throughout the trajectory. However, in the proposed RINS, there are several trajectories where few states become unobservable. These unobservable states are temporary and are dependent on the trajectory. This study analyzes the consistency of the EKF-RINS, determines the consistency rules, and applies them to improve the consistency of the EKF-RINS. To the best of the author's knowledge, this is the first study that analyzes the consistency of the EKF-RINS with three and two range measurements.

1.2.3 Problem 3: RINS with One Range Measurement

The third challenge addressed in this thesis is localizing the MAV using a single range measurement to a known location. Single range based localization has been studied in underwater robotics applications and in relative localization applications.

In general underwater robotics applications use multiple range measurements to localize autonomous underwater vehicles (AUVs). However, few studies have used one range sensor to obtain range measurements between two AUVs or an AUV, and a surface vehicle [24–27]. These studies have used complementary sensors such as depth sensors and Doppler Velocity Logs (DVL) to obtain additional information on the AUVs' state. Authors in [28] have proposed a leader-follower MAV system that uses velocity and heading sensors in addition to the range sensor and IMU.

Measuring the velocity of a MAV is challenging. Motion capture system (MCS) is a widely used external system capable of providing velocity measurements of MAVs [29]. Due to the high price tag of MCS, it is generally used in laboratory spaces to obtain ground truth data. Since MCS also provides position and orientation information, there is no need to develop a separate system to estimate the pose of the MAV. Another popular approach of measuring the velocity of MAVs is using an onboard optical flow sensor [30], but the performance of the optical flow sensors degrades when used over unstructured surfaces.

The single range assisted INS presented in this thesis does not require a velocity measurement of the MAV. Compared to the two and three range based RINS, the only additional measurement used in single range assisted INS is the heading of the MAV. To the best of the author's knowledge, no other study has developed a single range assisted INS, incorporating the unique dynamics of the MAV. The feasibility and the limitations of the proposed RINS with single range measurement are determined through an observability study, and validated using numerical simulations.

1.3 Research Objective and Contributions

The main goal of this research is to develop a range assisted INS to estimate the pose of the quadrotor MAV with less than four range measurements. In order to achieve this research goal following objectives are identified.

Objective 1: Development of a three and two range assisted inertial navigation system (RINS) for MAVs.

- Contribution 1: Designing a RINS for MAVs, which incorporates the unique dynamics of the MAVs, and can operate with three or two range measurements to known locations.

- Contribution 2: Conducting an observability analysis of the RINS with three and two range measurements and identifying the unobservable trajectories and corresponding unobservable directions.

Objective 2: Development of a trajectory dependent observability constrained RINS with three and two range measurements.

- Contribution 1: Analyzing the consistency of the EKF implementation of the proposed RINS under unobservable trajectories.
- Contribution 2: Determining the observability consistency rules and developing a trajectory based observability constrained RINS.

Objective 3: Development of a single range assisted inertial navigation system (RINS) for MAVs.

- Contribution 1: Developing a RINS for MAVs using a single range measurement.
- Contribution 2: Developing a RINS for MAVs incorporating heading and single range measurement.
- Contribution 3: Conducting an observability study of the proposed single range assisted INS in determining the feasibility and identifying the unobservable trajectories and unobservable directions.

1.4 Organization of the Thesis

This thesis is organized as follows.

- **Chapter 1 - Introduction**: This chapter provides an overview of the research motivation, highlights the problem statements, and outlines the objectives and contributions of this thesis.
- **Chapter 2 - Literature Review**: This chapter presents the literature review in the areas of state estimation, range based localization, and observability analysis.

- **Chapter 3 - Three and Two Range assisted Inertial Navigation System**: This chapter relates to the objective 1 of this thesis. The chapter presents the formulation of the three and two range assisted inertial navigation system and EKF implementation of the RINS. A detailed observability analysis of the proposed RINS is presented, and unobservable trajectories along with unobservable modes are identified. Simulation and experimental studies are carried out to validate the performance of the proposed RINS.

- **Chapter 4 - Observability Constrained Three and Two Range assisted Inertial Navigation System**: This chapter relates to the objective 2 of this thesis. A consistency analysis is carried out for the three and two range assisted INS proposed in Chapter 3. Consistency rules are determined for the unobservable trajectories of the RINS and implemented a observability constrained RINS with three and two range measurements. Simulation results are presented to show the consistency improvement.

- **Chapter 5 - Single Range assisted Inertial Navigation System**: This chapter relates to the objective 3 of this thesis. This chapter presents the design of EKF-RINS with single range and heading measurements. An observability analysis is carried out to identify the limitations of the single range assisted INS. The performance of the RINS is validated through simulation studies.

- **Chapter 6 - Summary and Future Work**: This chapter concludes the thesis and presents the applicability of the proposed RINS for MAVs. Also, it presents possible future research directions.

Chapter 2

Literature Review

2.1 Dynamics and Control of MAVs

In recent years usage of multi-rotor micro aerial vehicles has increased significantly. Due to the vertical take-off and land landing capabilities, simple construction, and high maneuverability, multi-rotor MAVs are being adapted for indoor applications and applications which require high agility [1, 2, 4]. Quadrotor micro-aerial vehicles have four thrust generating rotors, producing torques for maneuvering in the 3-D space. They are the most used MAV for applications with small to medium payload requirements.

The earliest studies on the quadrotor MAVs focused on the basic dynamics and controls of the MAVs [31, 32]. MAV is an underactuated system with four actuators to control 6 degrees of freedom (DOF). Hence, the MAV is modeled as a 6 DOF rigid body, and four control variables are selected to develop the attitude control algorithms. Earlier studies have chosen thrust and orientation as the four control variables [33], whereas more recent studies have selected thrust and angular velocities of the MAV [29].

2.1.1 Aerodynamic Drag Forces Acting on MAV

The dynamics of the MAV are more complex than the 6DOF rigid body dynamics due to various aerodynamic forces acting on the MAV. The study carried out by Derafa et al. in [34] is one of the first studies that have incorporated the aerodynamic forces in modeling the MAV. They have modeled the aerodynamic drag as a force proportional to the velocity of the MAV with respect to the inertial frame. In [35], authors have studied how the thrust variations and blade flapping affect the dynamics of the MAV. The translational flight of a propeller through the air causes the blade to flap. The advancing rotor blade experiences an increase in the effective velocity relative to the air, increasing the lift. Similarly, the retreating blade experiences a reduction in lift. The resulting force is parallel to the propeller plane of the MAV. A more detailed study on the aerodynamic forces acting on the MAV is carried out in [15], where the authors have analyzed blade flapping, induced drag, translational drag, profile drag, and parasitic drag. All the drag forces except for translational and parasitic drags have a linear relationship with the translational speed of the MAV. Among these drag forces, blade flapping drag is the most significant contributor to the drag force[1].

Studies have shown that incorporating the drag forces into the estimator formulation has improved the performance of the estimators. Few of them are listed here. Leishman et al. in [36] have shown that the estimator which uses the drag force model[2] outperforms the standard attitude heading reference system (AHRS) and provides the velocity of the MAV. A similar study by Abeywardena et al., in [37] showed that a drift-free velocity estimate could be obtained using the drag force model. One key takeaway from these studies is that incorporating the drag force model enables the estimator to estimate the velocity of the MAV without requiring a dedicated veloc-

---

[1] From this point onwards the *drag force* refers to the blade flapping and other drag-like forces that are proportional to the translational velocity of the MAV.

[2] Dynamic model of MAV incorporating the aerodynamic drag forces

ity sensor. This is an advantage, especially for MAV applications, where measuring velocities is challenging.

2.2 MAV Localization

Localization is one of the main challenges in developing autonomous, semi-autonomous MAV applications. A plethora of studies has addressed the localization problem using various approaches. Localizing in an outdoor environment is straightforward due to the availability of GNSS. GNSS provides absolute position and velocity information of the MAV at a relatively lower rate (1Hz - 10Hz). Several studies have fused GNSS with other sensors such as IMU and vision to improve the accuracy of the localization [8, 38, 39]. GNSS is unreliable or sometimes unavailable in indoor and cluttered environments despite good performance in outdoor environments. Therefore, other techniques have been proposed for localizing MAVs in GNSS-denied environments.

Vision based localization techniques are one of the widely studied localization techniques for GNSS-denied environments. One such technique is Visual SLAM, and it aims to construct a map of the environment and simultaneously estimate the global position of the MAV using visual features of the environment. VSLAM algorithms are developed using different types of camera configurations such as single camera [40, 41], stereo cameras [42, 43], and RGB-D cameras [10, 44]. Another popular approach of vision based localization is VINS. Vision information is fused with IMU and other onboard sensors to estimate the pose of the MAV [11, 45].One main drawback of the aforementioned vision based techniques is the drift in the estimation over time due to error accumulation. The drift can be minimized using loop closure [46], global pose graph optimization [11] or relocalization [47] techniques.

2.2.1 Range Based Localization

Compared to vision based localization techniques, range based localization techniques are computationally efficient. Since the vision based techniques require features in the image or video, the operating environment should have detectable features. Additionally, the range based localization techniques do not suffer from drift in the estimates. Therefore range based localization can be an attractive alternative to vision based localization techniques. Range based localization techniques can be broadly divided into two categories, range only localization and range assisted localization. As the name suggests, range only localization uses only range measurements. Whereas range assisted localization makes use of additional sensors to aid in localization.

There are various sensor technologies that are capable of providing distance measurement between the robot and the environment, and few of them are WiFi, cellular, ultrasonic, and Ultra-wideband (UWB). Distance measurements are commonly obtained through the time of arrival (TOA) [48], time difference of arrival (TDOA) [49], and received signal strength (RSS) [50]. Ultra-wideband (UWB) is a key technique that has been proven effective in indoor ranging. UWB has a unique nature: its dual capabilities, communication, and ranging. Radio communication is considered UWB if the signal has a large relative bandwidth that exceeds 20% of the center frequency or a large absolute bandwidth of more than 500MHz [51]. This bandwidth enables high data throughput using short pulses, and more importantly, the wide bandwidth allows accurate ranging. The UWB technology uses short pulses, which are more robust in multipath conditions, and the wide bandwidth allows better ranging performance even in non-line-of-sight conditions [52, 53]. In recent years several companies such as Ubisense [54], Decawave [55], and Sewio [56] have developed real-time localization systems (RTLS) using UWB technology.

2.2.1.1 Range Only Localization

Bertrand Fang has shown that a unique solution for the position can be calculated when there are a minimum of four range measurements to known locations at any given time [13]. When distance measurements to four known locations are available, the position fix can be obtained by solving a quartic equation. Additionally, techniques such as lateration [57], fingerprinting [58], and probabilistic approaches [59] can be used to localize when there are four or more range measurements.

One of the early studies conducted on UWB based localization was carried out by Krishnan et al. in [60]. This study has used TDOA to measure the distance between the robot and the UWB anchors. Interestingly, the authors have developed the UWB anchor module and used wires to synchronize the stationary anchors. However, recent studies have used off-the-shelf UWB modules such as DW1001, to develop localization techniques. Authors in [61] have proposed a multi robot localization system with a self-calibrating UWB network. They have proposed a novel clock synchronization scheme for the UWB anchors and showed improvement in TDOA measurement accuracy. A MAV-based inventory management system is proposed in [62] that uses DW1001 module for ranging and a sub-GHz beacon for synchronization. Authors in [63] use off-the-shelf RTLS and improve the performance of the localization by tracking the dynamic motion of the robot through Bayesian filtering.

2.2.1.2 Range Assisted Localization

Range assisted localization incorporates measurements from sensors such as IMU, velocity, heading, etc., along with the range measurements in the localization algorithm. Several relative localization algorithms have used range measurements along with velocity measurements to localize agents. In [64], Trawny et al. have shown that it is feasible to obtain an algebraic solution for the 3D relative pose of two robots using ten distance measurements between the robots at ten different time steps. In order to obtain the algebraic solution, the robots should have the capability of estimating their location, which can be achieved through dead reckoning (integrating wheel encoders or IMU measurements). Extending the work in [64], Trawny et al. have conducted an observability study on the single range relative localization problem in [65], and propose an EKF based estimator which incorporates velocity measurements of the two robots. Autonomous underwater vehicle (AUV) applications is another area that uses range assisted localization. Most AUV related applications use depth sensors to measure the operating depth of the AUV. Hence localization is mainly carried out on the 2D plane. Authors in [66] have proposed a single range based localization for AUV, and they have used depth measurements along with the yaw measurement. Gadre et al. have proposed a similar single range assisted localization of AUV under the influence of unknown, constant speed currents [26]. In [25] Arrichiello et al. have used a velocity sensor to measure the AUV vehicle and incorporate it with the single range measurement to localize the AUV in 2D. Extending the work in [25], authors in [67] proposed 3D localization with single range measurement to a fixed location. These localization techniques have focused on the kinematics of the robot and used additional velocity and height sensors. Since all the MAVs are equipped with at least one IMU, MAV related applications have opted for range assisted inertial navigation systems for localization.

2.2.2 Range Assisted INS

An inertial navigation system (INS) is a dead reckoning technique that uses an accelerometer and gyroscope to continuously calculate the robot's position, orientation, and velocity. With the development of low cost MEMS-IMUs, INS has been extensively used in the localization of robots. Due to the noise characteristics of low cost

MEMS-IMU, the pose estimate suffers from drift [68]. Hence other sensor measurements are fused with the INS to improve the estimation accuracy.

Early studies on range assisted INS have used GNSS to obtain pseudo range measurements to the satellites and fuse with inertial measurements to obtain accurate localization [69, 70]. Later, for indoor applications, other ranging techniques were used. Study in [71] is one of the early studies that has used UWB technology with INS. Authors in [71] have used the time of arrival (TOA) measurement as the pseudo range measurement in the tightly coupled EKF implementation. In [14], authors have proposed an algorithm fusing IMU, UWB, and vision to estimate the orientation and the 2D position of a MAV. The proposed algorithm is a loosely coupled estimator that uses the position information from the off-the-shelf UWB system, velocity from down facing camera, and inertial measurements and assumes that the height of the MAV is available. A RINS for relative localization of two MAVs using a single range measurement is proposed in [28]. This study assumes that the height and velocity information is available and focuses on addressing the 2.5D pose estimation problem during a leader-follower flight formation. Authors in [72] have proposed a tightly coupled RINS that focuses on the spatial and temporal calibration of the UWB anchors while estimating the pose of the MAV. The study in [73] is one of the first studies that has used the aerodynamic drag force model of MAV in a range assisted INS. However, the authors have used five range anchors to obtain range measurements but have not discussed the effect of fewer range measurements on the estimation performance. To the best of the author's knowledge, this research study is the first that develop a RINS which incorporates the aerodynamic drag forces and uses three or fewer range measurements.

2.2.2.1 Estimation Techniques

Range assisted INS has been implemented using various algorithms, and among them, Kalman filter based algorithms are the most popular. Early studies have used vanilla Kalman filter to implement the RINS by linearizing both system and measurement models [69, 70]. However, the range measurements and the MAV dynamics are inherently nonlinear. Therefore the majority of the RINS implementations have used the extended Kalman filter formulation [14, 71–73]. In recent years, several studies have used unscented Kalman filter (UKF), and cubature Kalman filter (CKF) to capture the higher-order nonlinear dynamics of the range measurements and MAV dynamics [74–77]. Optimization based algorithms such as moving horizon estimator (MHE) have been used in several studies to implement the RINS for MAVs, and the authors claim that optimization based RINS implementation has better performance over Kalman filter based techniques [78, 79]. It should be noted that among the nonlinear filtering and optimization techniques, EKF is one of the techniques with the least computational overhead. Since EKF performs with acceptable accuracy, this thesis focuses on the EKF implementation of the RINS.

2.3 Nonlinear Observability Analysis

Observability of a system quantifies how well the internal states of a system can be determined by the external outputs of the system over a finite period of time [80]. The observability of linear systems is well documented in the literature. Since the research on this thesis is focused on a highly nonlinear system of MAV, special attention is given to the observability of nonlinear systems. The study [81] conducted by Hermann et al. is one of the first studies that discuss the observability of nonlinear systems. Hermann et al. define four classes of observability of nonlinear system. They are 1) observable, 2) locally observable, 3) weakly observable, and 4) locally weakly observable. This thesis focuses on the locally weakly observability of the RINS since it can be determined through an algebraic test. If a system is locally weakly observable, then the states of the system can be inferred instantaneously[3].

Several studies have carried out nonlinear observability analysis on various nonlinear systems. One of the early studies that have utilized the analysis method proposed in [81] is conducted by Trawny et al. in [65]. They studied the observability[4] of relative localization problem when using range and bearing measurements between the robots, and presented the conditions under which the system become unobservable. Authors in [82] have carried out a similar observability study on the 2.5D relative localization problem subjected to velocity constraints.

Observability analysis of a VINS is performed in [83], and this study is one of the first studies that have parameterized the rotation using Rodrigues parameterization (Gibbs vector). Gibbs parameterization is a three-component parameterization instead of the four used in quaternion [84], and it reduces the complexity of the observability analysis. Furthermore, authors in [83] have defined basis functions which further simplifies the observability analysis. Observability of RINS for MAVs is studied in [72], and the authors have identified the sufficient conditions under which the RINS becomes locally weakly observable. In [28], authors have conducted a similar observability study on the single range assisted INS in leader-follower flight formation and identified the unobservable trajectories of the system. The aforementioned studies on the RINS for MAVs have not considered the aerodynamic effects on the MAV, and they have not identified unobservable directions[5] when the MAV is flying in an

---

[3] A more detailed explanation of the nonlinear observability is given in section 3.1.3

[4] The term *observability* refers to the nonlinear observability of a system, unless otherwise mentioned

[5] The terms *unobservable modes* and *unobservable directions* are used interchangeably through out thesis.

unobservable trajectory.

Several studies have analyzed the observability of RINS using different analysis techniques. Authors in [85] have analyzed the global observability of discrete-time range assisted localization for non-holonomic robots and identified the global unobservable conditions. Discretization of the continuous system has facilitated an easy analysis of the observability. Several studies related to range assisted localization of AUVs have proposed state augmentation techniques to convert an inherently nonlinear system to a linear time-varying system and conducted observability analysis by analyzing the observability Gramian [27, 67, 86].

2.4 Consistency Analysis and Improvement

The proposed RINS in this thesis involves the nonlinear process model, i.e., dynamics of MAV, and measurement model, i.e., range measurements. The EKF based estimator can suffer from inconsistencies due to linearization during uncertainty propagation. A consistent estimator has errors that 1) are zero mean and 2) have covariance less than or equal to the values calculated by the filter [20]. The accuracy of the state estimates of an inconsistent estimator is unknown, and therefore the estimator is unreliable.

Inconsistency of the SLAM and VINS have been studied extensively in the literature. Authors in [87] have shown that the EKF implementation of SLAM is inconsistent. They have focused on a stationary robot making several measurements of the same landmark and have shown that the covariance of the yaw angle estimate decreases, even though there is no additional information. Huang et al. have shown that the inconsistency of the EKF-SLAM is caused by a mismatch between the number of unobservable directions of the nonlinear system and the number of unobservable directions of the error state model used for the EKF implementation [21]. A similar study has been carried out in [23] to analyze the consistency of the VINS implementation. No other study has analyzed the consistency of the EKF-RINS with three and two range measurements under unobservable conditions.

In [88], authors have proposed a technique to improve the consistency of the EKF-SLAM implementation. The technique ‘First Estimates Jacobian’ (FEJ) computes Jacobians with the first-ever available estimates for each of the state variables. This results in both the error-state model and the underlying nonlinear model having the same observability properties, which improves the consistency and the accuracy of the estimates. Authors in [23] have proposed observability constrained VINS (OC-VINS) algorithm which enforces both linearized and nonlinear models have the same number of unobservable directions and the same structure. OC-VINS technique is a generalized algorithm that can be adapted for linearized estimator frameworks.

In contrast to the consistency improvement techniques mentioned above, Wu et al. [89] have proposed a novel formulation for VINS, which does not require modifying the Jacobians, or the transition matrix. They have proposed a novel Right Invariant error extended Kalman filter (RIEKF) formulation for the standard VINS and proved that the RIEKF-VINS has invariant properties. RIEKF has been adapted for various localization techniques to improve consistency. In [90] authors have developed an object based SLAM based on RIEKF algorithm.

Chapter 3

Three and Two Range assisted Inertial Navigation System: Design and Observability Analysis

This chapter focuses on developing a three and two range assisted INS for MAVs incorporating the aerodynamic drag forces. An observability study is conducted to determine the feasibility of the RINS with three and two range measurements, and unobservable trajectories along with the corresponding unobservable directions are identified. Numerical simulations are used to validate the identified unobservable trajectories, and the performance of the RINS is experimentally validated.

3.1 Preliminaries

This section introduces rotation parameterizations, general notational definitions, and operators used throughout the thesis.

3.1.1 System Description

In this thesis, it is assumed that the MAV is flying in an environment populated with range sensors, also referred to as range anchors, that are capable of measuring the distance to the MAV. The locations of the range anchors are known with respect to a global reference frame $\{W\}$. The frame $\{W\}$ is defined according to the east, north, up (ENU) coordinates system. The frame $\{B\}$ is attached to the center of gravity of the MAV, and $\{B\}$ is oriented such that the $x-y$ plane of $\{B\}$ is parallel the propeller plane of the MAV and the thrust is parallel to the z axis of $\{B\}$. The frames $\{W\}$, and $\{B\}$ are illustrated in Figure 3.1.

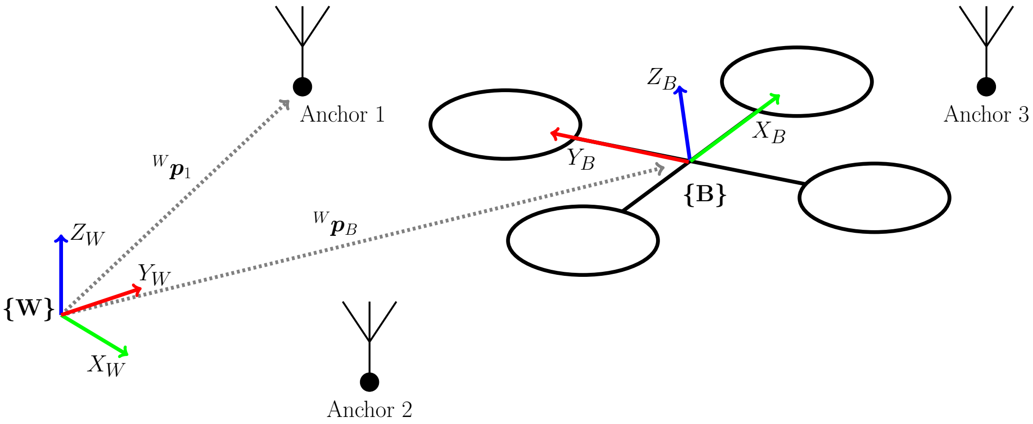

Fig. 3.1: Frames of reference

Without loss of generality, it is assumed that the frames of the sensors onboard the MAV coincide with the frame $\{B\}$. I acknowledge that this assumption is not valid for most of the commercially available MAVs. However, there are various techniques to identify the transformation between $\{B\}$ and the sensor frames, and the identified transformations can be used to map the sensor measurements onto $\{B\}$ [91–93].

In this thesis, vectors are expressed as ${}^W\boldsymbol{a}_B$, where the subscript represents the frame of the vector $\boldsymbol{b}$, and the superscript represents the frame in which the vector $\boldsymbol{b}$ is expressed. For example, ${}^W\boldsymbol{p}_B$ in Fig. 3.1 denotes the position of $\{B\}$ expressed in $\{W\}$

. For the clarity of presentation, the subscript is omitted when both frames are the same. There are a few exceptions to these conventions. First is the accelerometer bias ${}^{B}\boldsymbol{b}_a$, and gyroscope bias ${}^{B}\boldsymbol{b}_g$, where the subscript represents the sensor. The second is the accelerometer measurement ${}^{B}\boldsymbol{a}_m$, and gyroscope measurement${}^{B}\boldsymbol{\omega}_m$. The subscript m denotes a measured value.

3.1.2 3D Rotation Parameterziation

Compared to the representations of 3D position, representations for orientation of a rigid body are numerous. The attitude representations comprise three and four component vectors, as well as 3×3, and 4×4 matrices. Each representation has its own advantages and disadvantages, and it can be advantageous to use one representation over the other in certain applications [84]. In this thesis, the quaternion parameterization is used for the RINS implementation and the Gibbs vector parameterization for the observability analysis.

3.1.2.1 Quaternion parameterization

Quaternion parameterization is a four element parameterization of the 3D orientation. Quaternion representation does not suffer from the singularity problem associated with the Euler angles. There are several ways to determine quaternion, and it has lead to confusion in the science community. Two conventions, namely *Hamilton* and *JPL* are the widely used conventions in literature, however the *Hamilton* convention has gained the wide acceptance in the community [94]. In this thesis *Hamilton* convention is used to represent the quaternion.

A unit quaternion is denoted by $\boldsymbol{q} = [q_w \; q_x \; q_y \; q_z]^T = \left[q_w \; \bar{\boldsymbol{q}}^T\right]^T$, and $\|\boldsymbol{q}\| = 1$. The unit quaternion can be used to represent the rotation of a frame about an axis $\hat{\boldsymbol{n}}$ by an angle of θ as.

$$\boldsymbol{q} = \begin{bmatrix} \cos\left(\frac{\theta}{2}\right) & \hat{\boldsymbol{n}}^T \sin\left(\frac{\theta}{2}\right) \end{bmatrix}^T \tag{3.1}$$

The quaternion multiplication operator ($\otimes$) is defined as follows

$$\boldsymbol{q}_1 \otimes \boldsymbol{q}_2 = \boldsymbol{\Xi}(\boldsymbol{q}_1)\boldsymbol{q}_2 \qquad \text{and} \qquad \boldsymbol{q}_1 \otimes \boldsymbol{q}_2 = \boldsymbol{q}_1 \boldsymbol{\Psi}(\boldsymbol{q}_2), \tag{3.2}$$

where

$$\boldsymbol{\Xi}(\boldsymbol{q}) = q_w \boldsymbol{I}_4 + \begin{bmatrix} 0 & -\bar{\boldsymbol{q}}^T \\ \bar{\boldsymbol{q}} & \lfloor \bar{\boldsymbol{q}} \rfloor_\times \end{bmatrix} \qquad \text{and} \qquad \boldsymbol{\Psi}(\boldsymbol{q}) = q_w \boldsymbol{I}_4 + \begin{bmatrix} 0 & -\bar{\boldsymbol{q}}^T \\ \bar{\boldsymbol{q}} & -\lfloor \bar{\boldsymbol{q}} \rfloor_\times \end{bmatrix}. \tag{3.3}$$

$\boldsymbol{I}_4$ is the 4×4 identity matrix[1].

The operator $\lfloor \cdot \rfloor_\times$ is the skew operator that produces the cross-product matrix,

$$\lfloor \boldsymbol{a} \rfloor_\times \triangleq \begin{bmatrix} 0 & -a_z & a_y \\ a_z & 0 & -a_x \\ -a_y & a_x & 0 \end{bmatrix}. \tag{3.4}$$

The unit quaternion represents the rotation of $\{B\}$ in $\{W\}$ is denoted as ${}^W\boldsymbol{q}_B$, and the operation that express the vector ${}^B\boldsymbol{a}$ in $\{B\}$, in frame $\{W\}$ is defined as

$${}^W\boldsymbol{a}_B = {}^W\boldsymbol{q}_B \otimes \begin{bmatrix} 0 \\ {}^B\boldsymbol{a} \end{bmatrix} \otimes {}^W\boldsymbol{q}_B^{-1}, \tag{3.5}$$

---

[1] In this thesis $\boldsymbol{I}_n$ represents the $n \times n$ identity matrix

where

$$\boldsymbol{q}^{-1} = [q_w \;\; -\bar{\boldsymbol{q}}] \tag{3.6}$$

The rotation matrix from frame $\{B\}$ to $\{W\}$ is denoted as ${}^{W}\boldsymbol{C}_{B}$, and can be expressed using quaternion as

$${}^{W}\boldsymbol{C}_{B} = \boldsymbol{C}({}^{W}\boldsymbol{q}_{B}) = (q_w - \bar{\boldsymbol{q}}^T\bar{\boldsymbol{q}})\boldsymbol{I_3} + 2\bar{\boldsymbol{q}}\bar{\boldsymbol{q}}^T + 2q_w \lfloor \bar{\boldsymbol{q}} \rfloor_{\times} \tag{3.7}$$

Rotation kinematics between two frames can be expressed using quaternion and rotation matrix parameterization as

$${}^{W}\dot{\boldsymbol{q}}_{B} = \frac{1}{2}{}^{W}\boldsymbol{q}_{B} \otimes \begin{bmatrix} 0 \\ {}^{B}\boldsymbol{\omega} \end{bmatrix} \qquad \text{and} \qquad {}^{W}\dot{\boldsymbol{C}}_{B} = {}^{W}\boldsymbol{C}_{B} \lfloor {}^{B}\boldsymbol{\omega} \rfloor_{\times}, \tag{3.8}$$

where ${}^{B}\boldsymbol{\omega}$ is the angular velocity of the MAV expressed in $\{B\}$.

3.1.2.2 Gibbs parameterization

Gibbs parameterization, also known as Gibbs vector, Cayley–Gibbs–Rodriguez (CGR) parameterization is a minimal parameterization of orientation using three elements. Gibbs parameterization suffers from singularity problem, hence not recommended for RINS implementation. However, the minimal representation makes the observability analysis straightforward. The Gibbs vector that represents the rotation of a frame about the axis $\hat{\boldsymbol{n}}$ by an angle θ can be expressed as

$$\boldsymbol{s} = \hat{\boldsymbol{n}} \tan\left(\frac{\theta}{2}\right). \tag{3.9}$$

Composition of two Gibbs vectors, $\boldsymbol{s}_1$, and $\boldsymbol{s}_2$ is defined as

$$\boldsymbol{s}^* = \frac{\boldsymbol{s}_2 + \boldsymbol{s}_1 - \boldsymbol{s}_2 \times \boldsymbol{s}_1}{1 - \boldsymbol{s}_2 \cdot \boldsymbol{s}_1} \tag{3.10}$$

The Gibbs vector for the orientation of $\{B\}$ expressed in $\{W\}$ is denoted as ${}^W\boldsymbol{s}_B$, and the corresponding rotation matrix can be defined using ${}^W\boldsymbol{s}_B$ as

$${}^W\boldsymbol{C}_B = \boldsymbol{C}({}^W\boldsymbol{s}_B) = \frac{1}{1 + \|{}^W\boldsymbol{s}_B\|^2} \left(\left(1 - \|{}^W\boldsymbol{s}_B\|^2\right) \boldsymbol{I_3} + 2 \left\lfloor {}^W\boldsymbol{s}_B \right\rfloor_\times + 2{}^W\boldsymbol{s}_B{}^W\boldsymbol{s}_B^T \right). \tag{3.11}$$

Gibbs vector kinematics are defined as

$${}^W\dot{\boldsymbol{s}}_B = \boldsymbol{D}{}^B\boldsymbol{\omega}, \tag{3.12}$$

where

$$\boldsymbol{D} = \boldsymbol{D}({}^W\boldsymbol{s}_B) \triangleq \frac{\partial {}^W\boldsymbol{s}_B}{\partial \theta} = \frac{1}{2} \left(\boldsymbol{I_3} + \left\lfloor {}^W\boldsymbol{s}_B \right\rfloor_\times + {}^W\boldsymbol{s}_B{}^W\boldsymbol{s}_B^T \right). \tag{3.13}$$

The following identities and the differentiation expressions related to Gibbs vector ${}^W\boldsymbol{s}_B$ and a vector $\boldsymbol{a}$ are used throughout the thesis.

Gibbs vector identities

$${}^W\boldsymbol{s}_B = -{}^B\boldsymbol{s}_W \tag{3.14}$$

$$\boldsymbol{D}({}^B\boldsymbol{s}_W) = \boldsymbol{D}({}^W\boldsymbol{s}_B)^T \tag{3.15}$$

$$\boldsymbol{D}({}^W\boldsymbol{s}_B)\boldsymbol{D}({}^B\boldsymbol{s}_W)^{-1} = \boldsymbol{D}({}^B\boldsymbol{s}_W)^{-1}\boldsymbol{D}({}^W\boldsymbol{s}_B) = {}^W\boldsymbol{C}_B \tag{3.16}$$

$$\boldsymbol{D}({}^B\boldsymbol{s}_W)\boldsymbol{D}({}^W\boldsymbol{s}_B)^{-1} = \boldsymbol{D}({}^W\boldsymbol{s}_B)^{-1}\boldsymbol{D}({}^B\boldsymbol{s}_W) = {}^B\boldsymbol{C}_W \tag{3.17}$$

Differentiation expressions

$$\frac{\partial}{\partial \boldsymbol{s}} {}^W\boldsymbol{C}_B\boldsymbol{a} = -\left\lfloor {}^W\boldsymbol{C}_B\boldsymbol{a} \right\rfloor_\times \boldsymbol{D}({}^B\boldsymbol{s}_W)^{-1} \tag{3.18}$$

$$\frac{\partial}{\partial \boldsymbol{s}} {}^{B}\boldsymbol{C}_{W}\boldsymbol{a} = \lfloor {}^{B}\boldsymbol{C}_{W}\boldsymbol{a} \rfloor_{\times} \boldsymbol{D}({}^{W}\boldsymbol{s}_{B})^{-1} \tag{3.19}$$

$$\frac{\partial}{\partial \boldsymbol{a}} {}^{W}\boldsymbol{C}_{B}\boldsymbol{a} = {}^{W}\boldsymbol{C}_{B} \tag{3.20}$$

$$\frac{\partial}{\partial \boldsymbol{a}} {}^{B}\boldsymbol{C}_{W}\boldsymbol{a} = {}^{B}\boldsymbol{C}_{W} \tag{3.21}$$

3.1.3 Nonlinear Observability Analysis

A general nonlinear system can be expressed as

$$\dot{\mathbf{x}} = \mathbf{f}(\mathbf{x}, \mathbf{u}), \quad \mathbf{y} = \mathbf{h}(\mathbf{x}), \tag{3.22}$$

where the state vector, control input vector and output vector are denoted by $\mathbf{x} \in \mathbb{R}^n$, $\mathbf{u} = [u_1 \ldots u_l]^T \in \mathbb{R}^l$, and $\mathbf{y} = [y_1 \ldots y_m]^T \in \mathbb{R}^m$ respectively. The control affine form of (3.22) can be expressed as

$$\begin{gathered} \dot{\mathbf{x}} = \mathbf{f_0}(\mathbf{x}) + \sum_{\forall k=1}^{l} \mathbf{f_k}(\mathbf{x}) u_k \\ \mathbf{y} = \mathbf{h}(\mathbf{x}), \end{gathered} \tag{3.23}$$

where $\mathbf{f_0}$ is the zero-input process function and $\mathbf{f_k}$ corresponds to the process function that is excited by the k^{th} component of the input control vector $\mathbf{u}$. Observability of a nonlinear system was introduced by Hermann et. al, and they have defined four classes to describe various levels of observability of a nonlinear system [81]. The four classes were defined based on the distinguishability of states, and a pair of states, $\mathbf{x}_0$, and $\mathbf{x}_1$ in the state space $\mathcal{X}$ are said to be *indistinguishable*, if the system (3.23) produce the same input-output map for every admissible input trajectory $\boldsymbol{u}$.

Observable A system is observable if each state $\mathbf{x} \in \mathcal{X}$ is distinguishable from all other states in the state space $\mathcal{X}$. This can be denoted as $I(\mathbf{x}) = \{\mathbf{x}\}$, where I

is the indistinguishability relation on $\mathcal{X}$.

Locally Observable A system is locally observable if each state $\mathbf{x} \in \mathcal{X}$ is distinguishable within every open neighborhood U of $\mathbf{x}$. This is denoted as $I_U(\mathbf{x}) = \{\mathbf{x}\}$.

Weakly Observable A system is weakly observable if each state $\mathbf{x} \in \mathcal{X}$ is only distinguishable in an open subset $U \subseteq \mathcal{X}$. This can be denoted as $I(\mathbf{x}) \cap U = \{\mathbf{x}\}$, and this implies that there can be multiple indistinguishable states in the state space.

Locally Weakly Observable A system is locally weakly observable if each state $\mathbf{x} \in \mathcal{X}$ is distinguishable in every open neighborhood $V \subseteq U$. Where U is an open neighborhood of $\mathbf{x}$. This can be denoted as $I_V(\mathbf{x}) \cap U = \{\mathbf{x}\}$.

The advantage of locally weakly observability over other classes is that it can be determined using a straightforward algebraic test. Interestingly for autonomous linear systems, these four classes of observability are equivalent.

Authors in [81] have defined an observability matrix using the Lie derivatives of the output function $\mathbf{h}(\mathbf{x})$ to determine the locally weakly observability of the nonlinear system. Lie derivatives evaluate how the output function changes due to the changes in the states and input trajectory. The zeroth-order Lie derivative is defined as the output function itself, i.e.

$$\mathfrak{L}^0\mathbf{h} = \mathbf{h}(\mathbf{x}). \tag{3.24}$$

Higher order Lie derivatives can be derived recursively from the definition of $\mathfrak{L}^0\mathbf{h}$. Assume i^{th} order Lie derivative with respect to k^{th} process function is given by $\mathfrak{L}^i_{\mathbf{f_k}}\mathbf{h}$, then $(i+1)^{\text{th}}$ order Lie derivative with respect to i^{th} process function can be calculated as

$$\mathfrak{L}^{i+1}_{\mathbf{f_k}\mathbf{f_l}}\mathbf{h} = \nabla\mathfrak{L}^i_{\mathbf{f_k}}\mathbf{h} \cdot \mathbf{f_l}, \quad k, l, i \in \mathbb{N} \tag{3.25}$$

where

$$\nabla \mathfrak{L}^{i}_{\mathbf{f_k}}\mathbf{h} = \begin{bmatrix} \frac{\partial \mathfrak{L}^{i}_{\mathbf{f_k}}\mathbf{h}}{\partial \mathrm{x}_1} & \frac{\partial \mathfrak{L}^{i}_{\mathbf{f_k}}\mathbf{h}}{\partial \mathrm{x}_2} & \dots & \frac{\partial \mathfrak{L}^{i}_{\mathbf{f_k}}\mathbf{h}}{\partial \mathrm{x}_n} \end{bmatrix}.$$

Using the Lie derivatives, the observability matrix $\boldsymbol{\mathcal{O}}$ is defined as the matrix with rows

$$\boldsymbol{\mathcal{O}} = \{\nabla \mathfrak{L}^{i}_{\mathbf{f_a},\dots,\mathbf{f_b}}\mathbf{h} | a, b = 0 \dots k; i \in \mathbb{N}\}. \tag{3.26}$$

In [81], authors provide the necessary and sufficient conditions under which the nonlinear system given in (3.23) becomes locally weakly observable (**Th. 3.1**). They also define the term *observability rank condition* which is said to be satisfied when the observability matrix (3.26) is full rank.

3.2 Range Assisted Inertial Navigation System

This section presents the design of the range assisted inertial navigation system for the MAV. The structure of the RINS is similar when three and two range measurements are available, and the only difference is in the measurement model of the RINS. In order to distinguish between the three range and two range measurement availability, the terms *Case 1* and *Case 2* are used. The *Case 1* refers to the RINS with three range measurements, and *Case 2* refers to the RINS with two range measurements.

3.2.1 System Mathematical Model

The states of the proposed range assisted INS consists of the position, velocity, and orientation of the MAV along with the time varying IMU biases. The 16 dimensional state vector can be expressed as

$$\mathbf{x} = \begin{bmatrix} {}^{W}\boldsymbol{p}_{B}^{T} & {}^{B}\boldsymbol{v}^{T} & {}^{W}\boldsymbol{q}_{B}^{T} & {}^{B}\boldsymbol{b}_{g}^{T} & {}^{B}\boldsymbol{b}_{a}^{T} \end{bmatrix}^{T}, \tag{3.27}$$

where ${}^{W}\boldsymbol{p}_{B}$ is the position of the MAV expressed in $\{W\}$, ${}^{B}\boldsymbol{v}$ is the velocity of the MAV with respect to $\{W\}$ expressed in $\{B\}$, and ${}^{W}\boldsymbol{q}_{B}$ is the quaternion representation of the orientation of the MAV, $\{B\}$ in $\{W\}$. Biases of the gyroscope and accelerometer measurements are represented by ${}^{B}\boldsymbol{b}_{g}$ and ${}^{B}\boldsymbol{b}_{a}$.

The aerodynamic drag forces acting on the MAV are proportional to the linear velocity of the MAV expressed in $\{B\}$ and to the sum of propeller speeds [15]. Hence the mass normalized drag force $\boldsymbol{f}_{d}$ can be expressed as

$$\boldsymbol{f}_{d} \propto \frac{1}{m}\dot{\theta}_{\Sigma}{}^{B}\boldsymbol{v}, \qquad \dot{\theta}_{\Sigma} = \sum_{i=1}^{4}\left|\dot{\theta}_{i}\right|, \tag{3.28}$$

where $\dot{\theta}_{i}$ is the speed of the i^{th} propeller and m is the mass of the quadrotor MAV.

The attitude control of MAV is achieved by increasing the propeller speed of a propeller while decreasing the speed of the opposing propeller [95]. Hence during slow maneuvers, the sum of propeller speeds, $\dot{\theta}_{\Sigma}$ can be approximated as a constant similar to [36, 37, 96]. Hence, mass and propeller speed normalized drag coefficient matrix $\boldsymbol{K_{d}}$ is defined as

$$\boldsymbol{K_{d}} = \frac{\dot{\theta}_{\Sigma}}{m}\text{diag}(\kappa_{\perp}, \kappa_{\perp}, \kappa_{\parallel}), \tag{3.29}$$

where $\kappa_{\perp}$ and $\kappa_{\parallel}$ are the proportionality constants for the drag forces in the plane of the rotors and in the direction of the thrust vector, respectively. Thus the mass normalized drag force expressed in $\{B\}$ can be expressed as

$$\boldsymbol{f}_{d} = -\boldsymbol{K_{d}}{}^{B}\boldsymbol{v}. \tag{3.30}$$

Identifying the mass normalized drag coefficient matrix $\boldsymbol{K_{d}}$ is crucial for the accuracy of the proposed RINS. The drag coefficients can be identified using the least square optimization approach [73].

The linear acceleration of the MAV expressed in $\{W\}$ can be expressed as

$$^{W}\ddot{\boldsymbol{p}}_{B} = {}^{W}\boldsymbol{C}_{B}\boldsymbol{f}_{d} + {}^{W}\boldsymbol{C}_{B}\boldsymbol{f}_{t} - \boldsymbol{g}, \tag{3.31}$$

where $\boldsymbol{g}$ is the gravitational acceleration vector expressed in $\{W\}$, $\boldsymbol{f}_t$ is the mass normalized thrust vector in $\{B\}$. In general, the propellers of the MAV are placed on the same plane or in parallel planes. Hence the thrust generated by the propellers is perpendicular to the plane of the propellers. Based on the placement of $\{B\}$, the thrust vector $\boldsymbol{f}_t$ can be expressed as

$$\boldsymbol{f}_{t} = f_{t}\grave{\boldsymbol{e}}_{3}, \tag{3.32}$$

where $\grave{\boldsymbol{e}}_3 = [\ 0\ 0\ 1\ ]^T$. The velocity of the MAV expressed in $\{W\}$ can be expressed using the body frame velocity, ${}^{B}\boldsymbol{v}$ as

$$^{W}\dot{\boldsymbol{p}}_{B} = {}^{W}\boldsymbol{v}_{B} = {}^{W}\boldsymbol{C}_{B}{}^{B}\boldsymbol{v}. \tag{3.33}$$

In order to facilitate the observability analysis and the estimator design, the linear acceleration expressed in $\{B\}$ is calculated by taking the time derivative of (3.33) and replacing ${}^{W}\ddot{\boldsymbol{p}}_{B}$ by (3.30).

$$^{B}\dot{\boldsymbol{v}} = \lfloor {}^{B}\boldsymbol{v} \rfloor_{\times}{}^{B}\boldsymbol{\omega} + \boldsymbol{f}_{d} + \boldsymbol{f}_{t} - {}^{W}\boldsymbol{C}_{B}^{T}\boldsymbol{g}. \tag{3.34}$$

3.2.2 Measurement Model

The angular velocity of the MAV is measured by three orthogonal rate gyroscopes, and the measurement can be modelled as

$$^{B}\boldsymbol{\omega}_m = {}^{B}\boldsymbol{\omega} + {}^{B}\boldsymbol{b}_g + \boldsymbol{\eta}_{\omega}, \tag{3.35}$$

where $^{B}\boldsymbol{\omega}_m$ is the measured angular velocity, $\boldsymbol{\eta_\omega}$ is the zero-mean white Gaussian noise with a standard deviation of $\boldsymbol{\sigma_\omega}$. MEMS gyroscope measurements suffer from time varying bias $^{B}\boldsymbol{b}_g$, and can be modelled as random-walk process governed by a zero-mean white Gaussian noise, $\boldsymbol{\eta_{gb}}$ with a standard deviation of $\boldsymbol{\sigma_{gb}}$ [97]. Therefore, the evolution of gyroscope bias can be expressed as

$$^{B}\dot{\boldsymbol{b}}_g = \boldsymbol{\eta_{gb}}. \tag{3.36}$$

Three axis accelerometer measures the linear acceleration of the MAV, and can be modeled as

$$^{B}\boldsymbol{a}_m = {}^{W}\boldsymbol{C}_{B}^{T}({}^{W}\ddot{\boldsymbol{p}}_{B} + \boldsymbol{g}) + {}^{B}\tilde{\boldsymbol{b}}_{\boldsymbol{a}} + \boldsymbol{\eta_a}, \tag{3.37}$$

where $\tilde{\boldsymbol{\eta}}_{\boldsymbol{a}}$ is the zero-mean white Gaussian noise and $\tilde{\boldsymbol{b}}_{\boldsymbol{a}}$ is the bias of the accelerometer measurement. Similar to gyroscope bias, evolution of accelerometer bias can also be modeled as a random-walk process governed by zero-mean white Gaussian noise $\tilde{\boldsymbol{\eta}}_{\boldsymbol{ab}}$ with standard deviation of $\tilde{\boldsymbol{\sigma}}_{\boldsymbol{ab}}$ [97].

$$^{B}\dot{\tilde{\boldsymbol{b}}}_{\boldsymbol{a}} = \tilde{\boldsymbol{\eta}}_{\boldsymbol{ab}} \tag{3.38}$$

In developing the three and two range assisted INS, the thrust, $\boldsymbol{f}_t$ is considered an estimated variable. Most MAVs are not equipped with sensors to measure the thrust or the propeller speeds, and in some commercially available MAVs, thrust information is unavailable to the developers. In this study, the thrust is modeled as a random walk process, and the mass normalized thrust is several magnitudes higher than the accelerometer bias in the z direction. Therefore, the accelerometer bias in the z direction and the mass normalized thrust are combined[2] and the new combined bias is defined as ${}^{B}\boldsymbol{b}_a$, where

$$ {}^{B}\boldsymbol{b}_a = [\ b_{ax}\ b_{ay}\ b_{az}\ ]^T = {}^{B}\tilde{\boldsymbol{b}}_{\boldsymbol{a}} + f_t \grave{\boldsymbol{e}}_3. \tag{3.39} $$

The noise characteristics of the combined bias $\boldsymbol{\eta_{ab}}$ can be modeled as

$$ \boldsymbol{\eta_{ab}} = \tilde{\boldsymbol{\eta}}_{\boldsymbol{ab}} + \eta_{f_t} \grave{\boldsymbol{e}}_3, \tag{3.40} $$

where η_{f_t} is the standard deviation of the thrust. Hence the dynamics of the combined accelerometer bias can be expressed as

$$ {}^{B}\dot{\boldsymbol{b}}_a = \boldsymbol{\eta_{ab}}. \tag{3.41} $$

Combining (3.30), (3.32), (3.37), and (3.39) accelerometer measurement can be rewritten as

$$ {}^{B}\boldsymbol{a}_m = -\boldsymbol{K_d}\,{}^{B}\boldsymbol{v} + {}^{B}\boldsymbol{b}_a + \boldsymbol{\eta_a}. \tag{3.42} $$

The range measurements are between the MAV and the i^{th} range anchor can be expressed as

$$ r_i = \|{}^{W}\boldsymbol{r}_i\| + \eta_{ri}, \quad {}^{W}\boldsymbol{r}_i \triangleq {}^{W}\boldsymbol{p}_B - {}^{W}\boldsymbol{p}_i, \tag{3.43} $$

where ${}^{W}\boldsymbol{p}_i$ is the location of the i^{th} range anchor expressed in $\{W\}$, and η_{ri} is the

---

[2] Based on the assumption stated in section 3.1.1, the direction of thrust and z direction of the accelerometer are parallel.

zero-mean white Gaussian noise of the i^{th} range measurement.

The nonlinear state space model of the proposed RINS can be summarized as follows

$$\dot{\mathbf{x}} = \mathbf{f}(\mathbf{x}, \boldsymbol{u}, \boldsymbol{\eta})$$

$$\begin{bmatrix} {}^{W}\dot{\boldsymbol{p}}_{B} \\ {}^{B}\dot{\boldsymbol{v}} \\ {}^{W}\dot{\boldsymbol{q}}_{B} \\ {}^{B}\dot{\boldsymbol{b}}_{g} \\ {}^{B}\dot{\boldsymbol{b}}_{a} \end{bmatrix} = \begin{bmatrix} {}^{W}\boldsymbol{C}_{B}{}^{B}\boldsymbol{v} \\ \lfloor {}^{B}\boldsymbol{v} \rfloor_{\times} \left({}^{B}\boldsymbol{\omega}_{m} - {}^{B}\boldsymbol{b}_{g} - \boldsymbol{\eta}_{\boldsymbol{\omega}}\right) - \boldsymbol{K}_{\boldsymbol{d}}{}^{B}\boldsymbol{v} + b_{az}\grave{\boldsymbol{e}}_{\boldsymbol{3}} - {}^{W}\boldsymbol{C}_{B}^{T}\boldsymbol{g} \\ \frac{1}{2}\boldsymbol{\Xi}(\boldsymbol{q}) \left[0 \; \left({}^{B}\boldsymbol{\omega}_{m} - {}^{B}\boldsymbol{b}_{g} - \boldsymbol{\eta}_{\boldsymbol{\omega}}\right)^{T}\right]^{T} \\ \boldsymbol{\eta}_{\boldsymbol{gb}} \\ \boldsymbol{\eta}_{\boldsymbol{ab}} \end{bmatrix} \tag{3.44}$$

The measurement model of the RINS includes the accelerometer and range measurements. The number of available range measurements determines the number of range measurements included in the measurement model. Hence the generic measurement model can be expressed as

$$\mathbf{y} = \mathbf{h}(\mathbf{x}, \boldsymbol{\nu})$$

$$\mathbf{y} = \begin{bmatrix} \mathbf{h}_{a}(\mathbf{x}) \\ \mathbf{h}_{r}(\mathbf{x}) \end{bmatrix} = \left[\begin{array}{c} -\boldsymbol{K}_{\boldsymbol{d}}{}^{B}\boldsymbol{v} + {}^{B}\boldsymbol{b}_{a} + \boldsymbol{\eta}_{\boldsymbol{a}} \\ \hdashline r_{1} + \eta_{r1} \\ \vdots \\ r_{j} + \eta_{rj} \end{array}\right], \; j \in \mathbb{Z}^{+}, j > 1, \tag{3.45}$$

where for *Case 1*, $j = 3$ and for *Case 2*, $j = 2$. [3]

---

[3] Through out the thesis, the variables, $i, j, n, m \in \mathbb{Z}^{+}$ and $\alpha_{*}, \beta_{*} \in \mathbb{R}$. Otherwise stated.

3.3 Observability Analysis of RINS

3.3.1 Revisiting System Model

The nonlinear observability analysis is carried out by calculating an observability matrix using the Lie derivatives of the output function and their gradients. The three element Gibbs vector parameterization is used to parameterize the orientation of the MAV instead of the four element quaternion parameterization used in the design of the RINS. Modeling the system using Gibbs vector simplifies the observability analysis and allows the identification of the unobservable modes of the system. The maximum rotation facilitated during the observability analysis is less than 180 degrees about any axis. Therefore, the observability analysis does not suffer from the singularity issue of Gibbs parameterization. The new 15 dimensional state vector can be redefined as

$$\mathbf{x} = \begin{bmatrix} {}^{W}\boldsymbol{p}_{B}^{T} & {}^{B}\boldsymbol{v}^{T} & {}^{W}\boldsymbol{s}_{B}^{T} & {}^{B}\boldsymbol{b}_{g}^{T} & {}^{B}\boldsymbol{b}_{a}^{T} \end{bmatrix}^{T}. \tag{3.46}$$

Substituting the angular velocity measurements provided by the gyroscope in (3.35) into the Gibbs kinematics in (3.12), the rotation kinematics can be expressed as

$${}^{W}\dot{\boldsymbol{s}}_{B} = \boldsymbol{D}\left({}^{B}\boldsymbol{\omega}_{m} - {}^{B}\boldsymbol{b}_{g} - \boldsymbol{\eta}_{\omega}\right). \tag{3.47}$$

The control affine form of the RINS presented in (3.44) without the noise components can be rewritten with Gibbs parameterization as

$$\begin{bmatrix} {}^{W}\dot{\boldsymbol{p}}_{B} \\ {}^{B}\dot{\boldsymbol{v}} \\ {}^{W}\dot{\boldsymbol{s}}_{B} \\ {}^{B}\dot{\boldsymbol{b}}_{g} \\ {}^{B}\dot{\boldsymbol{b}}_{a} \end{bmatrix} = \underbrace{\begin{bmatrix} {}^{W}\boldsymbol{C}_{B}\,{}^{B}\boldsymbol{v} \\ -\lfloor {}^{B}\boldsymbol{v} \rfloor_{\times}\,{}^{B}\boldsymbol{b}_{g} - \boldsymbol{K_d}\,{}^{B}\boldsymbol{v} + b_{az}\dot{\boldsymbol{e}}_{\mathbf{3}} - {}^{W}\boldsymbol{C}_{B}^{T}\boldsymbol{g} \\ -\boldsymbol{D}\,{}^{B}\boldsymbol{b}_{g} \\ \mathbf{0}_{3\times1} \\ \mathbf{0}_{3\times1} \end{bmatrix}}_{\mathbf{f_0}} + \underbrace{\begin{bmatrix} \mathbf{0}_{3\times3} \\ \lfloor {}^{B}\boldsymbol{v} \rfloor_{\times} \\ \boldsymbol{D} \\ \mathbf{0}_{3\times3} \\ \mathbf{0}_{3\times3} \end{bmatrix}}_{\mathbf{f_1}} {}^{B}\boldsymbol{\omega}_{m}, \tag{3.48}$$

$\mathbf{f_1}$ is the concatenated matrix of three process functions that corresponds to the three components of the angular velocity, and they are defined such that

$$\mathbf{f_1}\boldsymbol{\omega} = \mathbf{f_{11}} \cdot \omega_x + \mathbf{f_{12}} \cdot \omega_y + \mathbf{f_{13}} \cdot \omega_z, \tag{3.49}$$

and

$$\mathbf{f_1} = \left[\mathbf{f_{11}}\ \mathbf{f_{12}}\ \mathbf{f_{13}}\right]. \tag{3.50}$$

In order to further simplify the observability analysis, $r_i^2/2$ is used instead of r_i in the measurement model. Since r_i and r_i^2 are strictly positive and have a one-to-one correspondence, both provide the same information and do not affect the system's observability [65]. Hence the modified measurement model can be expressed as

$$\mathbf{y} = \mathbf{h}(\mathbf{x}) = \begin{bmatrix} -\boldsymbol{K_d}\,{}^{B}\boldsymbol{v} + {}^{B}\boldsymbol{b}_{a} \\ \frac{1}{2}r_1^2 \\ \vdots \\ \frac{1}{2}r_j^2 \end{bmatrix} = \begin{bmatrix} -\boldsymbol{K_d}\,{}^{B}\boldsymbol{v} + {}^{B}\boldsymbol{b}_{a} \\ \frac{1}{2}\left({}^{W}\boldsymbol{p}_{B} - {}^{W}\boldsymbol{p}_{1}\right)^{T}\left({}^{W}\boldsymbol{p}_{B} - {}^{W}\boldsymbol{p}_{1}\right) \\ \vdots \\ \frac{1}{2}\left({}^{W}\boldsymbol{p}_{B} - {}^{W}\boldsymbol{p}_{j}\right)^{T}\left({}^{W}\boldsymbol{p}_{B} - {}^{W}\boldsymbol{p}_{j}\right) \end{bmatrix},\ j \in \mathbb{Z}^{+}, j > 1. \tag{3.51}$$

3.3.2 *Case 1*: Three range assisted INS

Three range measurements are available for the RINS under *Case 1*, and therefore $j = 3$ in (3.51). The zeroth order Lie derivative of the measurement function $\mathbf{h}(\mathbf{x})$ can be expressed as

$$\mathfrak{L}^0\mathbf{h} = \mathbf{h}(\mathbf{x}) \tag{3.52}$$

The gradient of $\mathfrak{L}^0\mathbf{h}$ with respect to the state vector can be calculated as

$$\nabla\mathfrak{L}^0\mathbf{h} = \begin{bmatrix} \mathbf{0}_{3\times3} & -\boldsymbol{K_d} & \mathbf{0}_{3\times3} & \mathbf{0}_{3\times3} & \boldsymbol{I_3} \\ \boldsymbol{\Gamma_3} & \mathbf{0}_{3\times3} & \mathbf{0}_{3\times3} & \mathbf{0}_{3\times3} & \mathbf{0}_{3\times3} \end{bmatrix}, \tag{3.53}$$

where $\boldsymbol{\Gamma_3} \triangleq [\ {}^W\boldsymbol{r}_1\ {}^W\boldsymbol{r}_2\ {}^W\boldsymbol{r}_3\ ]^T$. The first order Lie derivative with respect to $\mathbf{f_0}$ can be calculated as

$$\mathfrak{L}^1_{\mathbf{f_0}}\mathbf{h} = \nabla\mathfrak{L}^0\mathbf{h}\cdot\mathbf{f_0} = \begin{bmatrix} -\boldsymbol{K_d}\,{}^B\dot{\boldsymbol{v}}' \\ \boldsymbol{\Gamma_3}\,{}^W\boldsymbol{C}_B\,{}^B\boldsymbol{v} \end{bmatrix}, \tag{3.54}$$

where

$${}^B\dot{\boldsymbol{v}}' = -\left\lfloor {}^B\boldsymbol{v} \right\rfloor_\times {}^B\boldsymbol{b}_g - \boldsymbol{K_d}\,{}^B\boldsymbol{v} + b_{az}\grave{\boldsymbol{e}}_\mathbf{3} - {}^W\boldsymbol{C}_B^T\boldsymbol{g}. \tag{3.55}$$

The span of the $\mathfrak{L}^1_{\mathbf{f_0}}\mathbf{h}$ can be calculated as

$$\nabla\mathfrak{L}^1_{\mathbf{f_0}}\mathbf{h} = \begin{bmatrix} \mathbf{0}_{3\times3} & \boldsymbol{K_d}\left(\boldsymbol{K_d} - \left\lfloor {}^B\boldsymbol{b}_g \right\rfloor_\times\right) & \boldsymbol{K_d}\left\lfloor {}^W\boldsymbol{C}_B^T\boldsymbol{g} \right\rfloor_\times \boldsymbol{D}^{-1} & \boldsymbol{K_d}\left\lfloor {}^B\boldsymbol{v} \right\rfloor_\times & -\boldsymbol{K_d}\boldsymbol{I}_{33} \\ \boldsymbol{V_3}\,{}^W\boldsymbol{C}_B^T & \boldsymbol{\Gamma_3}\,{}^W\boldsymbol{C}_B & -\boldsymbol{\Gamma_3}\left\lfloor {}^W\boldsymbol{C}_B\,{}^B\boldsymbol{v} \right\rfloor_\times \left(\boldsymbol{D}^T\right)^{-1} & \mathbf{0}_{3\times3} & \mathbf{0}_{3\times3} \end{bmatrix}, \tag{3.56}$$

where $\boldsymbol{V_3} = [\ {}^B\boldsymbol{v},\ {}^B\boldsymbol{v},\ {}^B\boldsymbol{v}\ ]^T$, and $\boldsymbol{I}_{33} \triangleq [\mathbf{0_{3\times2}},\ \grave{\boldsymbol{e}}_3]$.

The second order Lie derivative of $\mathfrak{L}^1_{\mathbf{f_0}}\mathbf{h}$ with respect to $\mathbf{f_0}$ and it's gradient can be expressed as

$$\mathfrak{L}^2_{\mathbf{f_0}\mathbf{f_0}}\mathbf{h} = \nabla\mathfrak{L}^1_{\mathbf{f_0}}\mathbf{h}\cdot\mathbf{f_0} = \begin{bmatrix} \boldsymbol{K_d}\left(\boldsymbol{K_d} - \lfloor{}^{B}\boldsymbol{b}_g\rfloor_\times\right){}^{B}\dot{\boldsymbol{v}} - \boldsymbol{K_d}\left\lfloor{}^{W}\boldsymbol{C}_{B}^{T}\boldsymbol{g}\right\rfloor_\times{}^{B}\boldsymbol{b}_g \\ \boldsymbol{V_3}{}^{B}\boldsymbol{v} + \boldsymbol{\Gamma_3}{}^{W}\boldsymbol{C}_{B}{}^{B}\dot{\boldsymbol{v}}' + \boldsymbol{\Gamma_3}{}^{W}\boldsymbol{C}_{B}\lfloor{}^{B}\boldsymbol{v}\rfloor_\times{}^{B}\boldsymbol{b}_g \end{bmatrix} \tag{3.57}$$

$$\nabla\mathfrak{L}^2_{\mathbf{f_0}\mathbf{f_0}}\mathbf{h} = \begin{bmatrix} \mathbf{0}_{3\times3} & -\boldsymbol{K_d}\left(\boldsymbol{K_d} - \lfloor{}^{B}\boldsymbol{b}_g\rfloor_\times\right)^2 & \boldsymbol{\Theta} & \boldsymbol{\Phi} & \boldsymbol{K_d}\left(\boldsymbol{K_d} - \lfloor{}^{B}\boldsymbol{b}_g\rfloor_\times\right)\boldsymbol{I}_{33} \\ \boldsymbol{\Upsilon_3} & 2\boldsymbol{V_3} - \boldsymbol{\Gamma_3}{}^{W}\boldsymbol{C}_{B}\boldsymbol{K_d} & \boldsymbol{\Lambda_3} & \mathbf{0}_{3\times3} & \boldsymbol{\Gamma_3}{}^{W}\boldsymbol{C}_{B}\boldsymbol{I}_{33} \end{bmatrix}, \tag{3.58}$$

where

$$\begin{aligned} \boldsymbol{\Theta} &= -\boldsymbol{K_d}\left(\boldsymbol{K_d} - 2\lfloor{}^{B}\boldsymbol{b}_g\rfloor_\times\right)\left\lfloor{}^{W}\boldsymbol{C}_{B}^{T}\boldsymbol{g}\right\rfloor_\times\boldsymbol{D}^{-1} \\ \boldsymbol{\Phi} &= \boldsymbol{K_d}\left\lfloor\left(-\boldsymbol{K_d}{}^{B}\boldsymbol{v} + b_{az}\grave{\mathbf{e}}_{\mathbf{3}} - 2{}^{W}\boldsymbol{C}_{B}^{T}\boldsymbol{g}\right)\right\rfloor_\times - \boldsymbol{K_d}\left(\boldsymbol{K_d} - \lfloor{}^{B}\boldsymbol{b}_g\rfloor_\times\right)\lfloor{}^{B}\boldsymbol{v}\rfloor_\times\ \ldots \\ &\qquad\qquad \ldots\ + \boldsymbol{K_d}\left\lfloor\lfloor{}^{B}\boldsymbol{b}_g\rfloor_\times{}^{B}\boldsymbol{v}\right\rfloor_\times \\ \boldsymbol{\Lambda_3} &= -\boldsymbol{\Gamma_3}\left(\lfloor{}^{W}\boldsymbol{C}_{B}(-\boldsymbol{K_d}{}^{B}\boldsymbol{v} + b_{az}\grave{\mathbf{e}}_{\mathbf{3}})\rfloor_\times\right)\left(\boldsymbol{D}^{T}\right)^{-1} \\ \boldsymbol{\Upsilon_3} &= [\ {}^{W}\ddot{\boldsymbol{p}}_{B}\ {}^{W}\ddot{\boldsymbol{p}}_{B}\ {}^{W}\ddot{\boldsymbol{p}}_{B}\ ]^{T};\ {}^{W}\ddot{\boldsymbol{p}}_{B} = {}^{W}\boldsymbol{C}_{B}\left(-\boldsymbol{K_d}{}^{B}\boldsymbol{v} + b_{az}\grave{\mathbf{e}}_{\mathbf{3}} - {}^{W}\boldsymbol{C}_{B}^{T}\boldsymbol{g}\right). \end{aligned}$$

Using (3.53), (3.56) and (3.58), the nonlinear observability matrix can be constructed as

$$\boldsymbol{\mathcal{O}}_{\boldsymbol{3R}} = \begin{bmatrix} \nabla\mathfrak{L}^0\mathbf{h} \\ \nabla\mathfrak{L}^1_{\mathbf{f_0}}\mathbf{h} \\ \nabla\mathfrak{L}^2_{\mathbf{f_0}\mathbf{f_0}}\mathbf{h} \end{bmatrix}. \tag{3.59}$$

$$\boldsymbol{\mathcal{O}}_{\boldsymbol{3R}} =$$

$$\begin{bmatrix} \mathbf{0}_{3\times3} & -\boldsymbol{K_d} & \mathbf{0}_{3\times3} & \mathbf{0}_{3\times3} & \boldsymbol{I_3} \\ \boldsymbol{\Gamma_3} & \mathbf{0}_{3\times3} & \mathbf{0}_{3\times3} & \mathbf{0}_{3\times3} & \mathbf{0}_{3\times3} \\ \mathbf{0}_{3\times3} & \boldsymbol{K_d}\left(\boldsymbol{K_d} - \lfloor {}^{B}\boldsymbol{b}_g \rfloor_\times\right) & \boldsymbol{K_d}\left\lfloor {}^{W}\boldsymbol{C}_{B}^{T}\boldsymbol{g} \right\rfloor_\times \boldsymbol{D}^{-1} & \boldsymbol{K_d}\lfloor {}^{B}\boldsymbol{v} \rfloor_\times & \boldsymbol{K_d}\boldsymbol{I}_{33} \\ \boldsymbol{V_3}{}^{W}\boldsymbol{C}_{B}^{T} & \boldsymbol{\Gamma_3}{}^{W}\boldsymbol{C}_{B} & -\boldsymbol{\Gamma_3}\lfloor {}^{W}\boldsymbol{C}_{B}{}^{B}\boldsymbol{v} \rfloor_\times \left(\boldsymbol{D}^{T}\right)^{-1} & \mathbf{0}_{3\times3} & \mathbf{0}_{3\times3} \\ \mathbf{0}_{3\times3} & -\boldsymbol{K_d}\left(\lfloor {}^{B}\boldsymbol{b}_g \rfloor_\times - \boldsymbol{K_d}\right)^2 & \boldsymbol{\Theta} & \boldsymbol{\Phi} & \boldsymbol{K_d}\left(\boldsymbol{K_d} - \lfloor {}^{B}\boldsymbol{b}_g \rfloor_\times\right)\boldsymbol{I}_{33} \\ \boldsymbol{\Upsilon_3} & 2\boldsymbol{V_3} - \boldsymbol{\Gamma_3}{}^{W}\boldsymbol{C}_{B}\boldsymbol{K_d} & \boldsymbol{\Lambda_3} & \mathbf{0}_{3\times3} & \boldsymbol{\Gamma_3}{}^{W}\boldsymbol{C}_{B}\boldsymbol{I}_{33} \end{bmatrix}. \tag{3.60}$$

Lemma 3.1. *The RINS with three range measurements is locally weakly observable when 1) Three range anchors are non-collinear. 2) MAV is not on the plane of the three anchors. 3) MAV is not stationary, and* ${}^{B}\boldsymbol{v} \nparallel {}^{W}\boldsymbol{C}_{B}^{T}\boldsymbol{g}$

Proof. The rank of the observability matrix in (3.60) is determined by calculating the rank of each block column of the matrix $\boldsymbol{\mathcal{O}}_{\boldsymbol{3R}}$. When the MAV is not on the plane of the three anchors, $\boldsymbol{\Gamma_3}$ on the first block column has full rank of three, irrespective of the velocity and the acceleration of the MAV. $\boldsymbol{K_d}$ is a diagonal matrix, and therefore the second block column is also full rank. The non-zeros blocks of the third block column can be expressed as

$$\boldsymbol{\mathcal{O}}'_{\boldsymbol{3R},(:,3)} = \begin{bmatrix} \boldsymbol{K_d}\left\lfloor {}^{W}\boldsymbol{C}_{B}^{T}\boldsymbol{g} \right\rfloor_\times \boldsymbol{D}^{-1} \\ \boldsymbol{\Gamma_3}\lfloor {}^{W}\boldsymbol{C}_{B}{}^{B}\boldsymbol{v} \rfloor_\times (\boldsymbol{D}^{T})^{-1} \\ -\boldsymbol{K_d}\left(\boldsymbol{K_d} - 2\lfloor {}^{B}\boldsymbol{b}_g \rfloor_\times\right)\left\lfloor {}^{W}\boldsymbol{C}_{B}^{T}\boldsymbol{g} \right\rfloor_\times \boldsymbol{D}^{-1} \\ \boldsymbol{\Gamma_3}\left(\lfloor {}^{W}\boldsymbol{C}_{B}({}^{B}\boldsymbol{v} - b_{az}\grave{\boldsymbol{e}}_{\boldsymbol{3}}) \rfloor_\times\right)\left(\boldsymbol{D}^{T}\right)^{-1} \end{bmatrix}$$

If the MAV is non-stationary, and ${}^{B}\boldsymbol{v} \nparallel {}^{W}\boldsymbol{C}_{B}^{T}\boldsymbol{g}$, the block matrix $\boldsymbol{\mathcal{O}}'_{\boldsymbol{3R},(:,3)}$[4] has a rank

---

[4] The subscript notation $\boldsymbol{\mathcal{O}}_{(i,:)}$ and $\boldsymbol{\mathcal{O}}_{(:,j)}$ refer to the i^{th} block row and j^{th} block column of

of three. By analyzing the non-zero blocks of the fourth column, it is straightforward to show that the column has full rank except when the MAV is stationary. Since the first block row of the fifth column is the identity matrix, the fifth column has full rank. Therefore, the observability matrix $\boldsymbol{\mathcal{O}}_{\boldsymbol{3R}}$ has a rank of 15, and based on Lemma 3.1 of [81], the RINS with three range measurements is locally weakly observable. □

3.3.3 Unobservable Scenarios of *Case 1*

This section focuses on three scenarios (trajectories) that cause the three rang assisted INS to become unobservable. The observability matrix $\boldsymbol{\mathcal{O}}_{\boldsymbol{3R}}$ is analyzed to identify the unobservable directions corresponding to each scenario. The unobservable directions span the unobservable sub-space of an unobservable system. Therefore, if information acquired by the estimator lies along an unobservable direction, then the accuracy of the estimation decreases.

3.3.3.1 Scenario 1: MAV is stationary with three range anchors

Lemma 3.2. *When the MAV is stationary, the RINS with three range measurements become unobservable, and the unobservable sub-space is spanned by*

$$^{1}\boldsymbol{\mathcal{N}} = \begin{bmatrix} \mathbf{0}_{3\times1} & \mathbf{0}_{3\times1} \\ \mathbf{0}_{3\times1} & \mathbf{0}_{3\times1} \\ \boldsymbol{D}^{W}\boldsymbol{C}_{B}^{T}\boldsymbol{g} & \mathbf{0}_{3\times1} \\ \mathbf{0}_{3\times1} & b_{az}\grave{\boldsymbol{e}}_{\mathbf{3}} \\ \mathbf{0}_{3\times1} & \mathbf{0}_{3\times1} \end{bmatrix}. \tag{3.61}$$

---

matrix $\boldsymbol{\mathcal{O}}$, respectively, while $\boldsymbol{\mathcal{O}}_{(i,j)}$ refers to the block element (i, j).

Proof. The stationary MAV has zero velocity, ${}^{B}\boldsymbol{v} = \mathbf{0}_{3\times1}$ and zero acceleration ${}^{W}\ddot{\boldsymbol{p}}_{B} = \mathbf{0}_{3\times1}$. Hence the equation (3.31) can be simplified as ${}^{W}\boldsymbol{C}_{B} b_{az} \grave{\boldsymbol{e}}_{\boldsymbol{3}} = \boldsymbol{g}$, Substituting these values into (3.53), (3.56) and (3.58), the new observability matrix $\boldsymbol{\mathcal{O}}_{\boldsymbol{3R_{S1}}}$ can be expressed as

$$
\boldsymbol{\mathcal{O}}_{\boldsymbol{3R_{S1}}} = \\
\begin{bmatrix}
\mathbf{0}_{3\times3} & -\boldsymbol{K_d} & \mathbf{0}_{3\times3} & \mathbf{0}_{3\times3} & \boldsymbol{I_3} \\
\boldsymbol{\Gamma_3} & \mathbf{0}_{3\times3} & \mathbf{0}_{3\times3} & \mathbf{0}_{3\times3} & \mathbf{0}_{3\times3} \\
\mathbf{0}_{3\times3} & \boldsymbol{K_d}\left(\boldsymbol{K_d} - \lfloor {}^{B}\boldsymbol{b}_g \rfloor_\times\right) & \boldsymbol{K_d}\left\lfloor {}^{W}\boldsymbol{C}_{B}^{T}\boldsymbol{g} \right\rfloor_\times \boldsymbol{D}^{-1} & \mathbf{0}_{3\times3} & \boldsymbol{K_d}\boldsymbol{I}_{33} \\
\mathbf{0}_{3\times3} & \boldsymbol{\Gamma_3}{}^{W}\boldsymbol{C}_{B} & \mathbf{0}_{3\times3} & \mathbf{0}_{3\times3} & \mathbf{0}_{3\times3} \\
\mathbf{0}_{3\times3} & -\boldsymbol{K_d}\left(\lfloor {}^{B}\boldsymbol{b}_g \rfloor_\times - \boldsymbol{K_d}\right)^2 & \boldsymbol{\Theta} & -\boldsymbol{K_d}\lfloor (b_{az}\grave{\boldsymbol{e}}_{\boldsymbol{3}}) \rfloor_\times & \boldsymbol{K_d}\left(\boldsymbol{K_d} - \lfloor {}^{B}\boldsymbol{b}_g \rfloor_\times\right)\boldsymbol{I}_{33} \\
\mathbf{0}_{3\times3} & -\boldsymbol{\Gamma_3}{}^{W}\boldsymbol{C}_{B}\boldsymbol{K_d} & \boldsymbol{\Lambda}_{\boldsymbol{3_{S1}}} & \mathbf{0}_{3\times3} & \boldsymbol{\Gamma_3}{}^{W}\boldsymbol{C}_{B}\boldsymbol{I}_{33}
\end{bmatrix}, \tag{3.62}
$$

where,

$$
\boldsymbol{\Lambda}_{\boldsymbol{3_{S1}}} = -\boldsymbol{\Gamma_3}\left(\lfloor \boldsymbol{g} \rfloor_\times\right)\left(\boldsymbol{D}^{T}\right)^{-1}.
$$

It is straightforward to show that the rank of both the third and fourth block columns of $\boldsymbol{\mathcal{O}}_{\boldsymbol{3R_{S1}}}$ have rank of two. Hence the three range assisted INS is unobservable under **Scenario 1**, and the system has two unobservable directions.

Multiplying $\boldsymbol{\mathcal{O}}_{\boldsymbol{3R_{S1}}}$ by the first column of the null vector ${}^{1}\boldsymbol{\mathcal{N}}$ results in

$$
\begin{aligned}
\boldsymbol{\mathcal{O}}_{\boldsymbol{3R_{S1}}}{}^{1}\boldsymbol{\mathcal{N}}_{(:,1)} &= -\boldsymbol{\Gamma_3}\left(\lfloor \boldsymbol{g} \rfloor_\times\right)\left(\boldsymbol{D}^{T}\right)^{-1}\boldsymbol{D}{}^{W}\boldsymbol{C}_{B}^{T}\boldsymbol{g} \\
&= -\boldsymbol{\Gamma_3}\left(\lfloor \boldsymbol{g} \rfloor_\times\right){}^{W}\boldsymbol{C}_{B}{}^{W}\boldsymbol{C}_{B}^{T}\boldsymbol{g} \\
&= \mathbf{0}_{3\times1}.
\end{aligned} \tag{3.63}
$$

It is straight forward to show that $\boldsymbol{\mathcal{O}}_{\boldsymbol{3R_{S1}}}{}^{1}\boldsymbol{\mathcal{N}}_{(:,2)} = \mathbf{0}_{3\times1}$. Hence, the ${}^{1}\boldsymbol{\mathcal{N}}$ spans the unobservable sub-space. □

The null vector given in (3.61) shows that the two unobservable directions correspond to the orientation and gyroscope bias states. ${}^{1}\boldsymbol{\mathcal{N}}_{(:,1)}$ corresponds to rotation about the gravity vector[5], and ${}^{1}\boldsymbol{\mathcal{N}}_{(:,2)}$ corresponds to the gyroscope bias along the z axis of $\{B\}$.

3.3.3.2 Scenario 2: MAV is flying on the plane of the three range anchors

Lemma 3.3. *When the MAV is flying on the plane of the three range anchors, the RINS with three range measurements becomes unobservable, and the unobservable subspace is spanned by*

$$ {}^{2}\boldsymbol{\mathcal{N}} = \begin{bmatrix} (\boldsymbol{l}_{12} \times \boldsymbol{l}_{13})^T & \mathbf{0}_{1\times3} & \mathbf{0}_{1\times3} & \mathbf{0}_{1\times3} & \mathbf{0}_{1\times3} \end{bmatrix}^T . \tag{3.64}$$

where $\boldsymbol{l}_{12} = {}^{W}\boldsymbol{r}_2 - {}^{W}\boldsymbol{r}_1$ *and* $\boldsymbol{l}_{13} = {}^{W}\boldsymbol{r}_3 - {}^{W}\boldsymbol{r}_1$*.*

Proof. When the MAV is flying on the plane of the anchors, i.e. $({}^{W}\boldsymbol{r}_1 \times {}^{W}\boldsymbol{r}_2) \cdot {}^{W}\boldsymbol{r}_3 = 0$ and ${}^{W}\boldsymbol{r}_3 = \alpha {}^{W}\boldsymbol{r}_1 + \beta {}^{W}\boldsymbol{r}_2$, the velocity and the acceleration of the MAV can be expressed as

$$ {}^{W}\boldsymbol{v}_{B} = {}^{W}\boldsymbol{C}_{B}{}^{B}\boldsymbol{v} = \alpha_1 \boldsymbol{l}_{12} + \beta_1 \boldsymbol{l}_{13}, \qquad {}^{W}\ddot{\boldsymbol{p}}_{B} = \alpha_2 \boldsymbol{l}_{12} + \beta_2 \boldsymbol{l}_{13}. \tag{3.65}$$

Hence using the elementary row operations, the first block column of $\boldsymbol{\mathcal{O}}_{\mathbf{3}\boldsymbol{R}}$ can be reduced to

$$ \boldsymbol{\mathcal{O}}'_{\mathbf{3}\boldsymbol{R}_{(:,1)}} = \begin{bmatrix} \mathbf{0}_{3\times3} & \mathbf{\Gamma}_{\mathbf{3}}^T & \mathbf{0}_{3\times3} & \mathbf{0}_{3\times3} & \mathbf{0}_{3\times3} & \mathbf{0}_{3\times3} \end{bmatrix}^T \tag{3.66}$$

The block column $\boldsymbol{\mathcal{O}}_{\mathbf{3}\boldsymbol{R}_{(:,1)}}$ has rank of two. Therefore the rank of the observability matrix becomes 14, and the system becomes unobservable.

---

[5] The Gibbs vector related to the rotation about the gravity vector can be expressed as $\lambda^* \boldsymbol{D}{}^{W}\boldsymbol{C}_{B}^{T}\boldsymbol{g}$ (See Appendix A). Since λ^* is a scalar, it does not affect the null vector ${}^{1}\boldsymbol{\mathcal{N}}_{(:,1)}$. Therefore, for the clarity of the presentation, λ^* is omitted throughout the thesis.

The null vector of $\mathbf{\Gamma_3}$ can be calculated as $(\boldsymbol{l}_{12} \times \boldsymbol{l}_{13})$, and therefor it is straight forward to show that the ${}^{2}\boldsymbol{\mathcal{N}}$ is the null vector of $\boldsymbol{\mathcal{O}}_{\mathbf{3}\boldsymbol{R}}$. $\square$

The null vector given in (3.64) shows that the unobservable direction under **Scenario 2** corresponds to the perpendicular direction to the plane of the three anchors. If the MAV is stationary while on the plane of the three anchors, the unobservable sub-space is spanned by $[\ {}^{1}\boldsymbol{\mathcal{N}}\ {}^{2}\boldsymbol{\mathcal{N}}\ ]$.

3.3.3.3 Scenario 3: MAV is flying parallel to the gravity with three range anchors

Lemma 3.4. *When the MAV is flying parallel to gravity, the three range assisted INS becomes unobservable. The unobservable sub-space is spanned by*

$$ {}^{3}\boldsymbol{\mathcal{N}} = \begin{bmatrix} \mathbf{0}_{1\times3} & \mathbf{0}_{1\times3} & \left(\boldsymbol{D}\,{}^{W}\boldsymbol{C}_{B}^{T}\boldsymbol{g}\right)^{T} & \mathbf{0}_{1\times3} & \mathbf{0}_{1\times3} \end{bmatrix}^{T}. \tag{3.67} $$

Proof. When the MAV is flying parallel to gravity, the velocity and the acceleration of the MAV can be expressed as

$$ {}^{W}\boldsymbol{v}_{B} = {}^{W}\boldsymbol{C}_{B}\,{}^{B}\boldsymbol{v} = \alpha \boldsymbol{g}, \qquad {}^{W}\ddot{\boldsymbol{p}}_{B} = \beta \boldsymbol{g}. \tag{3.68} $$

Substitute the conditions in (3.68) into $\boldsymbol{\mathcal{O}}_{\mathbf{3}\boldsymbol{R}}$, and consider the third column of the modified observability matrix $\boldsymbol{\mathcal{O}}_{\mathbf{3}\boldsymbol{R}_{\boldsymbol{S}\mathbf{3},(:,\mathbf{3})}}$

$$ \boldsymbol{\mathcal{O}}_{\mathbf{3}\boldsymbol{R}_{\boldsymbol{S}\mathbf{3},(:,\mathbf{3})}} = \begin{bmatrix} \mathbf{0}_{3\times3} & \mathbf{0}_{3\times3} & \left(\boldsymbol{K_d}\left\lfloor {}^{W}\boldsymbol{C}_{B}^{T}\boldsymbol{g}\right\rfloor_{\times}\boldsymbol{D}^{-1}\right)^{T} & \left(-\mathbf{\Gamma_3}\left(\lfloor \boldsymbol{g}\rfloor_{\times}\right)\left(\boldsymbol{D}^{T}\right)^{-1}\right)^{T} & \mathbf{\Theta}^{T} & \mathbf{\Lambda}_{\mathbf{3}_{\boldsymbol{S}\mathbf{3}}}^{T} \end{bmatrix}^{T}, \tag{3.69} $$

where $\boldsymbol{\Lambda}_{\boldsymbol{3}_{\boldsymbol{S3}}} = \boldsymbol{\Gamma}_{\boldsymbol{3}} \left(\lfloor \boldsymbol{g} \rfloor_{\times} \right) \left(\boldsymbol{D}^T \right)^{-1}$. The block column matrix $\boldsymbol{\mathcal{O}}_{\boldsymbol{3R_{S3,(:,3)}}}$ has a rank of 2, hence the system is locally weakly observable.

Similar to the proof in Lemma 3.2, it is straight forward to prove that $\left(\boldsymbol{D}^{W}\boldsymbol{C}_{B}^{T}\boldsymbol{g} \right)^T$ is the null vector of $\boldsymbol{\mathcal{O}}_{\boldsymbol{3R_{S3,(:,3)}}}$. Hence the unobservable sub-space under **Scenario 3** is spanned by ${}^{3}\boldsymbol{\mathcal{N}}$. □

Similar to **Scenario 1**, the null vector ${}^{3}\boldsymbol{\mathcal{N}}$ represents the rotation about the gravity vector. Therefore, when the MAV is flying parallel to gravity, any rotation about the gravity vector is unobservable.

3.3.4 *Case 2*: Two Range Assisted INS

Two range measurements are used in the measurement model of the RINS under *Case 2*, and therefore $j = 2$ in (3.51). The Lie derivatives of the output function and their gradients can be calculated as follows.

$$\mathfrak{L}^0\mathbf{h} = \mathbf{h}(\mathbf{x}) \tag{3.70}$$

$$\nabla\mathfrak{L}^0\mathbf{h} = \begin{bmatrix} \mathbf{0}_{3\times3} & -\boldsymbol{K_d} & \mathbf{0}_{3\times3} & \mathbf{0}_{3\times3} & \boldsymbol{I_3} \\ \boldsymbol{\Gamma_2} & \mathbf{0}_{3\times3} & \mathbf{0}_{3\times3} & \mathbf{0}_{3\times3} & \mathbf{0}_{3\times3} \end{bmatrix}, \tag{3.71}$$

where $\boldsymbol{\Gamma_2} \triangleq [\ {}^{W}\boldsymbol{r}_1\ {}^{W}\boldsymbol{r}_2\ ]^T$.

$$\mathfrak{L}^1_{\mathbf{f_0}}\mathbf{h} = \nabla\mathfrak{L}^0\mathbf{h} \cdot \mathbf{f_0} = \begin{bmatrix} \boldsymbol{K_d}{}^{B}\dot{\boldsymbol{v}}' \\ \boldsymbol{\Gamma_2}{}^{W}\boldsymbol{C}_{B}{}^{B}\boldsymbol{v} \end{bmatrix}, \tag{3.72}$$

$$\nabla \mathfrak{L}^{1}_{\mathbf{f_0}}\mathbf{h} =$$

$$\begin{bmatrix} \mathbf{0}_{3\times3} & \boldsymbol{K_d}\left(\boldsymbol{K_d} - \lfloor {}^{B}\boldsymbol{b}_g \rfloor_{\times}\right) & \boldsymbol{K_d}\left\lfloor {}^{W}\boldsymbol{C}_{B}^{T}\boldsymbol{g} \right\rfloor_{\times} \boldsymbol{D}^{-1} & \boldsymbol{K_d}\lfloor {}^{B}\boldsymbol{v} \rfloor_{\times} & -\boldsymbol{K_d}\boldsymbol{I}_{33} \\ \boldsymbol{V_2}{}^{W}\boldsymbol{C}_{B}^{T} & \boldsymbol{\Gamma_2}{}^{W}\boldsymbol{C}_{B} & -\boldsymbol{\Gamma_2}\lfloor {}^{W}\boldsymbol{C}_{B}{}^{B}\boldsymbol{v} \rfloor_{\times}\left(\boldsymbol{D}^{T}\right)^{-1} & \mathbf{0}_{3\times3} & \mathbf{0}_{3\times3} \end{bmatrix}, \tag{3.73}$$

where $\boldsymbol{V_2} = [\ {}^{B}\boldsymbol{v},\ {}^{B}\boldsymbol{v}\ ]^{T}$.

$$\mathfrak{L}^{2}_{\mathbf{f_0}\mathbf{f_0}}\mathbf{h} = \nabla \mathfrak{L}^{1}_{\mathbf{f_0}}\mathbf{h}\cdot\mathbf{f_0} = \begin{bmatrix} \boldsymbol{K_d}\left(\boldsymbol{K_d} - \lfloor {}^{B}\boldsymbol{b}_g \rfloor_{\times}\right){}^{B}\dot{\boldsymbol{v}} - \boldsymbol{K_d}\left\lfloor {}^{W}\boldsymbol{C}_{B}^{T}\boldsymbol{g} \right\rfloor_{\times}{}^{B}\boldsymbol{b}_g \\ \boldsymbol{V_2}{}^{B}\boldsymbol{v} + \boldsymbol{\Gamma_2}{}^{W}\boldsymbol{C}_{B}{}^{B}\dot{\boldsymbol{v}}' + \boldsymbol{\Gamma_2}{}^{W}\boldsymbol{C}_{B}\lfloor {}^{B}\boldsymbol{v} \rfloor_{\times}{}^{B}\boldsymbol{b}_g \end{bmatrix} \tag{3.74}$$

$$\nabla \mathfrak{L}^{2}_{\mathbf{f_0}\mathbf{f_0}}\mathbf{h} = \begin{bmatrix} \mathbf{0}_{3\times3} & -\boldsymbol{K_d}\left(\lfloor {}^{B}\boldsymbol{b}_g \rfloor_{\times} - \boldsymbol{K_d}\right)^{2} & \boldsymbol{\Theta} & \boldsymbol{\Phi} & \boldsymbol{K_d}\left(\lfloor \boldsymbol{K_d} - {}^{B}\boldsymbol{b}_g \rfloor_{\times}\right)\boldsymbol{I}_{33} \\ \boldsymbol{\Upsilon_2} & 2\boldsymbol{V_2} - \boldsymbol{\Gamma_2}{}^{W}\boldsymbol{C}_{B}\boldsymbol{K_d} & \boldsymbol{\Lambda_2} & \mathbf{0}_{3\times3} & \boldsymbol{\Gamma_2}{}^{W}\boldsymbol{C}_{B}\boldsymbol{I}_{33} \end{bmatrix}, \tag{3.75}$$

where

$$\boldsymbol{\Lambda_2} = \boldsymbol{\Gamma_2}\left(\lfloor {}^{W}\boldsymbol{C}_{B}(\boldsymbol{K_d}{}^{B}\boldsymbol{v} - b_{az}\grave{\boldsymbol{e}}_{\mathbf{3}}) \rfloor_{\times}\right)\left(\boldsymbol{D}^{T}\right)^{-1}$$

$$\boldsymbol{\Upsilon_2} = [\ {}^{W}\ddot{\boldsymbol{p}}_{B}\ {}^{W}\ddot{\boldsymbol{p}}_{B}\ ]^{T}.$$

The nonlinear observability matrix for the *Case 2*, $\boldsymbol{\mathcal{O}}_{\boldsymbol{2R}}$ can be constructed using (3.71), (3.73), (3.75) as

$$\boldsymbol{\mathcal{O}}_{\boldsymbol{2R}} = \begin{bmatrix} \nabla \mathfrak{L}^{0}\mathbf{h} \\ \nabla \mathfrak{L}^{1}_{\mathbf{f_0}}\mathbf{h} \\ \nabla \mathfrak{L}^{2}_{\mathbf{f_0}\mathbf{f_0}}\mathbf{h} \end{bmatrix}. \tag{3.76}$$

$$\boldsymbol{\mathcal{O}}_{\boldsymbol{2R}} = \begin{bmatrix} \mathbf{0}_{3\times3} & -\boldsymbol{K_d} & \mathbf{0}_{3\times3} & \mathbf{0}_{3\times3} & \boldsymbol{I_3} \\ \boldsymbol{\Gamma_2} & \mathbf{0}_{3\times3} & \mathbf{0}_{3\times3} & \mathbf{0}_{3\times3} & \mathbf{0}_{3\times3} \\ \mathbf{0}_{3\times3} & \boldsymbol{K_d}\left(\boldsymbol{K_d} - \lfloor {}^{B}\boldsymbol{b}_g \rfloor_\times\right) & \boldsymbol{K_d}\left\lfloor {}^{W}\boldsymbol{C}_{B}^{T}\boldsymbol{g} \right\rfloor_\times \boldsymbol{D}^{-1} & \boldsymbol{K_d}\lfloor {}^{B}\boldsymbol{v} \rfloor_\times & \boldsymbol{K_d}\boldsymbol{I}_{33} \\ \boldsymbol{V_2}{}^{W}\boldsymbol{C}_{B}^{T} & \boldsymbol{\Gamma_2}{}^{W}\boldsymbol{C}_{B} & -\boldsymbol{\Gamma_2}\lfloor {}^{W}\boldsymbol{C}_{B}{}^{B}\boldsymbol{v} \rfloor_\times \left(\boldsymbol{D}^{T}\right)^{-1} & \mathbf{0}_{3\times3} & \mathbf{0}_{3\times3} \\ \mathbf{0}_{3\times3} & -\boldsymbol{K_d}\left(\lfloor {}^{B}\boldsymbol{b}_g \rfloor_\times - \boldsymbol{K_d}\right)^2 & \boldsymbol{\Theta} & \boldsymbol{\Phi} & \boldsymbol{K_d}\left(\boldsymbol{K_d} - \lfloor {}^{B}\boldsymbol{b}_g \rfloor_\times\right)\boldsymbol{I}_{33} \\ \boldsymbol{\Upsilon_2} & 2\boldsymbol{V_2} - \boldsymbol{\Gamma_2}{}^{W}\boldsymbol{C}_{B}\boldsymbol{K_d} & \boldsymbol{\Lambda_2} & \mathbf{0}_{3\times3} & \boldsymbol{\Gamma_2}{}^{W}\boldsymbol{C}_{B}\boldsymbol{I}_{33} \end{bmatrix}. \tag{3.77}$$

Lemma 3.5. *The RINS with two range measurements is locally weakly observable when 1) MAV is nonstationary 2) MAV is not flying on the plane generated by the MAV and the two anchors. 3)* ${}^{B}\boldsymbol{v} \nparallel {}^{W}\boldsymbol{C}_{B}^{T}\boldsymbol{g}$.

Proof. The rank of the observability matrix in (3.77) is determined by calculating the rank of each block column of the matrix $\boldsymbol{\mathcal{O}}_{\boldsymbol{2R}}$. Consider the non zero matrices of the first block column of $\boldsymbol{\mathcal{O}}_{\boldsymbol{2R}}$.

$$\boldsymbol{\mathcal{O}}'_{\boldsymbol{2R(:,1)}} = \begin{bmatrix} \boldsymbol{\Gamma}_{\boldsymbol{2}}^{T} & (\boldsymbol{V_2}{}^{W}\boldsymbol{C}_{B}^{T})^{T} & \boldsymbol{\Upsilon}_{\boldsymbol{2}}^{T} \end{bmatrix}^{T}$$

It is straightforward to show that $\boldsymbol{\mathcal{O}}'_{\boldsymbol{2R(:,1)}}$ has full rank when MAV is moving in any direction that is not along the plane generated by the MAV and the two anchors. Following a similar approach of proofing Lemma 3.1, it can be shown that the block columns three, four, and five have full rank if the MAV trajectory satisfies the conditions given in this Lemma. □

3.3.5 Unobservable Scenarios of *Case 2*

This section focuses on three trajectories that causes the two range assisted INS to become unobservable and identify the unobservable directions for each trajectory.

3.3.5.1 Scenario 4: MAV is stationary with two range anchors

Lemma 3.6. *When the MAV is stationary in the two range assisted INS, the RINS becomes unobservable, and the unobservable sub-space is spanned by*

$$
{}^{4}\boldsymbol{\mathcal{N}} = \begin{bmatrix} \mathbf{0}_{3\times1} & \mathbf{0}_{3\times1} & ({}^{W}\boldsymbol{r}_1 \times {}^{W}\boldsymbol{r}_2) \\ \mathbf{0}_{3\times1} & \mathbf{0}_{3\times1} & \mathbf{0}_{3\times1} \\ \boldsymbol{D}{}^{W}\boldsymbol{C}_{B}^{T}\boldsymbol{g} & \mathbf{0}_{3\times1} & \mathbf{0}_{3\times1} \\ \mathbf{0}_{3\times1} & b_{az}\grave{\boldsymbol{e}}_{\mathbf{3}} & \mathbf{0}_{3\times1} \\ \mathbf{0}_{3\times1} & \mathbf{0}_{3\times1} & \mathbf{0}_{3\times1} \end{bmatrix}. \tag{3.78}
$$

Proof. A stationary MAV has zero velocity and acceleration, and the thrust is in the direction of gravity. Hence the observability matrix for **Scenario 4** can be expressed as

$$
\boldsymbol{\mathcal{O}}_{\boldsymbol{2R_{S2}}} =
$$

$$
\begin{bmatrix} \mathbf{0}_{3\times3} & -\boldsymbol{K_d} & \mathbf{0}_{3\times3} & \mathbf{0}_{3\times3} & \boldsymbol{I_3} \\ \boldsymbol{\Gamma_2} & \mathbf{0}_{3\times3} & \mathbf{0}_{3\times3} & \mathbf{0}_{3\times3} & \mathbf{0}_{3\times3} \\ \mathbf{0}_{3\times3} & \boldsymbol{K_d}\left(\boldsymbol{K_d} - \lfloor{}^{B}\boldsymbol{b}_g\rfloor_{\times}\right) & \boldsymbol{K_d}\left\lfloor{}^{W}\boldsymbol{C}_{B}^{T}\boldsymbol{g}\right\rfloor_{\times}\boldsymbol{D}^{-1} & \mathbf{0}_{3\times3} & \boldsymbol{K_d}\boldsymbol{I}_{33} \\ \mathbf{0}_{3\times3} & \boldsymbol{\Gamma_2}{}^{W}\boldsymbol{C}_{B} & \mathbf{0}_{3\times3} & \mathbf{0}_{3\times3} & \mathbf{0}_{3\times3} \\ \mathbf{0}_{3\times3} & -\boldsymbol{K_d}\left(\lfloor{}^{B}\boldsymbol{b}_g\rfloor_{\times} - \boldsymbol{K_d}\right)^{2} & \boldsymbol{\Theta} & -\boldsymbol{K_d}\lfloor(b_{az}\grave{\boldsymbol{e}}_{\mathbf{3}})\rfloor_{\times} & \boldsymbol{K_d}\left(\boldsymbol{K_d} - \lfloor{}^{B}\boldsymbol{b}_g\rfloor_{\times}\right)\boldsymbol{I}_{33} \\ \mathbf{0}_{3\times3} & -\boldsymbol{\Gamma_2}{}^{W}\boldsymbol{C}_{B}\boldsymbol{K_d} & \boldsymbol{\Lambda_{2_{S4}}} & \mathbf{0}_{3\times3} & \boldsymbol{\Gamma_2}{}^{W}\boldsymbol{C}_{B}\boldsymbol{I}_{33} \end{bmatrix}, \tag{3.79}
$$

where,

$$\boldsymbol{\Lambda}_{\mathbf{2}_{\boldsymbol{S4}}} = -\boldsymbol{\Gamma}_{\mathbf{2}} \left(\lfloor \boldsymbol{g} \rfloor_{\times} \right) \left(\boldsymbol{D}^{T} \right)^{-1}.$$

It is straightforward to show that the first, third, and fourth block columns of $\boldsymbol{\mathcal{O}}_{\mathbf{2}\boldsymbol{R}_{\boldsymbol{S2}}}$ each has a rank of 2. Hence the RINS is unobservable when the MAV is stationary.

Following the steps of Lemma 3.2, it can be shown that the first two columns of the null vector ${}^{4}\boldsymbol{\mathcal{N}}$ span the unobservable sub-space of the system. $\boldsymbol{\Gamma}_{\mathbf{2}}$ has a null vector of ${}^{W}\boldsymbol{r}_1 \times {}^{W}\boldsymbol{r}_2$. Therefore, it is straightforward to show that the third column of ${}^{4}\boldsymbol{\mathcal{N}}$ spans the unobservable sub-space of the RINS under **Scenario 4**. □

The null vector given in (3.78) shows that the three unobservable directions under **Scenario 4** correspond to the rotation about the gravity vector, gyroscope bias along z axis of $\{B\}$, and the perpendicular direction to the plane created by the MAV and the two anchors.

3.3.5.2 Scenario 5: MAV is flying on the plane of the MAV and the two anchors

Lemma 3.7. *When the MAV is flying on the plane generated by the MAV and the two anchors, the RINS is unobservable, and the unobservable sub-space is spanned by*

$${}^{5}\boldsymbol{\mathcal{N}} = \left[({}^{W}\boldsymbol{r}_1 \times {}^{W}\boldsymbol{r}_2)^{T},\ \mathbf{0}_{1\times 3},\ \mathbf{0}_{1\times 3},\ \mathbf{0}_{1\times 3},\ \mathbf{0}_{1\times 3} \right]^{T}. \tag{3.80}$$

Proof. When the MAV is flying on the plane of the anchors, the velocity and the acceleration of the MAV can be expressed as

$${}^{W}\boldsymbol{v}_{B} = {}^{W}\boldsymbol{C}_{B}{}^{B}\boldsymbol{v} = \alpha_1 {}^{W}\boldsymbol{r}_1 + \beta_1 {}^{W}\boldsymbol{r}_2, \qquad {}^{W}\ddot{\boldsymbol{p}}_{B} = \alpha_2 {}^{W}\boldsymbol{r}_1 + \beta_2 {}^{W}\boldsymbol{r}_2. \tag{3.81}$$

By substituting the relations into $\boldsymbol{V}_{\mathbf{2}}$, and $\boldsymbol{\Upsilon}_{\mathbf{2}}$ it is straight forward to show that

$({}^{W}\boldsymbol{r}_1 \times {}^{W}\boldsymbol{r}_2)$ is the null vector of the first column of $\boldsymbol{\mathcal{O}}_{\boldsymbol{2R}}$. Hence the ${}^{5}\boldsymbol{\mathcal{N}}$ spans the unobservable sub-space of the RINS under **Scenario 5**. □

3.3.5.3 Scenario 6: MAV is flying parallel to the gravity with two range anchors

Lemma 3.8. *When the MAV is flying parallel to gravity, the two range assisted INS becomes unobservable. The unobservable sub-space is spanned by*

$$ {}^{3}\boldsymbol{\mathcal{N}} = \begin{bmatrix} \mathbf{0}_{1\times 3} & \mathbf{0}_{1\times 3} & \left(\boldsymbol{D}^{W}\boldsymbol{C}_{B}^{T}\boldsymbol{g}\right)^{T} & \mathbf{0}_{1\times 3} & \mathbf{0}_{1\times 3} \end{bmatrix}^{T}. \tag{3.82} $$

Proof. The proof is similar to that of Lemma 3.4. □

Table 3.1 summarize the results of the observability analysis of three and two range assisted INS.

3.4 Simulation Results

A MATLAB simulator was developed using the measured physical parameters of the AscTec Hummingbird quadrotor MAV to validate the observability conditions identified in section 3.3. The IMU and range measurements were modelled as in (3.42), (3.43), and the noise characteristics were obtained using experimental data. Noise characteristics of the IMU and range measurements used for the simulation are shown in Table 3.2. All the unobservable modes of orientation are the rotation about the gravity vector. The velocity and acceleration conditions of the corresponding scenarios enforce that the MAV is horizontal; hence the rotation about the gravity vector can be interpreted as a change in the yaw angle of the MAV. Therefore the Euler angles are used to visualize the estimated orientation of the MAV. The estimated

Table 3.1: Summary of the observability analysis of three and two range assisted INS

Case	**Scenario**	**Unobservable Directions**
Case 1: Three range measurements	**Scenario 1:** Hovering	• Rotation about gravity vector • Gyroscope bias along z axis
	Scenario 2: Flying on the plane of the three anchors	• Position perpendicular to the plane of the three anchors
	Scenario 3: Vertical flight	• Rotation about gravity vector • Gyroscope bias along ${}^{B}\boldsymbol{v}$
Case 2: Two range measurements	**Scenario 4:** Hovering	• Position perpendicular to the plane of the MAV and two anchors • Rotation about gravity vector, • Gyroscope bias along z axis
	Scenario 5: Flying on the plane of the MAV and the two anchors	• Position perpendicular to the plane of the MAV and two anchors
	Scenario 6: Vertical flight	• Rotation about the gravity vector • Gyroscope bias along ${}^{B}\boldsymbol{v}$

Table 3.2: IMU and Range Noise Figures

Measurement	Noise Density
Acceleration	2.08×10^{-3} $(\mathrm{ms}^{-2}/\sqrt{\mathrm{Hz}})$
Angular Velocity	5.088×10^{-4} $({}^\circ\mathrm{s}^{-1}/\sqrt{\mathrm{Hz}})$
Accelerometer Bias	3.0×10^{-5} $(\mathrm{ms}^{-3}/\sqrt{\mathrm{Hz}})$
Gyroscope Bias	2.657×10^{-5} $({}^\circ\mathrm{s}^{-2}/\sqrt{\mathrm{Hz}})$
UWB Range	1.04×10^{-2} $(\mathrm{m}/\sqrt{\mathrm{Hz}})$

quaternions and the estimation covariances are used to calculate the corresponding Euler angles and their covariances. For a better illustration of the unobservable modes, the simulated trajectories were divided into two parts. For the first part, the MAV was flown along a circular trajectory with varying altitude during the first 50 seconds.

As for the second portion of the simulation, the MAV was flown along a straight line, vertically or kept stationary for another 50 seconds depending on the scenario. Fig. 3.2 shows the three different trajectories used to simulate the unobservable modes.

The covariance matrix $\mathbf{P}$ [see (4.17)] represents the confidence level of the estimation. The diagonal elements of $\mathbf{P}$ correspond to the variance of each estimated error state, and the standard deviation is represented by σ. The 3σ boundary represents the 99% confident boundary of the estimation. During an unobservable scenario, the estimator does not have sufficient information to estimate the states along the unobservable direction. Hence the 3σ boundary of the error states along the unobservable direction diverge.

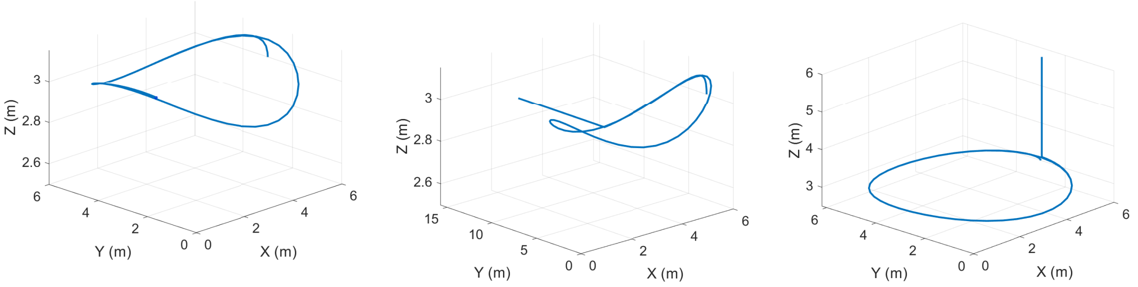

(a) (b) (c)

Fig. 3.2: Trajectories used for the three and two range assisted INS simulation. (a) Circular trajectory with varying altitude, (b) Circular trajectory with varying altitude and straight line, (c) Circular trajectory with varying altitude and vertical climb

3.4.1 *Case 1*: RINS with three range measurements

The simulated circular trajectory is shown in Fig. 3.2a, and the estimator was run with five different anchor constellations, each containing three anchors. The anchor positions are randomly selected, and the locations of the anchors are shown in Table 3.3. Fig. 3.3 shows the total position and the total angle estimation errors for the five range constellations. This shows that when the MAV is flying in an observable trajectory, the proposed RINS with three range measurements can estimate the pose of the MAV with good accuracy irrespective of the anchor locations.

Table 3.3: Anchor Locations for *Case 1*

	Anchor 1 (m)	Anchor 2 (m)	Anchor 3 (m)
Constellation 1	(4.2, 7.2, 0)	(3.0, 1.5, 0.9)	(1.9, 3.5, 4.0)
Constellation 2	(7.4, 3.9, 6.7)	(7.3, 7.7, 1.3)	(8.7, 1.3, 9.5)
Constellation 3	(6.2, 6.0, 2.5)	(7.4, 4.8, 8.6)	(1.2, 6.3, 3.0)
Constellation 4	(5.3, 8.2, 3.9)	(2.7, 9.4, 7.3)	(7.7, 4.0, 5.0)
Constellation 5	(0.1, 6.5, 1.8)	(7.6, 5.1, 2.6)	(8.8, 9.8, 8.3)

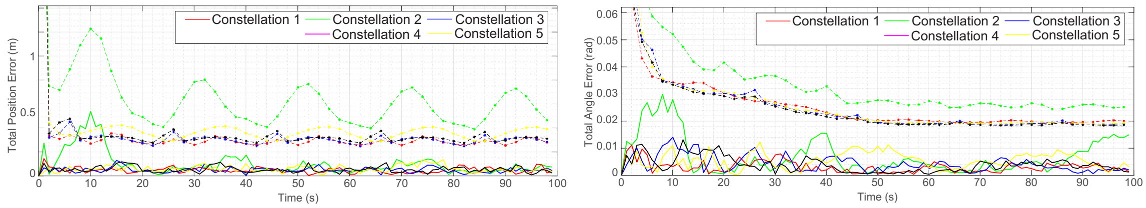

(a) (b)

Fig. 3.3: *Case 1*: Localization using three range measurements, (a) Total Position error and 3σ boundary, (b) Total Angle Error and 3σ boundary. (—) is total error, and (-$*$-) is 3σ boundary.

25 Monte-Carlo simulations were conducted with the anchor constellations in Table 3.3. Due to space limitations, the Mean Absolute Error (MAE) of estimates and the average 3σ of the simulation with constellation 1 are shown in Fig. 3.4. This shows that all the estimation errors are bounded and well within the 3σ boundary under *Case 1*. The covariance values of the estimates depends on the position of the MAV relative to the anchor locations. Since the MAV is flying in a circular trajectory, a repeating pattern can be seen in the estimation covariances. This phenomenon is clearly visible in the position covariance in Fig. 3.4a

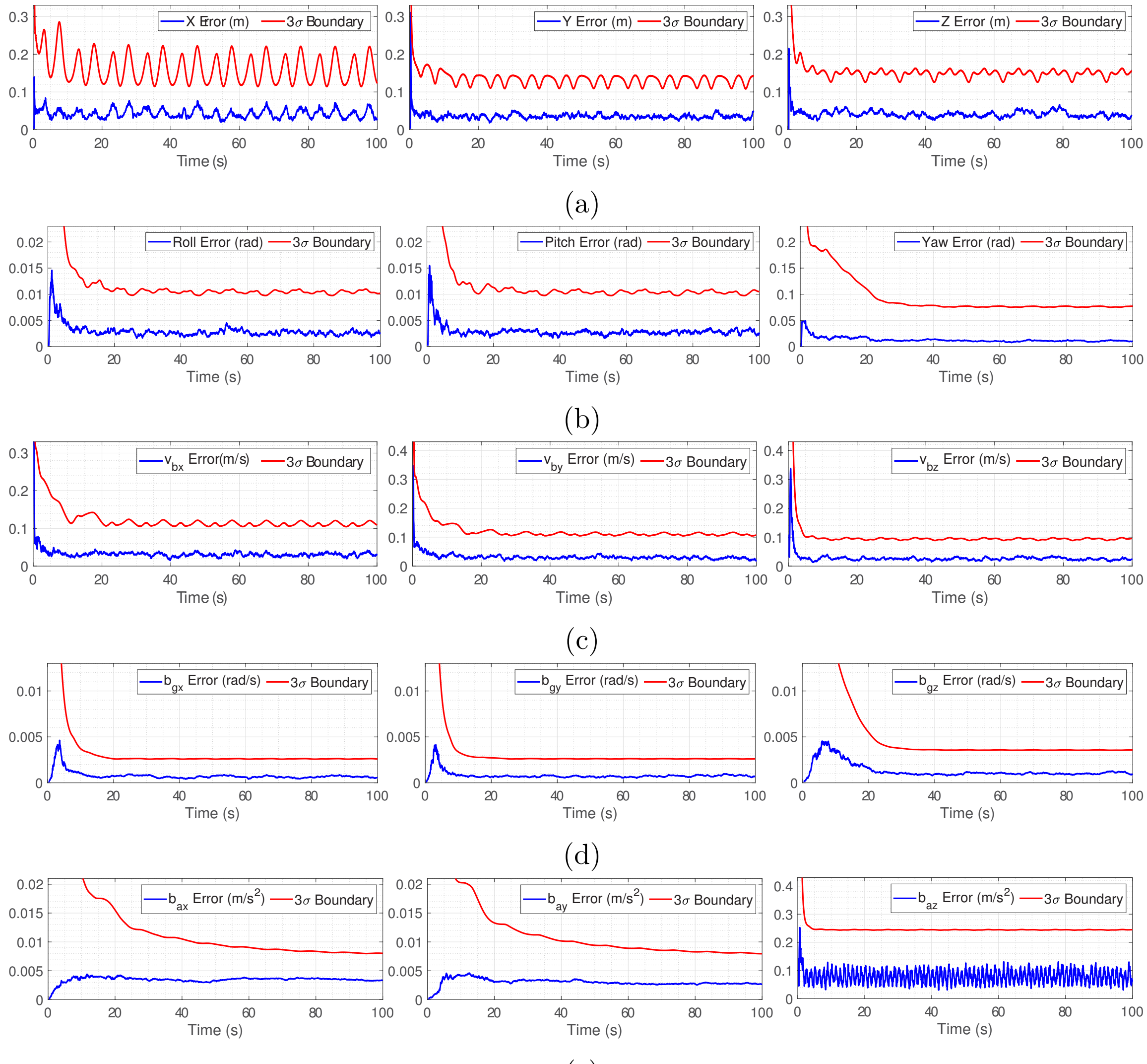

Fig. 3.4: *Case 1*: Localization using three range anchors in Constellation 1, 25 Monte-Carlo simulations conducted. MAE and 3σ boundary of (a) Position, (b) Orientation, (c) Body frame velocity, (d) Gyroscope bias, (e) Accelerometer bias.

3.4.2 *Case 2*: RINS with two range measurements

Similar to *Case 1*, I ran the simulation with five range anchor constellations for the case with two range measurements. Each constellation contains two anchors and the anchor locations are shown in Table 3.4. Fig. 3.5a and Fig. 3.5b shows the total position and total angle errors along with corresponding 3σ error boundary for each anchor constellation.

Table 3.4: Anchor Locations for *Case 2*

	Anchor 1 (m)	Anchor 2 (m)
Constellation 1	(7.1, 7.5, 2.8)	(6.8, 6.6, 1.6)
Constellation 2	(1.2, 5.0, 9.6)	(3.4, 5.9, 2.2)
Constellation 3	(7.5, 2.6, 5.1)	(7.0, 8.9, 9.6)
Constellation 4	(5.5, 1.4, 1.5)	(2.6, 8.4, 2.5)
Constellation 5	(0.1, 2.4, 9.3)	(3.5, 2.0, 2.5)

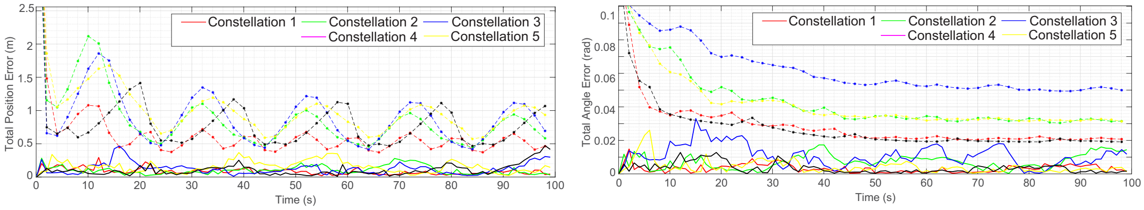

(a) (b)

Fig. 3.5: *Case 2*: Localization using two range measurements, (a) Total Position error and 3σ boundary, (b) Total Angle Error and 3σ boundary. (—) is total error, and (-$*$-) is 3σ boundary.

25 Monte-Carlo simulations are conducted with each constellation in Table 3.4. Fig. 3.6 shows the MAEs and average 3σ boundaries of the simulations with Constellation 1. The estimation errors of *Case 2* are larger than the errors in *Case 1*. However, all the errors are bounded and well within the 3σ confidence level.

It can be seen that the total error values in both cases lie within the 3σ boundary, and the covariances remain bounded as expected since non of the unobservable conditions are met during the flight. It can be seen that the proposed estimator is able to estimate the position and orientation of the MAV with three and two range measurements. The total estimation errors are bounded well within the 3σ boundary.

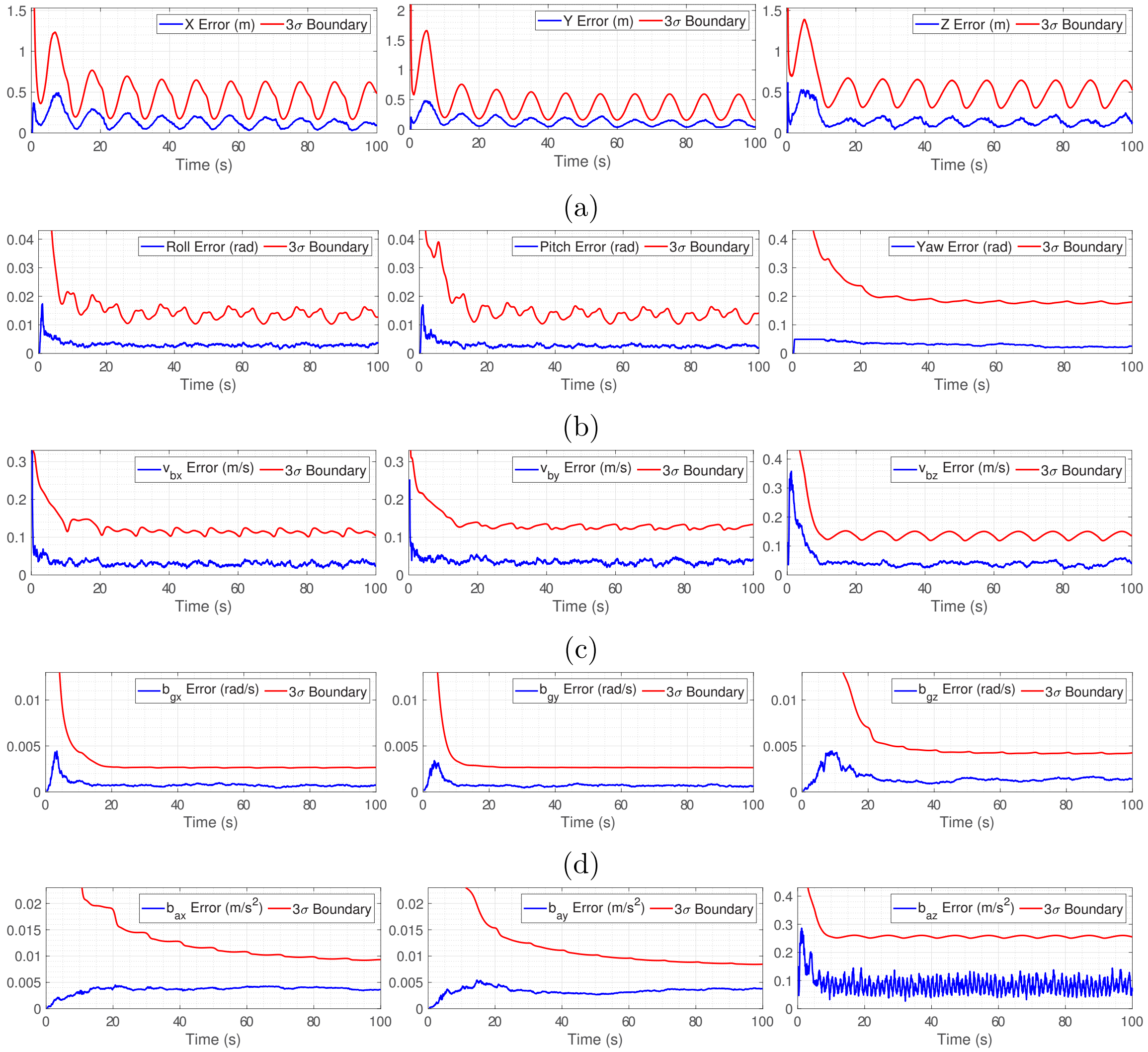

(a)

(b)

(c)

(d)

(e)

Fig. 3.6: *Case 2*, 25 Monte-Carlo simulations: Constellation 1, MAE and 3σ boundary (a) Position, (b) Orientation, (c) Body frame velocity, (d) Gyroscope bias, (e) Accelerometer bias.

3.4.3 Unobservable Scenarios

Simulations of Scenario 1 to Scenario 3 use the same anchor constellation. The three anchors are located at $(3, -1, 0)$ m, $(3, 7, 5)$ m, $(3, 0, 7)$ m. The x coordinate is selected to be fixed, and the rest of the coordinates are selected randomly. The range anchors are located on the $y-z$ plane so that the unobservable modes in position estimate will align with the x axis of $\{W\}$. This does not change the observability conditions but allows a clear presentation of the unobservable modes. Scenarios 4 to 6 require two range measurements, and therefore the first two anchors of the previous constellation are used as the range anchors. The simulation results show the MAE of the estimates of 25 Monte-Carlo simulations and the average of 3σ boundary.

Scenario 1: MAV is stationary with three range anchors: For this scenario, the MAV was kept stationary during the second portion of the simulation. The analysis shows that when the MAV is stationary with three range measurements, rotation about the gravity vector, under these conditions, the yaw angle, and the gyroscope bias along the z axis of $\{B\}$are unobservable modes. Fig. 3.7 shows the errors of the entire trajectory, circular portion, and stationary portion. The figures for the rest of the scenarios will show only the last 50 s of the simulation.

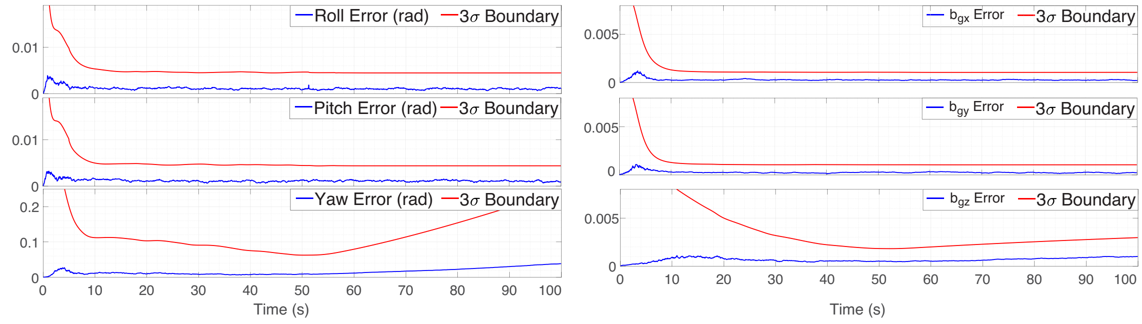

(a) (b)

Fig. 3.7: **Scenario 1**: MAV is stationary with three range anchors, Estimation errors, and 3σ boundary. (a) Orientation error, (b) Gyroscope bias error.

Fig. 3.7a shows the angle error and the 3σ error boundary for Scenario 1, and it can be seen that after the first 50 s, the covariance of the yaw estimation diverge rapidly, which shows that the yaw angle is an unobservable mode. Fig. 3.7b shows the gyroscope bias error and the 3σ error boundary. It can be seen that there is a slight divergence in the covariance of the z component of the gyroscope bias estimate. Since the gyroscope is modeled as a slow varying random walk process, the change of the covariance is not significant during the 50 second simulation period.

Scenario 2: MAV is flying on the plane of the three range anchor: In this scenario, the MAV follows the trajectory shown in Fig. 3.2b, and the velocity and acceleration of the MAV are on the plane of the three range anchors. The position of the MAV in the direction perpendicular to the plane is the unobservable mode. Fig. 3.8 shows the position error and the 3σ error boundary. It is clear that the covariance of the x estimate diverges significantly since x direction is perpendicular to the plane of the anchors.

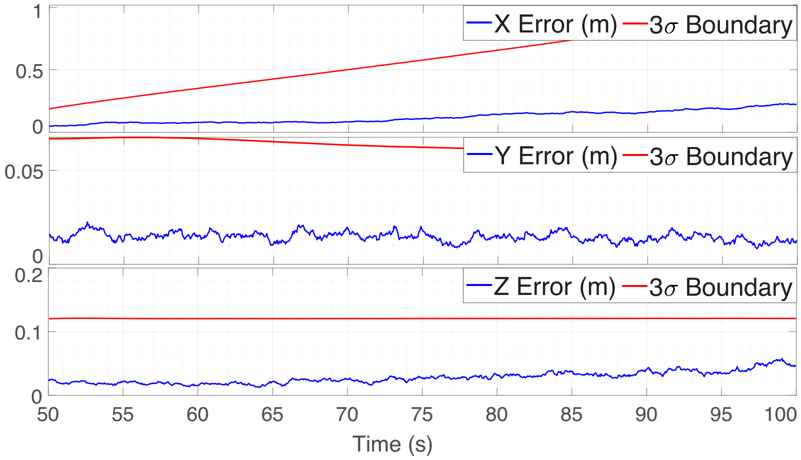

Fig. 3.8: **Scenario 2**: MAV is flying on the plane of the three anchors. Position estimation error and 3σ boundary,

Scenario 3: MAV is flying parallel to the gravity with three range anchors: In this scenario, the MAV transitions from the circular trajectory to a vertical climb at 50 seconds. According to the theoretical analysis, the rotation about gravity vector, i.e, yaw angle, is an unobservable mode. It is visible in Fig. 3.9 where the covariance of the yaw estimation diverges rapidly.

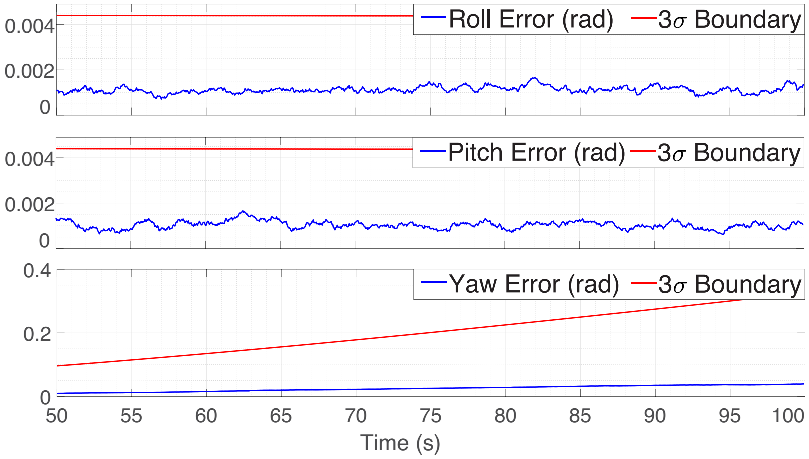

Fig. 3.9: **Scenario 3**: MAV is flying vertically with three range anchors. Orientation estimation error and 3σ boundary.

Scenario 4: MAV is stationary with two range anchors: In scenario 4, the MAV is hovering at $(3, 6, 3.1)$ m such that the anchors and the MAV lie on the $y - z$ plane. According to the analysis, the position of the MAV becomes unobservable in the direction perpendicular to the plane of the MAV and the two anchors, which in this configuration is the x direction.

Fig. 3.10a shows the position error and the 3σ error boundary. It can be seen that the covariance of the x estimate diverges rapidly, which can be interpreted as the position along the x axis is unobservable. Furthermore, the covariance of the y estimate also diverges but at a much lower rate, and this behavior can be attributed to the errors in position estimation. Due to the errors, the plane of the estimated MAV position and the two anchors is not parallel with the $y - z$ plane, and therefore the normal direction to the estimated plane has a component in the y direction.

In addition to the position being unobservable, the yaw angle and the gyroscope bias in the z direction are also unobservable. Fig. 3.10b shows that the covariance of the yaw estimation diverges rapidly; therefore, it confirms the theoretical calculation. In Fig. 3.10c we can see a slight divergence in the covariance of the z direction estimation of gyroscope bias as well.

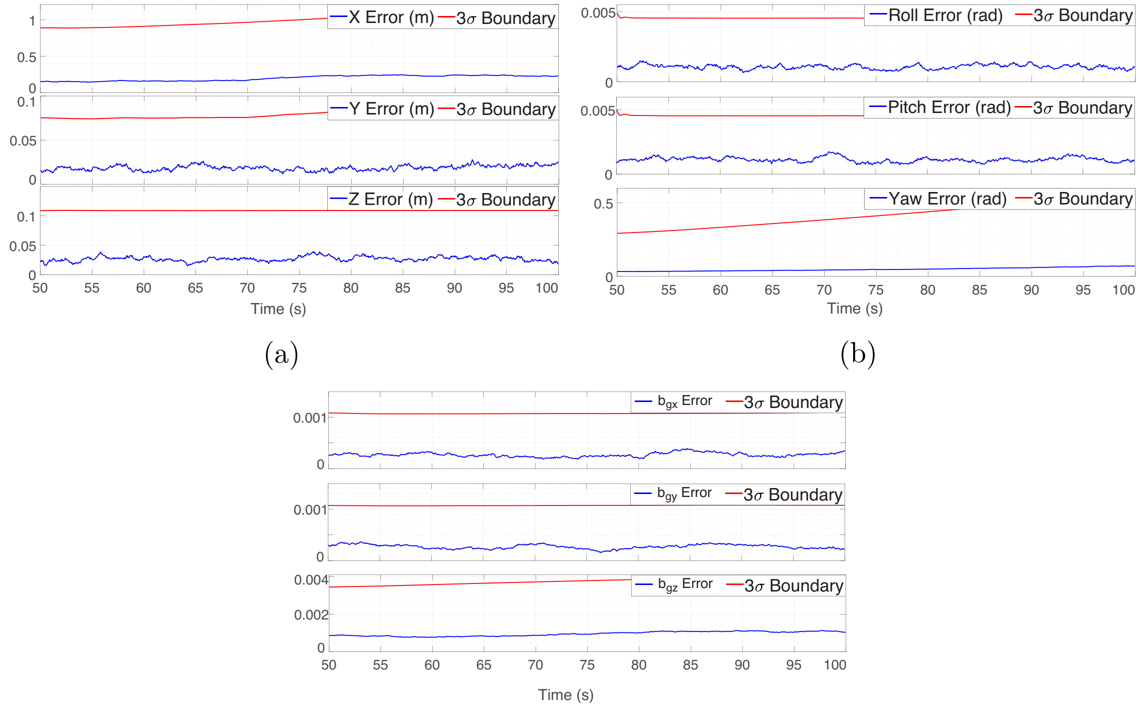

(a) (b)

(c)

Fig. 3.10: **Scenario 4**: MAV is stationary with two range measurements, Estimation errors, and 3σ boundary. (a) Position error, (b) Orientation error, (c) Gyroscope bias error.

Scenario 5: MAV is flying on the plane of the MAV and the two anchors: For this scenario, the MAV is flown in the trajectory shown in Fig. 3.2b such that the plane of the MAV and the two anchors is parallel to the $y-z$ plane. Fig. 3.11 shows that the covariance of the x estimate, perpendicular to the $y-z$ plane diverges rapidly, confirming the unobservable modes of Scenario 5. Similar to position estimation in Scenario 4, the covariances for y and z estimates diverge slightly due to the errors in the estimated position of the MAV which results in the plane between MAV and two anchors to be not parallel to the $y-z$ plane.

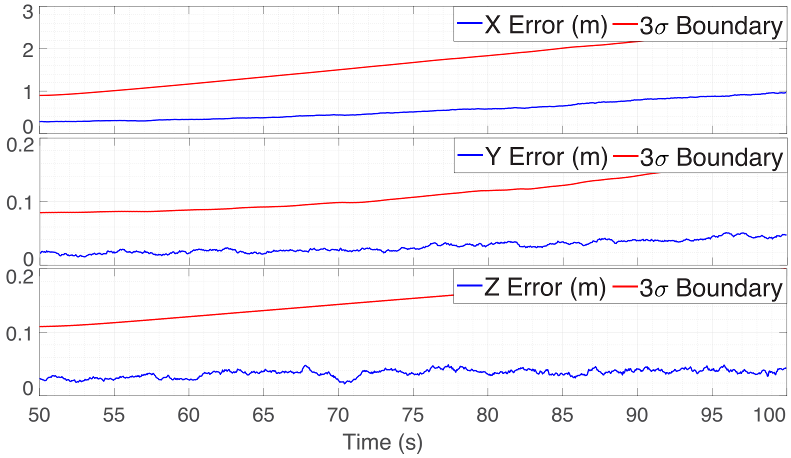

Fig. 3.11: **Scenario 5**: MAV is flying on the plane of the MAV and the two range anchors. Position estimation error and 3σ boundary

Scenario 6: MAV is flying parallel to the gravity with two range anchors: In this scenario, the MAV starts flying vertically on the trajectory shown in Fig. 3.2c. According to the theoretical analysis, the rotation about the gravity vector axis is unobservable. This can be seen in Fig. 3.12, where the covariance of the yaw estimate increase while the covariances of roll and pitch estimate stay constant.

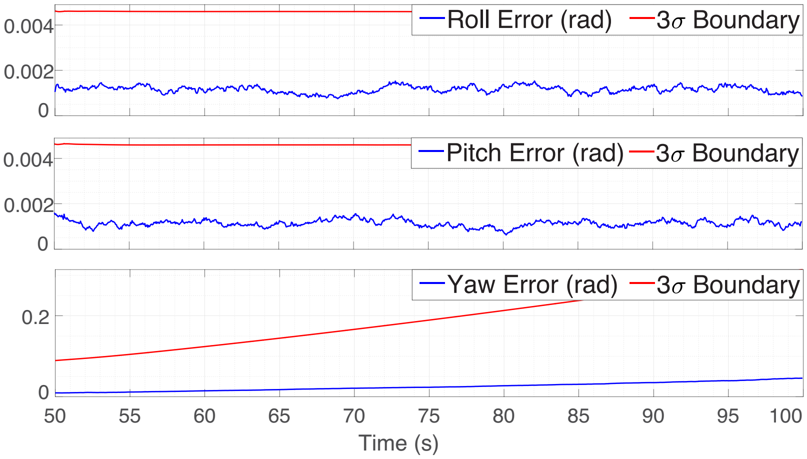

Fig. 3.12: **Scenario 6**: MAV is flying vertically with two range anchors. Orientation estimation error and 3σ boundary

3.5 Experimental Results

The main objective of the experiment is to validate the proposed INS's ability to localize the quadrotor MAV with two or three range measurements under real world conditions. The trajectory of the MAV and the placement of the anchors are decided such that the unobservable conditions identified in the observability analysis are not invoked. The MAV follows a circular trajectory with a constant height, and the range anchors are placed such that the height of the range anchors are not same as height of the trajectory.

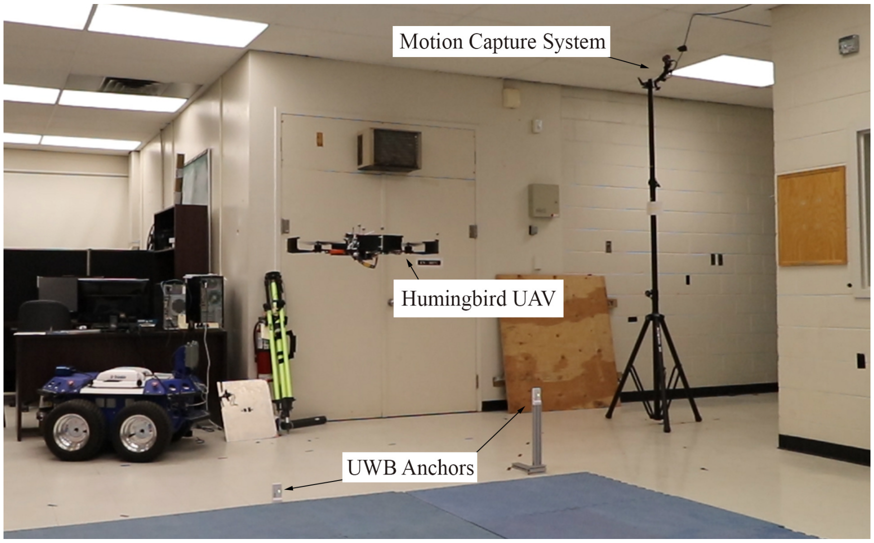

Fig. 3.13: Experimental setup

The experiments are carried out using an Ascending Technologies Hummingbird quadrotor with its factory programmed attitude controller. A high-level trajectory controller is implemented using the Robotic Operating System (ROS) to fly the quadrotor along the desired trajectory. The trajectory controller uses the differential flatness property of the quadrotor MAV to generate feasible reference attitude and thrust control commands for the attitude controller [98]. The trajectory controller runs at 60Hz in ROS and transmits the control commands to the quadrotor via XBee modules. The feedback for the trajectory controller and the ground truth of the experiment are captured using an Optitrack motion capture system. Fig. 3.13 shows the experimental setup.

Range measurements for the experiment are obtained using DWM1001 transceivers from decaWave. DWM1001 module compromises of DW1000 UWB range sensor and a system on chip (SoC), which includes an embedded UWB-based Real-Time Location System (RLTS). In a network of DWM1001 modules, the range is measured between a *Tag* and an *Anchor*. There can be several anchors and at least one Tag in the network to obtain the range measurements. In the current configuration, three DWM1001 modules are configured as *Anchors* and placed at the following locations.

- **Anchor 1** : $[-1.592\ -1.480\ 0.104]$ m
- **Anchor 2** : $[\ 2.130\ -0.828\ 0.057]$ m
- **Anchor 3** : $[\ 1.379\ \ 1.293\ 0.053]$ m

Another DWM1001 module is configured as a *Tag*, and it is mounted on the quadrotor. *Tag* measures the distance to the three anchors and provides range measurements at a rate of 10Hz. The quadrotor is flown on a circular trajectory with 1 m radius at a constant height of 1 m, and flight data are recorded.

The proposed estimator is executed offline using the recorded data from the quadrotor and the range sensors. The initialization of the estimator is done using groundtruth data obtained from the Optitrack motion captures system. The experimental results focus on validating the observable behavior of the estimator when the MAV is flying in an observable trajectory. Fig. 3.14 shows the position error for the case with three range measurements (*Case 1*). It can be seen that the estimation error is well within the 3σ boundary. The 3σ boundary is calculated using the covariance matrix generated by the error-state Kalman filter implementation (See Section 4.1.2). The total RMS error for the *Case 1* is 0.3248 m.

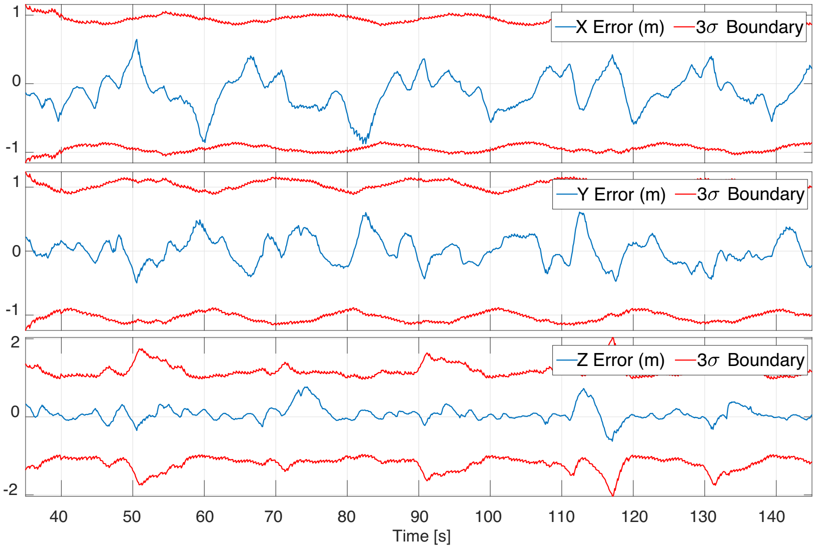

Fig. 3.14: Circular trajectory position estimation error with three range measurements.

For the case with two range measurements, I use the range measurements to Anchor 1 and Anchor 2. Fig. 3.15 shows the position error and the 3σ error boundary. The error is slightly larger than the case with three range measurements, but the error is well within the boundary. The total RMS error for *Case 2* is 0.8858 m. One of the main reasons for higher RMSE is the accuracy of the DWM1001 range measurements. DWM range measurements have an accuracy of around 10 cm. Additionally, the noise of the range measurements from DWM1001 module changes depending on the relative orientation of the two modules.

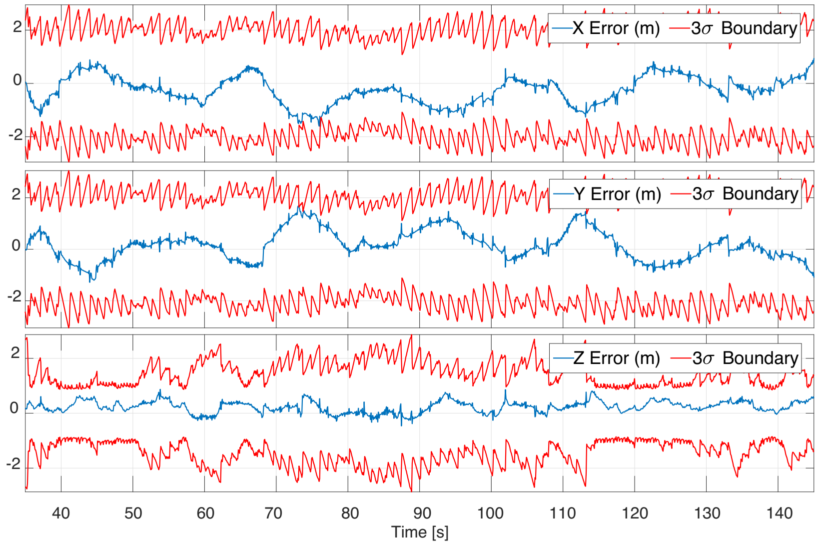

Fig. 3.15: Circular trajectory position estimation error with two range measurements.

There are a few challenges to mimicking the identified unobservable scenarios while performing experiments. One such challenge is the capture volume of the motion capture system. The capture volume is not large enough to sustain some unobservable conditions for a sufficient period of time. Therefore the results of the unobservable scenarios are limited to simulation results.

3.6 Summary

This chapter presented the design of a RINS that estimate the 3D pose of the MAV with three or two range measurements. The unique aerodynamic drag force effects were introduced into the system model, and this enabled the RINS to operate without a velocity sensor. An observability analysis was carried out to determine the observability of the RINS, and six unobservable trajectories and the corresponding unobservable directions were identified. The numerical simulations validated the unobservable directions identified in the observability analysis, and the experimental results showed that the proposed RINS is able to estimate the pose of the MAV when it is flying in an observable trajectory. The unobservable directions identified in this chapter is used in Chapter 4 to study the consistency of the proposed RINS.

Chapter 4

Observability Constrained Three and Two Range assisted Inertial Navigation System

In the previous chapter, the observability analysis of the three and two range assisted INS identified the unobservable trajectories and the corresponding unobservable modes of the proposed RINS. When the MAV is flying along an unobservable trajectory, the linearized estimator, the error-state Kalman filter (EKF) can suffer from inconsistencies, and the estimator gain spurious information along the unobservable directions. This chapter analyzes the ideal linearized estimator along unobservable trajectories to identify the cause of inconsistency and determine the consistency rules for the observability constrained RINS.

4.1 Error-state Kalman Filter Implementation

4.1.1 Continuous Time Model

The EKF implementation of the RINS is formulated using the nonlinear error definitions of the states of the system. Applying the expectation operator $\hat{(\cdot)}$ on both sides of (3.44), the state estimate propagation model can be expressed as

$$\begin{bmatrix} {}^W\dot{\hat{\boldsymbol{p}}}_B \\ {}^W\dot{\hat{\boldsymbol{v}}} \\ {}^W\dot{\hat{\boldsymbol{q}}}_B \\ {}^W\dot{\hat{\boldsymbol{b}}}_{\boldsymbol{g}} \\ {}^W\dot{\hat{\boldsymbol{b}}}_{\boldsymbol{a}} \end{bmatrix} = \begin{bmatrix} {}^W\hat{\boldsymbol{C}}_B\, {}^B\hat{\boldsymbol{v}} \\ \lfloor {}^B\hat{\boldsymbol{v}} \rfloor_\times ({}^B\hat{\boldsymbol{\omega}}) - \boldsymbol{K_d}\, {}^B\hat{\boldsymbol{v}} + \hat{b}_{az}\hat{\boldsymbol{e}}_{\boldsymbol{3}} - {}^W\hat{\boldsymbol{C}}_B^T \boldsymbol{g} \\ \frac{1}{2}\boldsymbol{\Xi}({}^W\hat{\boldsymbol{q}}_B)\begin{bmatrix} 0 & {}^B\hat{\boldsymbol{\omega}}^T \end{bmatrix}^T \\ \mathbf{0}_{3\times1} \\ \mathbf{0}_{3\times1} \end{bmatrix} \tag{4.1}$$

where ${}^W\hat{\boldsymbol{C}}_B = \boldsymbol{C}({}^W\hat{\boldsymbol{q}}_B)$, and ${}^B\hat{\boldsymbol{\omega}} = {}^B\boldsymbol{\omega}_m - \hat{\boldsymbol{b}}_{\boldsymbol{g}}$.

The error-state vector $\boldsymbol{\delta}\mathbf{x}$ is defined as

$$\boldsymbol{\delta}\mathbf{x} = \begin{bmatrix} \boldsymbol{\delta p}^T & \boldsymbol{\delta v}_{\boldsymbol{b}}^T & \boldsymbol{\delta\theta}^T & \boldsymbol{\delta b}_{\boldsymbol{g}}^T & \boldsymbol{\delta b}_{\boldsymbol{a}}^T \end{bmatrix}^T, \tag{4.2}$$

where $\boldsymbol{\delta p}, \boldsymbol{\delta v_b}, \boldsymbol{\delta b_g}, \boldsymbol{\delta b_a}$ are the position error, body frame velocity error, gryroscope bias error, and accelerometer bias error respectively.

The states of the RINS can be defined using the estimated states ($\hat{\mathbf{x}}$) and the error-states ($\boldsymbol{\delta}\mathbf{x}$) as, $\boldsymbol{\delta}\mathbf{x} = \mathbf{x} \ominus \hat{\mathbf{x}}$. The operator $\ominus$ is the same as the standard subtraction for all the states except for quaternion. For the quaternion, the multiplicative error model has been used [99]. The error between the quaternion ${}^W\boldsymbol{q}_B$ and its estimate

${}^{W}\hat{\boldsymbol{q}}_{B}$ is denoted by the angle-error vector $\boldsymbol{\delta\theta}$ as

$$\boldsymbol{\delta q} = \hat{\boldsymbol{q}}^{-1} \otimes \boldsymbol{q} \simeq \begin{bmatrix} 1 & \frac{1}{2}\boldsymbol{\delta\theta}^{T} \end{bmatrix}. \tag{4.3}$$

The rotation matrix, ${}^{W}\boldsymbol{C}_{B}$ can be expressed using the estimated rotation matrix and the angle error as

$${}^{W}\boldsymbol{C}_{B} = {}^{W}\hat{\boldsymbol{C}}_{B}\boldsymbol{\delta C}, \quad \boldsymbol{\delta C} = \exp(\lfloor \boldsymbol{\delta\theta} \rfloor_{\times}) \tag{4.4}$$

The system is linearized about the current state estimate, and the linearized error-states' dynamics can be expressed as

$$\dot{\boldsymbol{\delta p}} = {}^{W}\hat{\boldsymbol{C}}_{B}\boldsymbol{\delta v_{b}} - {}^{W}\hat{\boldsymbol{C}}_{B}\left\lfloor {}^{B}\hat{\boldsymbol{v}} \right\rfloor_{\times} \boldsymbol{\delta\theta} \tag{4.5}$$

$$\begin{aligned} \dot{\boldsymbol{\delta v_{b}}} = &- \left\lfloor ({}^{B}\boldsymbol{\omega}_{m} - \hat{\boldsymbol{b}}_{g}) \right\rfloor_{\times} \boldsymbol{\delta v_{b}} - \boldsymbol{K}_{d}\boldsymbol{\delta v_{b}} - \left\lfloor {}^{W}\hat{\boldsymbol{C}}_{B}^{T}\boldsymbol{g} \right\rfloor_{\times} \boldsymbol{\delta\theta} - \\ &\left\lfloor {}^{B}\hat{\boldsymbol{v}} \right\rfloor_{\times} \boldsymbol{\delta b_{g}} + \boldsymbol{I}_{33}\boldsymbol{\delta b_{a}} - \left\lfloor {}^{B}\hat{\boldsymbol{v}} \right\rfloor_{\times} \boldsymbol{\eta_{\omega}} \end{aligned} \tag{4.6}$$

$$\dot{\boldsymbol{\delta\theta}} = - \left\lfloor ({}^{B}\boldsymbol{\omega}_{m} - \hat{\boldsymbol{b}}_{g}) \right\rfloor_{\times} \boldsymbol{\delta\theta} - \boldsymbol{\delta b_{g}} - \boldsymbol{\eta_{\omega}} \tag{4.7}$$

$$\dot{\boldsymbol{\delta b_{g}}} = \boldsymbol{\eta_{gb}} \tag{4.8}$$

$$\dot{\boldsymbol{\delta b_{a}}} = \boldsymbol{\eta_{ab}}, \tag{4.9}$$

where $\boldsymbol{I}_{33} = [\mathbf{0}_{3\times1}\ \mathbf{0}_{3\times1}\ \grave{\boldsymbol{e}}_{3}]$. The linearized error-state dynamics given in (4.5), can be rewritten using the continuous time state transition matrix, $\mathbf{F_{c}}$ and continuous time input noise matrix, $\mathbf{G_{c}}$ as

$$\dot{\boldsymbol{\delta}\mathbf{x}} = \mathbf{F_{c}}\boldsymbol{\delta}\mathbf{x} + \mathbf{G_{c}}\boldsymbol{\eta}, \tag{4.10}$$

where

$$\mathbf{F_c} = \begin{bmatrix} \mathbf{0}_{3\times3} & {}^{W}\hat{\boldsymbol{C}}_{B} & -{}^{W}\hat{\boldsymbol{C}}_{B} \left\lfloor {}^{B}\hat{\boldsymbol{v}} \right\rfloor_{\times} & \mathbf{0}_{3\times3} & \mathbf{0}_{3\times3} \\ \mathbf{0}_{3\times3} & -\left\lfloor ({}^{B}\boldsymbol{\omega}_{m} - \hat{\boldsymbol{b}}_{\boldsymbol{g}}) \right\rfloor_{\times} - \boldsymbol{K_d} & -\left\lfloor {}^{W}\hat{\boldsymbol{C}}_{B}^{T} \boldsymbol{g} \right\rfloor_{\times} & \left\lfloor {}^{B}\hat{\boldsymbol{v}} \right\rfloor_{\times} & \boldsymbol{I}_{33} \\ \mathbf{0}_{3\times3} & \mathbf{0}_{3\times3} & -\left\lfloor ({}^{B}\boldsymbol{\omega}_{m} - \hat{\boldsymbol{b}}_{\boldsymbol{g}}) \right\rfloor_{\times} & -\boldsymbol{I_3} & \mathbf{0}_{3\times3} \\ \mathbf{0}_{3\times3} & \mathbf{0}_{3\times3} & \mathbf{0}_{3\times3} & \mathbf{0}_{3\times3} & \mathbf{0}_{3\times3} \\ \mathbf{0}_{3\times3} & \mathbf{0}_{3\times3} & \mathbf{0}_{3\times3} & \mathbf{0}_{3\times3} & \mathbf{0}_{3\times3} \end{bmatrix}, \tag{4.11}$$

$$\mathbf{G_c} = \begin{bmatrix} \mathbf{0}_{3\times3} & \mathbf{0}_{3\times3} & \mathbf{0}_{3\times3} \\ -\left\lfloor {}^{B}\hat{\boldsymbol{v}} \right\rfloor_{\times} & \mathbf{0}_{3\times3} & \mathbf{0}_{3\times3} \\ -\boldsymbol{I_3} & \mathbf{0}_{3\times3} & \mathbf{0}_{3\times3} \\ \mathbf{0}_{3\times3} & \boldsymbol{I_3} & \mathbf{0}_{3\times3} \\ \mathbf{0}_{3\times3} & \mathbf{0}_{3\times3} & \boldsymbol{I_3} \end{bmatrix}, \tag{4.12}$$

$$\boldsymbol{\eta} = \begin{bmatrix} \boldsymbol{\eta}_{\boldsymbol{\omega}}^{T} & \boldsymbol{\eta}_{\boldsymbol{gb}}^{T} & \boldsymbol{\eta}_{\boldsymbol{ga}}^{T} \end{bmatrix}^{T}. \tag{4.13}$$

4.1.2 Discrete-time Implementation

4.1.2.1 State Propagation

The IMU measurements are sampled at interval of δt, where $\delta t \triangleq t_{k+1} - t_k$. 4th order Runge-Kutta numerical integration is used to propagate the estimated states after each gyroscope measurement based on the process model given in (4.1). The covariance propagation is carried out by the discrete-time transition matrix $\boldsymbol{\Phi}_k$ defined as

$$\boldsymbol{\Phi}_k = \boldsymbol{\Phi}(t_{k+1}, t_k) = \exp\left(\int_{t_k}^{t_{k+1}} \mathbf{F_c}(\tau)\mathrm{d}\tau\right). \tag{4.14}$$

The discrete-time system noise covariance matrix $\boldsymbol{Q}_d$ is calculated as

$$\mathbf{Q}_{d,k} = \int_{t_k}^{t_{k+1}} \boldsymbol{\Phi}(t_{k+1}, \tau)\mathbf{G_c}\mathbf{Q}_c{\mathbf{G_c}}^T\boldsymbol{\Phi}(t_{k+1}, \tau)^T\mathrm{d}\tau, \tag{4.15}$$

where

$$\mathbf{Q}_c = \mathrm{diag}((\delta t^2\boldsymbol{\sigma}_{\boldsymbol{\omega}}^2)^T, (\delta t^2\boldsymbol{\sigma}_{\boldsymbol{gb}}^2)^T, (\delta t^2\boldsymbol{\sigma}_{\boldsymbol{ab}}^2)^T) \tag{4.16}$$

The propagated covariance matrix is calculated as

$$\mathbf{P}_{k+1|k} = \boldsymbol{\Phi}_k\mathbf{P}_{k|k}\boldsymbol{\Phi}_k^T + \mathbf{Q}_{d,k}. \tag{4.17}$$

4.1.2.2 Measurement update

Measurements for the filter are obtained using accelerometer and range sensors. The linearized error model of the measurements given in (3.45) can be expressed as

$$\boldsymbol{\delta y} = \boldsymbol{y_m} - \hat{\boldsymbol{y}} = \mathbf{H}\boldsymbol{\delta}\mathbf{x} + \boldsymbol{\nu}, \tag{4.18}$$

where $\hat{\boldsymbol{y}} = \mathbf{h}(\hat{\mathbf{x}})$ is the expected measurements computed by evaluating (3.45) with current state estimate. The measurement Jacobian w.r.t to the error states is expressed as

$$\mathbf{H} = \begin{bmatrix} {\mathbf{H_a}}^T & {\mathbf{H_r}}^T \end{bmatrix}^T, \tag{4.19}$$

where

$$\mathbf{H_a} = \begin{bmatrix} \mathbf{0}_{3\times3} & -\boldsymbol{K_d} & \mathbf{0}_{3\times3} & \mathbf{0}_{3\times3} & \boldsymbol{I_3} \end{bmatrix} \tag{4.20}$$

$$\mathbf{H_r} = \begin{bmatrix} \frac{{}^W\boldsymbol{r}_1^T}{r_1} & \mathbf{0}_{1\times3} & \mathbf{0}_{1\times3} & \mathbf{0}_{1\times3} & \mathbf{0}_{1\times3} \\ & & \vdots & & \\ \frac{{}^W\boldsymbol{r}_j^T}{r_j} & \mathbf{0}_{1\times3} & \mathbf{0}_{1\times3} & \mathbf{0}_{1\times3} & \mathbf{0}_{1\times3} \end{bmatrix}. \tag{4.21}$$

The Kalman gain for the filter correction is calculated as

$$\mathbf{K}_k = \mathbf{P}_{k+1|k}\mathbf{H}\left(\mathbf{H}\mathbf{P}_{k+1|k}\mathbf{H}^T + \mathbf{R}\right)^{-1} \tag{4.22}$$

where $\mathbf{R}$ is the covariance of $\boldsymbol{\nu}$. Employing the Kalman gain and the residual, the error state and covariance updates are calculated as

$$\boldsymbol{\delta}\mathbf{x} \leftarrow \mathbf{K}_k\left(\boldsymbol{y_m} - \hat{\boldsymbol{y}}\right) \tag{4.23}$$

$$\mathbf{P}_{k+1|k+1} \leftarrow \mathbf{P}_{k+1|k} - \mathbf{K}_k\left(\mathbf{H}\mathbf{P}_{k+1|k}\mathbf{H}^T + \mathbf{R}\right)\mathbf{K}_k^T \tag{4.24}$$

4.2 Verification of Unobservable Modes

A primary cause of estimator inconsistency is the mismatch between the unobservable modes of the linearized system and the unobservable modes of the nonlinear system. Hence accurately identifying the unobservable modes of a system can facilitate improvements in the consistency of the estimator.

The observability analysis carried out in Section 3.3 utilized the observability rank condition proposed in [81] to identify the unobservable trajectories and the corresponding unobservable modes. The rank of the observability matrix provides the sufficient conditions to determine the local weakly observability of the system. The nonlinear observability matrix is calculated using Lie derivatives of the output function. The first order Lie derivative of the output function captures the sensitivity of the system output along the states of the system. The nonlinear observability matrix constructed using the first and higher-order Lie derivatives captures the output's and its time derivatives' sensitivity along the states. The sensitivity of the output and its derivatives along the state space is only first order and does not capture any higher-order dynamics in the state space [100]. Therefore, the unobservable modes identified through the rank condition might not hold under certain conditions.

Wu et. al. have defined the unobservability of a nonlinear system based on unobservable transformations [89]. Internal states of an unobservable system cannot be inferred using the outputs of the system. This implies that there can be multiple states which produce the same output. Therefore, an unobservable system is always accompanied by at least one unobservable transformation, which is a relationship between the states that produce the same output. So the output of a system being invariant to a transformation is a description of unobservability.

Definition 4.1. *A transformation $\mathcal{T}$ is an unobservable transformation if the the system outputs and their derivatives are invariant under $\mathcal{T}$.*

The transformation $\mathcal{T}$ is an unobservable transformation if for arbitrary time t, $\mathbf{h}^{(j)}(\mathbf{x}) = \mathbf{h}^{(j)}(\mathbf{x^*})$, where $\mathbf{h}^{(j)}$ the j^{th} derivative with respect to time[1]. $\mathbf{x}$ and $\mathbf{x}^*$ denote the two states of the system defined as $\mathbf{x}^* = \mathcal{T}(\mathbf{x})$ [89].

4.2.1 Unobservable Scenarios of *Case 1*

4.2.1.1 Scenario 1: MAV is stationary with three range anchors

Unobservable transformations are defined based on the null vector spanning the unobservable subspace. The transformations are defined such that the transformed states are in the unobservable directions.

---

[1] Through out the thesis $(\cdot)^{(j)}$ represents the j^{th} time derivative of $(\cdot)$, $j \in [0, \mathbb{Z}^+]$.

The transformations correspond to the null vectors in (3.61) can be defined as

$$\mathcal{T}_{S1} = [\ \mathcal{T}_{S1_1}(\mathbf{x}) \quad \mathcal{T}_{S1_2}(\mathbf{x})\ ] = \begin{bmatrix} {}^{W}\boldsymbol{p}_{B} & {}^{W}\boldsymbol{p}_{B} \\ {}^{B}\boldsymbol{C}_{B'}^{T}\,{}^{B}\boldsymbol{v} & {}^{B}\boldsymbol{v} \\ {}^{W}\boldsymbol{q}_{B} \otimes {}^{B}\boldsymbol{q}_{B'} & {}^{W}\boldsymbol{q}_{B} \\ {}^{B}\boldsymbol{b}_{g} & {}^{B}\boldsymbol{b}_{g} + \theta_2 \grave{\boldsymbol{e}}_3 \\ {}^{B}\boldsymbol{b}_{a} & {}^{B}\boldsymbol{b}_{a} \end{bmatrix}, \tag{4.25}$$

where

$${}^{B}\boldsymbol{C}_{B'} = \exp\left(\left\lfloor {}^{W}\boldsymbol{C}_{B}^{T}\boldsymbol{g}\theta_1 \right\rfloor_{\times} \right), \tag{4.26}$$

$${}^{B}\boldsymbol{q}_{B'} = \begin{bmatrix} \cos\frac{\phi}{2} \\ \hat{\boldsymbol{u}}\sin\frac{\phi}{2} \end{bmatrix};\ \phi = \|{}^{W}\boldsymbol{C}_{B}^{T}\boldsymbol{g}\theta_1\|, \hat{\boldsymbol{u}} = \frac{{}^{W}\boldsymbol{C}_{B}^{T}\boldsymbol{g}\theta_1}{\phi}, \tag{4.27}$$

$\mathcal{T}_{S1_1}$ represents the transformation for the rotation of the MAV about the gravity vector, and $\mathcal{T}_{S1_2}$ represents the transformation for the gyroscope bias along the z axis of $\{B\}$.

Lemma 4.1. *When the MAV is stationary, the outputs of the RINS with three range measurements are invariant under the transformation* $\mathcal{T}_{S1}$

Proof. When the MAV is stationary, ${}^{B}\boldsymbol{\omega}_m - {}^{B}\boldsymbol{b}_g = \mathbf{0}_{3\times1}$, ${}^{W}\boldsymbol{p}_{B}^{(n)}, {}^{W}\boldsymbol{C}_{B}^{(n)}, \boldsymbol{\omega}^{(n)} = \mathbf{0}_{3\times1}$, ${}^{B}\boldsymbol{v}, {}^{B}\boldsymbol{v}^{(n)} = \mathbf{0}_{3\times1}$ and $b_{az}\grave{\boldsymbol{e}}_{\mathbf{3}} = {}^{W}\boldsymbol{C}_{B}^{T}\boldsymbol{g}$. Using the output function and the derivatives given in (B.2) to (B.6), it is straightforward to show that

$$\begin{aligned} &\mathbf{h}_a(\mathbf{x}) = \mathbf{h}_a(\mathcal{T}_{S1_1}(\mathbf{x})) = {}^{B}\boldsymbol{b}_a, \quad \mathbf{h}_a^{(n)}(\mathbf{x}) = \mathbf{h}_a^{(n)}(\mathcal{T}_{S1_1}(\mathbf{x})) = \mathbf{0}_{3\times3} \\ &\mathbf{h}_j(\mathbf{x}) = \mathbf{h}_j(\mathcal{T}_{S1_1}(\mathbf{x})) = \frac{1}{2}{}^{W}\boldsymbol{r}_j^{T}\,{}^{W}\boldsymbol{r}_j \quad \mathbf{h}_j^{(n)}(\mathbf{x}) = \mathbf{h}_j^{(n)}(\mathcal{T}_{S1_1}(\mathbf{x})) = 0. \end{aligned}$$

Hence, the output and its derivatives are invariant to the transformation $\mathcal{T}_{S1_1}$.

All the gyroscope bias terms of $\mathbf{h}_a^{(n)}(\mathbf{x})$ are multiplied with ${}^{B}\boldsymbol{v}$, and its derivatives. Since ${}^{B}\boldsymbol{v}^{(n)} = \mathbf{0}_{3\times1}$, $\mathbf{h}_a^{(n)}(\mathbf{x})$ is invariant under $\mathcal{T}_{S1_2}$. $\mathbf{h}_j^{(n)}(\mathbf{x})$ is a function of ${}^{W}\boldsymbol{r}_j$ and derivatives of ${}^{W}\boldsymbol{r}_j$, and therefore $\mathbf{h}_j^{(n)}(\mathbf{x})$ is also invariant under $\mathcal{T}_{S1_2}$. Hence the output and its derivatives are invariant under $\mathcal{T}_{S1_2}$. □

By the **Definition 1**, the unobservable modes identified through the observability analysis for **Scenario 1** are truly unobservable.

4.2.1.2 Scenario 2: MAV is flying on the plane of the three range anchors

The observability analysis showed that the position perpendicular to the plane of the three anchors is the unobservable direction under **Scenario 2**. Hence a transformation corresponding to the unobservable direction can be defined as

$$\mathcal{T}_{S2}(\mathbf{x}) = \begin{bmatrix} ({}^{W}\boldsymbol{p}_B + \theta\boldsymbol{n}_l)^T & {}^{B}\boldsymbol{v}^T & {}^{W}\boldsymbol{q}_B^T & {}^{B}\boldsymbol{b}_g^T & {}^{B}\boldsymbol{b}_a^T \end{bmatrix}^T, \tag{4.28}$$

where $\theta \in \mathbb{R},\ \theta \neq 0$, $\boldsymbol{n}_l = \boldsymbol{l}_{12} \times \boldsymbol{l}_{13}$, $\boldsymbol{l}_{12} = {}^{W}\boldsymbol{r}_2 - {}^{W}\boldsymbol{r}_1$, and $\boldsymbol{l}_{13} = {}^{W}\boldsymbol{r}_3 - {}^{W}\boldsymbol{r}_1$.

Lemma 4.2. *When the MAV is flying on the plane of the three anchors, the outputs of RINS are variant under transformation $\mathcal{T}_{S2}$.*

Proof. Consider the output function $\mathbf{h}_j(\mathbf{x})$. By substituting $\mathcal{T}_{S2}(\mathbf{x})$ we get

$$\begin{aligned} \mathbf{h}_j(\mathcal{T}_{S2}(\mathbf{x})) &= \frac{1}{2}\left({}^{W}\boldsymbol{p}_B + \theta\boldsymbol{n}_l - {}^{W}\boldsymbol{p}_j\right)^T\left({}^{W}\boldsymbol{p}_B + \theta\boldsymbol{n}_l - {}^{W}\boldsymbol{p}_j\right) \\ &= \theta^2\boldsymbol{n}_l^T\boldsymbol{n}_l + \mathbf{h}_j(\mathbf{x}) \end{aligned} \tag{4.29}$$

(4.29) shows that, $\mathbf{h}_j(\mathcal{T}_{S2}(\mathbf{x})) \neq \mathbf{h}_j(\mathbf{x}), \forall\theta \neq 0$. Therefore the outputs of the RINS is variant under the transformation $\mathcal{T}_{S2}$. □

Lemma 4.2 shows that the unobservable direction identified through the observability analysis for **Scenario 2**, is not a true unobservable direction.

4.2.1.3 Scenario 3: MAV is flying parallel to the gravity with three range anchors

The observability analysis provides two unobservable modes for **Scenario 3**, rotation about the gravity vector and gyroscope bias along ${}^{B}\boldsymbol{v}$ direction. Similar to (4.25), the unobservable transformations correspond to unobservable modes can be defined as

$$\mathcal{T}_{S3} = [\ \mathcal{T}_{S3_1}(\mathbf{x}) \quad \mathcal{T}_{S3_2}(\mathbf{x})\ ] = \begin{bmatrix} {}^{W}\boldsymbol{p}_{B} & {}^{W}\boldsymbol{p}_{B} \\ {}^{B}\boldsymbol{C}_{B'}^{T}\,{}^{B}\boldsymbol{v} & {}^{B}\boldsymbol{v} \\ {}^{W}\boldsymbol{q}_{B} \otimes {}^{B}\boldsymbol{q}_{B'} & {}^{W}\boldsymbol{q}_{B} \\ {}^{B}\boldsymbol{b}_{g} & {}^{B}\boldsymbol{b}_{g} + \theta_2\,{}^{B}\boldsymbol{v} \\ {}^{B}\boldsymbol{b}_{a} & {}^{B}\boldsymbol{b}_{a} \end{bmatrix}. \tag{4.30}$$

Lemma 4.3. *When the MAV is flying parallel to the gravity vector, the outputs of the RINS are invariant under transformation $\mathcal{T}_{S3}$.*

Proof. When the MAV is flying parallel to the gravity vector, the velocity and the acceleration of the MAV in $\{W\}$ can be expressed as ${}^{W}\boldsymbol{p}_{B}^{(1)} = \alpha\boldsymbol{g}$, and ${}^{W}\boldsymbol{p}_{B}^{(2)} = \beta\boldsymbol{g}$. Using (3.31) and (3.33), it is trivial to show that ${}^{B}\boldsymbol{v}$ is parallel to the z axis of $\{B\}$, and ${}^{B}\boldsymbol{v} = \alpha\,{}^{W}\boldsymbol{C}_{B}^{T}\boldsymbol{g}$. Since any vector rotated about itself results in the same vector, applying the transformation $\mathcal{T}_{S3_1}$ to (B.2) results in

$$\mathbf{h}_a(\mathcal{T}_{S3_1}(\mathbf{x})) = -\boldsymbol{K_d}\,{}^{B}\boldsymbol{C}_{B'}^{T}\,{}^{B}\boldsymbol{v} + {}^{B}\boldsymbol{b}_{a} = -\boldsymbol{K_d}\,{}^{B}\boldsymbol{v} + {}^{B}\boldsymbol{b}_{a} = \mathbf{h}_a(\mathbf{x}) \tag{4.31}$$

$\boldsymbol{C}({}^{W}\boldsymbol{q}_{B} \otimes {}^{B}\boldsymbol{q}_{B'}) = {}^{W}\boldsymbol{C}_{B'} = {}^{W}\boldsymbol{C}_{B}\,{}^{B}\boldsymbol{C}_{B'}$, and from (4.26) it can be shown that

${}^{W}\boldsymbol{C}_{B'}^{T}\boldsymbol{g} = {}^{W}\boldsymbol{C}_{B}^{T}\boldsymbol{g}$. Furthermore, from (3.34) it can be shown that ${}^{B}\boldsymbol{\omega} \parallel {}^{B}\boldsymbol{v}$, i.e. ${}^{B}\boldsymbol{\omega}^{(n)} = [\ 0\ 0\ \omega_z^{(n)}\ ]^T$, and this results in $\lfloor {}^{B}\boldsymbol{v}^{(n)} \rfloor_\times {}^{B}\boldsymbol{\omega}_m^{(m)} = \mathbf{0}$ and $\left({}^{W}\boldsymbol{C}_{B}^{T}\right)^{(n)}\boldsymbol{g} = \mathbf{0}$. Using the aforementioned relations, it is trivial to show that

$$\begin{aligned}
\mathbf{h}_a^{(1)}(\mathbf{X}) &= \mathbf{h}_a^{(1)}(\mathcal{T}_{S3_1}(\mathbf{X})) = -\boldsymbol{K}_{\boldsymbol{d}}{}^{B}\boldsymbol{v} + b_{az}\grave{\boldsymbol{e}}_{\boldsymbol{3}} - {}^{W}\boldsymbol{C}_{B}\boldsymbol{g} \\
\mathbf{h}_a^{(n)}(\mathbf{X}) &= \mathbf{h}_a^{(n)}(\mathcal{T}_{S3_1}(\mathbf{X})) = (-1)^n\boldsymbol{K}_{\boldsymbol{d}}^{n}\left(-\boldsymbol{K}_{\boldsymbol{d}}{}^{B}\boldsymbol{v} + b_{az}\grave{\boldsymbol{e}}_{\boldsymbol{3}} - {}^{W}\boldsymbol{C}_{B}^{T}\boldsymbol{g}\right).
\end{aligned}$$

This shows that output function $\mathbf{h}_a(\mathbf{X})$ is invariant to $\mathcal{T}_{S3_1}(\mathbf{X})$. Since the position does not change under $\mathcal{T}_{S3_1}(\mathbf{X})$, the output function $\mathbf{h}_j(\mathbf{X})$ is invariant. Hence the output function is invariant to $\mathcal{T}_{S3_1}(\mathbf{X})$.

In (B.4), the gyroscope bias and its derivatives always appear as a cross product with ${}^{B}\boldsymbol{v}$ and its derivatives. It is straightforward to show that $\lfloor {}^{B}\boldsymbol{v} \rfloor_\times ({}^{B}\boldsymbol{\omega}_m - ({}^{B}\boldsymbol{b}_g + \theta_2{}^{B}\boldsymbol{v})) = \lfloor {}^{B}\boldsymbol{v} \rfloor_\times ({}^{B}\boldsymbol{\omega}_m - {}^{B}\boldsymbol{b}_g)$. Therefore $\mathbf{h}_a(\mathbf{x})$ and its derivatives are invariant under $\mathcal{T}_{S3_1}(\mathbf{X})$. $\mathbf{h}_j^{(n)}(\mathbf{x})$ is a function of ${}^{W}\boldsymbol{r}_j$ and derivatives of ${}^{W}\boldsymbol{r}_j$, and does not contain any ${}^{B}\boldsymbol{b}_g$ terms. Therefore $\mathbf{h}_j^{(n)}(\mathbf{x})$ is also invariant under $\mathcal{T}_{S3_2}$. Hence the output and its derivatives are invariant under $\mathcal{T}_{S3_2}$, $\square$

The unobservable modes identified for the **Scenario 3** are truly unobservable.

4.2.2 Unobservable Scenarios of *Case 2*

4.2.2.1 Scenario 4: MAV is stationary with two range anchors

This scenario has three unobservable modes, out of which two of them are similar to the unobservable mode of **Scenario 1**. The third unobservable mode is the perpendicular direction to the plane having the MAV and the two anchors. The corresponding transformations can be defined as

$$\mathcal{T}_{S4}(\mathbf{x}) = [\ \mathcal{T}_{S4_1}(\mathbf{x}) \quad \mathcal{T}_{S4_2}(\mathbf{x}) \quad \mathcal{T}_{S4_3}(\mathbf{x})\ ]$$

$$= \begin{bmatrix} {}^W\boldsymbol{p}_B & {}^W\boldsymbol{p}_B & \exp(\lfloor\theta_3\boldsymbol{l}_{12}\rfloor_\times){}^W\boldsymbol{r}_j + {}^W\boldsymbol{p}_j \\ {}^B\boldsymbol{C}_{B'}^T{}^B\boldsymbol{v} & {}^B\boldsymbol{v} & {}^B\boldsymbol{v} \\ {}^W\boldsymbol{q}_B \otimes {}^B\boldsymbol{q}_{B'} & {}^W\boldsymbol{q}_B & {}^W\boldsymbol{q}_B \\ {}^B\boldsymbol{b}_g & {}^B\boldsymbol{b}_g + \theta_2\grave{\boldsymbol{e}}_3 & {}^B\boldsymbol{b}_g \\ {}^B\boldsymbol{b}_a & {}^B\boldsymbol{b}_a & {}^B\boldsymbol{b}_a \end{bmatrix}, \tag{4.32}$$

where $\theta_3 \in \mathbb{R}$ and $\boldsymbol{l}_{12} = {}^W\boldsymbol{r}_1 - {}^W\boldsymbol{r}_2$.

Lemma 4.4. *When the MAV is stationary with two range anchors, the outputs of the RINS is invariant under the transformation $\mathcal{T}_{S4}(\mathbf{x})$.*

Proof. The transformations $\mathcal{T}_{S4_1}(\mathbf{x})$, and $\mathcal{T}_{S4_2}(\mathbf{x})$ are similar to the unobservable transformations of **Scenario 1**. Therefore the invariance of the outputs can be proven similar to Lemma 4.1.

The position state does not appear in $\mathbf{h}_a(\mathbf{x})$. Therefore, $\mathcal{T}_{S4_3}(\mathbf{X})$ does not affect $h_a(\mathbf{x})$ and it's derivatives. Once $\mathcal{T}_{S4_3}(\mathbf{X})$ applied to the range vector,

$$\boldsymbol{r}_j^* = \exp(\lfloor\theta_3\boldsymbol{l}_{12}\rfloor_\times){}^W\boldsymbol{r}_j + {}^W\boldsymbol{p}_j - {}^W\boldsymbol{p}_j = \exp\left(\lfloor\theta_3\boldsymbol{l}_{12}\rfloor_\times\right){}^W\boldsymbol{r}_j. \tag{4.33}$$

(4.33) represents the rotation of the range vector ${}^W\boldsymbol{r}_j$ about $\boldsymbol{l}_{12}$. Therefore, $\boldsymbol{r}_i^*$, and ${}^W\boldsymbol{r}_j$ has the same magnitude, and $\mathbf{h}_j(\mathbf{x}) = \mathbf{h}_j(\mathcal{T}_{S4_3}(\mathbf{x}))$. Since the MAV is stationary, ${}^W\boldsymbol{p}_B^{(n)} = \mathbf{0}_{3\times1}$, and $\mathbf{h}_j^{(n)}(\mathcal{T}_{S1_1}(\mathbf{x})) = \mathbf{h}_j^{(n)}(\mathbf{x}) = 0$. Therefore $\mathbf{h}(\mathbf{x})$ is invariant to the transformation $\mathcal{T}_{S4_3}(\mathbf{x})$. □

The proof shows that the output function is invariant under the transformation

$\mathcal{T}_{S4}(\mathbf{x})$. Therefore, the unobservable modes of **Scenario 4** are truly unobservable.

4.2.2.2 Scenario 5: MAV is flying on the plane of the MAV and the two anchors

The only unobservable mode of this scenario is the perpendicular direction to the plane of the MAV and the two anchors. The corresponding transformation, $\mathcal{T}_{S5}(\mathbf{x})$ can be defined as as

$$\mathcal{T}_{S5}(\mathbf{x}) = \begin{bmatrix} \exp(\lfloor \theta_3 \boldsymbol{l}_{12} \rfloor_\times)^W\boldsymbol{r}_j + {}^W\boldsymbol{p}_j \\ {}^B\boldsymbol{v} \\ {}^W\boldsymbol{q}_B \\ {}^B\boldsymbol{b}_g \\ {}^B\boldsymbol{b}_a \end{bmatrix}, \tag{4.34}$$

Lemma 4.5. *When the MAV is flying on the plane created by the MAV and the two anchors, the output of the RINS is invariant under transformation* $\mathcal{T}_{S5}(\mathbf{x})$

Proof. The position state does not appear in $\mathbf{h}_a(\mathbf{x})$. Therefore, $\mathcal{T}_{S5}(\mathbf{X})$ does not affect $h_a(\mathbf{x})$ and it's derivatives. The $\boldsymbol{r}_j^*$ expressed in (4.33) holds true under $\mathcal{T}_{S5}(\mathbf{X})$, and the time derivative of $\boldsymbol{r}_j^*$ can be calculated as

$$\boldsymbol{r}_j^{*(n)} = \exp(\lfloor \theta_3 \boldsymbol{l}_{12} \rfloor_\times)^W\boldsymbol{r}_j^{(n)}. \tag{4.35}$$

With (4.35), it is trivial to show that $\mathbf{h}_j^{(n)}(\mathcal{T}_{S5}(\mathbf{x})) = \mathbf{h}_j^{(n)}(\mathbf{x}), \forall n \in \mathbb{Z}^+$. Hence the $\mathbf{h}(\mathbf{x})$ is invariant under transformation $\mathcal{T}_{S5}$ □

This proof shows that the perpendicular direction to the plane created by the

MAV and the two range anchors is a true unobservable mode, under **Scenario 5**.

4.2.2.3 Scenario 6: MAV is flying parallel to the gravity with two range anchors

Null space of this scenario is spanned by the same two vectors as in **Scenario 3**, and the transformations corresponding to the unobservable directions, $\mathcal{T}_{S6}(\mathbf{x})$ are similar to the transformations defined in (4.30)

Lemma 4.6. *When the MAV is flying parallel to the gravity vector, the outputs of the RINS with two range measurements are invariant under transformation* $\mathcal{T}_{S6}(\mathbf{x})$

Proof. The proof is similar to that of Lemma 4.3. ☐

4.3 Consistency Analysis

A key contributor to inconsistency in filter implementation is the mismatch between the unobservable properties of the true nonlinear system and the one employed by the estimator. This section examines the observability properties of the linearized RINS model. First, the unobservable directions of the ideal linearized RINS (i.e. Jacobians evaluated at the true states) are determined and show that they match the unobservable directions of the nonlinear system. Then the unobservable directions of the linearized RINS (i.e. Jacobians evaluated at the estimated states) are calculated and show that they differ from the ideal linearized RINS.

4.3.1 Observability analysis of *Ideal* Linearized RINS

The observability matrix (also known as observability Gramian) $\mathbf{M}$ is defined as a function of the linearized measurement model $\mathbf{H}$, and the discrete time transition matrix $\mathbf{\Phi}$. $\mathbf{M}$ and $\mathbf{\Phi}$ are functions of $\mathbf{x}^*$, and can be expressed as

$$\mathbf{M}(\mathbf{x}^*) = \begin{bmatrix} \mathbf{H}_1 \\ \\ \mathbf{H}_1\mathbf{\Phi}_{2,1} \\ \vdots \\ \\ \mathbf{H}_k\mathbf{\Phi}_{k,1} \end{bmatrix}, \tag{4.36}$$

where $\mathbf{\Phi}_{k,1}$ is the state transition matrix from time-step 1 to k, and $\mathbf{H}_k$ is the Jacobian of the measurement model given in (4.19), at time step k.

4.3.1.1 Structure of $\Phi(t_k, t_1)$

The discrete state transition matrix $\mathbf{\Phi}^{(}t_k, t_1)$ satisfies the following differential equations,

$$\dot{\mathbf{\Phi}}(t_k, t_1) = \mathbf{F_c}\mathbf{\Phi}(t, t_0) \tag{4.37}$$

$$\mathbf{\Phi}(t_1, t_1) = \mathbf{I}_{15}. \tag{4.38}$$

The analytical expressions of the elements of $\mathbf{\Phi}(t, t_1)$ can be obtained by analyzing the block elements of (4.37). Following the process provided in [23], elements of $\mathbf{\Phi}(t, t_1)$

are determined as [2]

$$\mathbf{\Phi}(t_k, t_1) = \mathbf{\Phi}_{k,1} = \begin{bmatrix} \boldsymbol{I_3} & \mathbf{\Phi}^{(1,2)} & \mathbf{\Phi}^{(1,3)} & \mathbf{\Phi}^{(1,4)} & \mathbf{\Phi}^{(1,5)} \\ \mathbf{0}_{3\times3} & \mathbf{\Phi}^{(2,2)} & \mathbf{\Phi}^{(2,3)} & \mathbf{\Phi}^{(2,4)} & \mathbf{\Phi}^{(2,5)} \\ \mathbf{0}_{3\times3} & \mathbf{0}_{3\times3} & \mathbf{\Phi}^{(3,3)} & \mathbf{\Phi}^{(3,4)} & \mathbf{0}_{3\times3} \\ \mathbf{0}_{3\times3} & \mathbf{0}_{3\times3} & \mathbf{0}_{3\times3} & \boldsymbol{I_3} & \mathbf{0}_{3\times3} \\ \mathbf{0}_{3\times3} & \mathbf{0}_{3\times3} & \mathbf{0}_{3\times3} & \mathbf{0}_{3\times3} & \boldsymbol{I_3} \end{bmatrix}, \tag{4.39}$$

where

$$\mathbf{\Phi}_{k,1}^{(1,2)} = -{}^{W}\boldsymbol{C}_{B(t_1)} \exp\left(-\boldsymbol{K_d}(t_k - t_1)\right) \boldsymbol{K_d}^{-1} \tag{4.40}$$

$$\begin{aligned} \mathbf{\Phi}_{k,1}^{(1,3)} = &\int_{t_1}^{t_k} \left({}^{W}\boldsymbol{C}_{B(s)} \exp\left(-\boldsymbol{K_d}(s - t_1)\right) \int_{t_1}^{s} \left(\Lambda(\tau) \left\lfloor {}^{W}\boldsymbol{C}_{B(\tau)}^{T} \boldsymbol{g} \right\rfloor_{\times} {}^{B(\tau)}\boldsymbol{C}_{B(t_1)} \right) \mathrm{d}\tau \right) \mathrm{d}s \\ &+ \int_{t_1}^{t_k} \left({}^{W}\boldsymbol{C}_{B(s)} \left\lfloor {}^{B}\boldsymbol{v} \right\rfloor_{\times} {}^{B(s)}\boldsymbol{C}_{B(t_1)} \right) \mathrm{d}s \end{aligned} \tag{4.41}$$

$$\mathbf{\Phi}_{k,1}^{(1,4)} = \int_{t_1}^{t_k} {}^{W}\boldsymbol{C}_{B(s)} \mathbf{\Phi}_{k,1}^{(2,.4)} \mathrm{d}s - \int_{t_1}^{t_k} \left({}^{W}\boldsymbol{C}_{B(s)} \left\lfloor {}^{B}\boldsymbol{v} \right\rfloor_{\times} \int_{t_1}^{s} {}^{B(t_k)}\boldsymbol{C}_{B(\tau)} \mathrm{d}\tau \right) \mathrm{d}s \tag{4.42}$$

$$\mathbf{\Phi}_{k,1}^{(1,5)} = \int_{t_1}^{t_k} \left({}^{W}\boldsymbol{C}_{B(s)} \exp\left(-\boldsymbol{K_d}(s - t_1)\right) \int_{t_1}^{s} \left(\Lambda(\tau) \boldsymbol{I}_{33}\right) \right) \mathrm{d}\tau \mathrm{d}s \tag{4.43}$$

$$\mathbf{\Phi}_{k,1}^{(2,2)} = {}^{B(t_k)}\boldsymbol{C}_{B(t_1)} \exp\left(-\boldsymbol{K_d}(t - t_1)\right) \tag{4.44}$$

$$\mathbf{\Phi}_{k,1}^{(2,3)} = \exp\left(-\boldsymbol{K_d}(t_k - t_1)\right) \int_{t_1}^{t_k} \left(\Lambda(\tau) \left\lfloor {}^{W}\boldsymbol{C}_{B(\tau)}^{T} \boldsymbol{g} \right\rfloor_{\times} {}^{B(\tau)}\boldsymbol{C}_{B(t_1)} \right) \mathrm{d}\tau \tag{4.45}$$

$$\mathbf{\Phi}_{k,1}^{(2,4)} = \exp\left(-\boldsymbol{K_d}(t_k - t_1)\right) \int_{t_1}^{t_k} \left(\Lambda(s) \left(\left\lfloor {}^{W}\boldsymbol{C}_{B(s)}^{T} \boldsymbol{g} \right\rfloor_{\times} \int_{t_1}^{s} {}^{B(s)}\boldsymbol{C}_{B(\tau)} \mathrm{d}\tau - \left\lfloor {}^{B}\boldsymbol{v} \right\rfloor_{\times} \right) \right) \mathrm{d}s \tag{4.46}$$

$$\mathbf{\Phi}_{k,1}^{(2,5)} = \exp\left(-\boldsymbol{K_d}(t_k - t_1)\right) \int_{t_1}^{t_k} \left(\Lambda(\tau) \boldsymbol{I}_{33}\right) \mathrm{d}\tau \tag{4.47}$$

$$\mathbf{\Phi}_{k,1}^{(3,3)} = {}^{B(t_k)}\boldsymbol{C}_{B(t_1)} \tag{4.48}$$

$$\mathbf{\Phi}_{k,1}^{(3,4)} = -\int_{t_1}^{t_k} {}^{B(t_k)}\boldsymbol{C}_{B(\tau)} \mathrm{d}\tau \tag{4.49}$$

---

[2] In this calculation I omit the time parameters for clarity. $\mathbf{\Phi}^{(i,j)}$ refers to the block matrix on i^{th} row and j^{th} column.

$$\Lambda(\tau) = {}^{B(t)}\boldsymbol{C}_{B(\tau)} \exp\left(\boldsymbol{K_d}(\tau - t_1)\right) \tag{4.50}$$

Using the expressions calculated above, the k^{th} row of $\mathbf{M}$ for any $k > 1$ can be calculated as

$$\mathbf{M}_k = \mathbf{H}_k \boldsymbol{\Phi}_{k,1} = \begin{bmatrix} \mathbf{0}_{3\times3} & -\boldsymbol{K_d}\boldsymbol{\Phi}_{k,1}^{(2,2)} & -\boldsymbol{K_d}\boldsymbol{\Phi}_{k,1}^{(2,3)} & -\boldsymbol{K_d}\boldsymbol{\Phi}_{k,1}^{(2,4)} & -\boldsymbol{K_d}\boldsymbol{\Phi}_{k,1}^{(2,5)} + \boldsymbol{I}_{33} \\ \mathbf{R}_3 & \mathbf{R}_3\boldsymbol{\Phi}_{k,1}^{(1,2)} & \mathbf{R}_3\boldsymbol{\Phi}_{k,1}^{(1,3)} & \mathbf{R}_3\boldsymbol{\Phi}_{k,1}^{(1,4)} & \mathbf{R}_3\boldsymbol{\Phi}_{k,1}^{(1,5)} \end{bmatrix}, \tag{4.51}$$

where

$$\mathbf{R}_3 = \begin{bmatrix} \frac{{}^{W}\boldsymbol{r}_1}{r_1} & \frac{{}^{W}\boldsymbol{r}_2}{r_2} & \frac{{}^{W}\boldsymbol{r}_3}{r_3} \end{bmatrix}^T. \tag{4.52}$$

Lemma 4.7. *The right nullspace of the observability matrix* $\mathbf{M}(\mathbf{x})$ *of the linearized RINS under* ***Scenario 1*** *is spanned by*

$$^{1}\boldsymbol{\mathcal{N}} = \begin{bmatrix} \mathbf{0}_{3\times1} & \mathbf{0}_{3\times1} \\ \mathbf{0}_{3\times1} & \mathbf{0}_{3\times1} \\ {}^{W}\boldsymbol{C}_{B}^{T}\boldsymbol{g} & \mathbf{0}_{3\times1} \\ \mathbf{0}_{3\times1} & b_{az}\grave{\boldsymbol{e}}_{\boldsymbol{3}} \\ \mathbf{0}_{3\times1} & \mathbf{0}_{3\times1} \end{bmatrix}. \tag{4.53}$$

Proof. Multiplying each block row of $\mathbf{M}(\mathbf{x})$, with $^{1}\boldsymbol{\mathcal{N}}_{(:,1)}$, we get

$$\mathbf{M}_k{}^{1}\boldsymbol{\mathcal{N}}_{(:,1)} = \begin{bmatrix} -\boldsymbol{K_d}\boldsymbol{\Phi}_{k,1}^{(2,3)}{}^{W}\boldsymbol{C}_{B}^{T}\boldsymbol{g} \\ \mathbf{R}_3\boldsymbol{\Phi}_{k,1}^{(1,3)}{}^{W}\boldsymbol{C}_{B}^{T}\boldsymbol{g} \end{bmatrix} \tag{4.54}$$

$$\begin{aligned} -\boldsymbol{K_d}\boldsymbol{\Phi}_{k,1}^{(2,3)}\,{}^{W}\boldsymbol{C}_{B}^{T}\boldsymbol{g} &= -\boldsymbol{K_d}\int_{t_1}^{t_k}\left(\Lambda(\tau)\left\lfloor {}^{W}\boldsymbol{C}_{B(\tau)}^{T}\boldsymbol{g}\right\rfloor_{\times}{}^{B(\tau)}\boldsymbol{C}_{B(t_1)}\right)\mathrm{d}\tau\cdot{}^{W}\boldsymbol{C}_{B(t_1)}^{T}\boldsymbol{g} \\ &= -\boldsymbol{K_d}\int_{t_1}^{t_k}\left(\Lambda(\tau)\left\lfloor {}^{W}\boldsymbol{C}_{B(\tau)}^{T}\boldsymbol{g}\right\rfloor_{\times}{}^{W}\boldsymbol{C}_{B(\tau)}^{T}\boldsymbol{g}\right)\mathrm{d}\tau \\ &= \mathbf{0}_{3\times1} \end{aligned} \tag{4.55}$$

Since the MAV is stationary, ${}^{B}\boldsymbol{v} = \mathbf{0}_{3\times1}$,

$$\begin{aligned} &\mathbf{R}_3\boldsymbol{\Phi}_{k,1}^{(1,3)}\,{}^{W}\boldsymbol{C}_{B}^{T}\boldsymbol{g} \\ &= \mathbf{R}_3\int_{t_1}^{t_k}\left({}^{W}\boldsymbol{C}_{B(s)}\exp\left(-\boldsymbol{K_d}(s-t_1)\right)\int_{t_1}^{s}\left(\Lambda(\tau)\left\lfloor {}^{W}\boldsymbol{C}_{B(\tau)}^{T}\boldsymbol{g}\right\rfloor_{\times}{}^{B(\tau)}\boldsymbol{C}_{B(t_1)}\right)\mathrm{d}\tau\right)\mathrm{d}s\cdot{}^{W}\boldsymbol{C}_{B(t_1)}^{T}\boldsymbol{g} \\ &= \mathbf{R}_3\int_{t_1}^{t_k}\left({}^{W}\boldsymbol{C}_{B(s)}\exp\left(-\boldsymbol{K_d}(s-t_1)\right)\int_{t_1}^{s}\left(\Lambda(\tau)\left\lfloor {}^{W}\boldsymbol{C}_{B(\tau)}^{T}\boldsymbol{g}\right\rfloor_{\times}{}^{B(\tau)}\boldsymbol{C}_{B(t_1)}{}^{W}\boldsymbol{C}_{B(t_1)}^{T}\boldsymbol{g}\right)\mathrm{d}\tau\right)\mathrm{d}s \\ &= \mathbf{R}_3\int_{t_1}^{t_k}\left({}^{W}\boldsymbol{C}_{B(s)}\exp\left(-\boldsymbol{K_d}(s-t_1)\right)\int_{t_1}^{s}\left(\Lambda(\tau)\left\lfloor {}^{W}\boldsymbol{C}_{B(\tau)}^{T}\boldsymbol{g}\right\rfloor_{\times}{}^{W}\boldsymbol{C}_{B(\tau)}^{T}\boldsymbol{g}\right)\mathrm{d}\tau\right)\mathrm{d}s \\ &= \mathbf{0}_{3\times1} \end{aligned} \tag{4.56}$$

Similarly, it is trivial to prove that

$$\mathbf{M}_k{}^{1}\boldsymbol{\mathcal{N}}_{(:,2)} = \mathbf{0}_{6\times1} \tag{4.57}$$

Therefore, $\mathbf{M}_k{}^{1}\boldsymbol{\mathcal{N}} = \mathbf{0}_{6\times2}$, and ${}^{1}\boldsymbol{\mathcal{N}}$ spans the null space of $\mathbf{M}(\mathbf{x})$ under **Scenario 1**. □

Following similar steps, it is straightforward to show that the rest of the unobservable scenarios of the nonlinear system are unobservable in the ideal linearized RINS.

4.3.2 Observability analysis of Linearized RINS

The EKF implementation of the RINS employs a linearized system, and When the system is linearized about the estimated state $\hat{\mathbf{x}}$, $\mathbf{M}(\hat{\mathbf{x}})$ gains rank due to errors in the state estimates [23]. As the EKF is operating over time, evaluating the state transition matrix and the measurement Jacobian with the current estimated states changes the structure of (4.51) due to linearization errors. Therefore, the null spaces identified in Section 3.3, for each scenario, are not equal to the null spaces of $\mathbf{M}(\hat{\mathbf{x}})$. This can be verified by evaluating the rank of the observability matrix during simulations or experiments.

4.4 Consistency Improvement

This section focuses on improving the consistency of the EKF implementation of the RINS. The consistency can be improved by ensuring the linearized system and the nonlinear system both have the same number of unobservable directions with a similar structure. In other words, each block row of (4.36) should satisfy $\mathbf{H}_k \boldsymbol{\Phi}_{k,1} \boldsymbol{\mathcal{N}} = \mathbf{0}$. This condition can be enforced by satisfying the conditions given in (4.58), and (4.59) at each time step.

$$\boldsymbol{\mathcal{N}}_{k+1} = \boldsymbol{\Phi}_k \boldsymbol{\mathcal{N}}_k \tag{4.58}$$

$$\mathbf{H}_k \boldsymbol{\mathcal{N}}_k = \mathbf{0}, \tag{4.59}$$

where $\boldsymbol{\mathcal{N}}$ corresponds to the vectors that span the null space of the nonlinear system, $\mathbf{H}_k$ is the measurement Jacobian at time t_k, and $\boldsymbol{\Phi}_k$ is the state transition matrix defined in (4.39)

First, the null space of each scenario is evaluated with (4.58), and (4.59) to determine whether the null space violates both or a single condition. The null vectors of the **Scenario 1** at the time step k, and at $k+1$ can be expressed as

$$^{1}\boldsymbol{\mathcal{N}}_{k} = \begin{bmatrix} \mathbf{0}_{3\times1} & \mathbf{0}_{3\times1} \\ \mathbf{0}_{3\times1} & \mathbf{0}_{3\times1} \\ {}^{W}\boldsymbol{C}^{T}_{B(k)}\boldsymbol{g} & \mathbf{0}_{3\times1} \\ \mathbf{0}_{3\times1} & b_{az}\grave{\boldsymbol{e}}_{\mathbf{3}} \\ \mathbf{0}_{3\times1} & \mathbf{0}_{3\times1} \end{bmatrix} \qquad {}^{1}\boldsymbol{\mathcal{N}}_{k+1} = \begin{bmatrix} \mathbf{0}_{3\times1} & \mathbf{0}_{3\times1} \\ \mathbf{0}_{3\times1} & \mathbf{0}_{3\times1} \\ {}^{W}\boldsymbol{C}^{T}_{B(k+1)}\boldsymbol{g} & \mathbf{0}_{3\times1} \\ \mathbf{0}_{3\times1} & b_{az}\grave{\boldsymbol{e}}_{\mathbf{3}} \\ \mathbf{0}_{3\times1} & \mathbf{0}_{3\times1} \end{bmatrix} \tag{4.60}$$

Take the first null vector of the $^{1}\boldsymbol{\mathcal{N}}_{k}$. If the EKF-RINS is consistent, the null vector should satisfy $^{1}\boldsymbol{\mathcal{N}}_{k+1} = \hat{\boldsymbol{\Phi}}_{k}{}^{1}\boldsymbol{\mathcal{N}}_{t_k}$, where $\hat{\boldsymbol{\Phi}}_{k}$ is the discrete state transition matrix evaluated with the estimated states.

$$^{1}\boldsymbol{\mathcal{N}}'_{k+1,(:,1)} = \hat{\boldsymbol{\Phi}}_{k}{}^{1}\boldsymbol{\mathcal{N}}_{k,(:,1)} = \begin{bmatrix} \hat{\boldsymbol{\Phi}}_{k}^{(1,3)}{}^{W}\boldsymbol{C}^{T}_{B(k)}\boldsymbol{g} \\ \hat{\boldsymbol{\Phi}}_{k}^{(2,3)}{}^{W}\boldsymbol{C}^{T}_{B(k)}\boldsymbol{g} \\ \hat{\boldsymbol{\Phi}}_{k}^{(3,3)}{}^{W}\boldsymbol{C}^{T}_{B(k)}\boldsymbol{g} \\ \mathbf{0}_{3\times1} \\ \mathbf{0}_{3\times1} \end{bmatrix}. \tag{4.61}$$

Consider the third row of $^{1}\boldsymbol{\mathcal{N}}'_{k+1,(:,1)}$, and using (4.48) and (4.4) we obtain

$$\begin{aligned} \hat{\boldsymbol{\Phi}}_{k}^{(3,3)}{}^{W}\boldsymbol{C}^{T}_{B(k)}\boldsymbol{g} &= {}^{W}\hat{\boldsymbol{C}}^{T}_{B(k+1)}\boldsymbol{g} \\ &= \exp\left(\lfloor\boldsymbol{\delta\theta}\rfloor_{\times}\right){}^{W}\boldsymbol{C}^{T}_{B(k+1)}\boldsymbol{g} \\ &\neq {}^{W}\boldsymbol{C}^{T}_{B(k+1)}\boldsymbol{g}. \end{aligned} \tag{4.62}$$

Therefore, ${}^{1}\boldsymbol{\mathcal{N}}'_{k+1,(:,1)} \neq {}^{1}\boldsymbol{\mathcal{N}}_{k+1,(:,1)}$. Considering the second null space, we get

$$ {}^{1}\boldsymbol{\mathcal{N}}'_{k+1,(:,2)} = \hat{\boldsymbol{\Phi}}_k\, {}^{1}\boldsymbol{\mathcal{N}}_{k,(:,2)} = \begin{bmatrix} \hat{\boldsymbol{\Phi}}_k^{(1,4)} b_{az} \grave{\mathbf{e}}_{\mathbf{3}} \\ \hat{\boldsymbol{\Phi}}_k^{(2,4)} b_{az} \grave{\mathbf{e}}_{\mathbf{3}} \\ \hat{\boldsymbol{\Phi}}_k^{(3,4)} b_{az} \grave{\mathbf{e}}_{\mathbf{3}} \\ b_{az} \grave{\mathbf{e}}_{\mathbf{3}} \\ \mathbf{0}_{3\times 1} \end{bmatrix}. \tag{4.63} $$

The first three rows of the ${}^{1}\boldsymbol{\mathcal{N}}'_{k+1,(:,2)}$ are not zero, and therefore, ${}^{1}\boldsymbol{\mathcal{N}}'_{k+1,(:,2)} \neq {}^{1}\boldsymbol{\mathcal{N}}_{k+1,(:,2)}$. By multiplying the measurement Jacobian by the null vectors, it is straightforward to show that ${}^{1}\boldsymbol{\mathcal{N}}$ satisfies (4.59). Following a similar technique, it is straightforward to evaluate the rest of the true unobservable directions and determine the null spaces violate the conditions given in (4.58), and (4.59). A summary of the evaluated null spaces is shown in Table 4.1

4.4.1 Modification of state transition matrix $\boldsymbol{\Phi}_{\boldsymbol{k}}$

During each propagation step, the condition in (4.58) must be enforced for all the unobservable directions that violate it. This can be achieved by using the definitions of the state transition matrix in (4.39) and the corresponding null vectors to expand the relationship expressed in (4.58), and determining the requirements for each block

Table 4.1: Summery of Consistency Analysis

Scenario	**Null Vector**	Conditions	
		$\boldsymbol{\mathcal{N}}_{k+1} = \boldsymbol{\Phi}_k \boldsymbol{\mathcal{N}}_k$	$\mathbf{H}_k \boldsymbol{\mathcal{N}}_k = 0$
Scenario 1	${}^{1}\boldsymbol{\mathcal{N}}_{(:,1)}$	✗	✓
	${}^{1}\boldsymbol{\mathcal{N}}_{(:,2)}$	✗	✓
Scenario 3	${}^{3}\boldsymbol{\mathcal{N}}_{(:,1)}$	✗	✓
	${}^{3}\boldsymbol{\mathcal{N}}_{(:,2)}$	✗	✓
Scenario 4	${}^{4}\boldsymbol{\mathcal{N}}_{(:,1)}$	✗	✓
	${}^{4}\boldsymbol{\mathcal{N}}_{(:,2)}$	✗	✓
	${}^{4}\boldsymbol{\mathcal{N}}_{(:,3)}$	✓	✗
Scenario 5	${}^{5}\boldsymbol{\mathcal{N}}_{(:,1)}$	✓	✗
Scenario 6	${}^{6}\boldsymbol{\mathcal{N}}_{(:,1)}$	✗	✓
	${}^{6}\boldsymbol{\mathcal{N}}_{(:,2)}$	✗	✓

✓: Satisfies condition, ✗: Violates condition

elements of $\boldsymbol{\Phi}_k$. Consider the first unobservable direction of **Scenario 1** (see (4.60)).

$$\begin{bmatrix} \mathbf{0}_{3\times1} \\ \mathbf{0}_{3\times1} \\ {}^{W}\boldsymbol{C}^{T}_{B(k+1)}\boldsymbol{g} \\ \mathbf{0}_{3\times1} \\ \mathbf{0}_{3\times1} \end{bmatrix} = \begin{bmatrix} \boldsymbol{I_3} & \boldsymbol{\Phi}^{(1,2)} & \boldsymbol{\Phi}^{(1,3)} & \boldsymbol{\Phi}^{(1,4)} & \boldsymbol{\Phi}^{(1,5)} \\ \mathbf{0}_{3\times3} & \boldsymbol{\Phi}^{(2,2)} & \boldsymbol{\Phi}^{(2,3)} & \boldsymbol{\Phi}^{(2,4)} & \boldsymbol{\Phi}^{(2,5)} \\ \mathbf{0}_{3\times3} & \mathbf{0}_{3\times3} & \boldsymbol{\Phi}^{(3,3)} & \boldsymbol{\Phi}^{(3,4)} & \mathbf{0}_{3\times3} \\ \mathbf{0}_{3\times3} & \mathbf{0}_{3\times3} & \mathbf{0}_{3\times3} & \boldsymbol{I_3} & \mathbf{0}_{3\times3} \\ \mathbf{0}_{3\times3} & \mathbf{0}_{3\times3} & \mathbf{0}_{3\times3} & \mathbf{0}_{3\times3} & \boldsymbol{I_3} \end{bmatrix} \begin{bmatrix} \mathbf{0}_{3\times1} \\ \mathbf{0}_{3\times1} \\ {}^{W}\boldsymbol{C}^{T}_{B(k)}\boldsymbol{g} \\ \mathbf{0}_{3\times1} \\ \mathbf{0}_{3\times1} \end{bmatrix} = \begin{bmatrix} \boldsymbol{\Phi}_k^{(1,3)}\,{}^{W}\boldsymbol{C}^{T}_{B(k)}\boldsymbol{g} \\ \boldsymbol{\Phi}_k^{(2,3)}\,{}^{W}\boldsymbol{C}^{T}_{B(k)}\boldsymbol{g} \\ \boldsymbol{\Phi}_k^{(3,3)}\,{}^{W}\boldsymbol{C}^{T}_{B(k)}\boldsymbol{g} \\ \mathbf{0}_{3\times1} \\ \mathbf{0}_{3\times1} \end{bmatrix}. \tag{4.64}$$

Requirement for the third row of (4.64) is,

$$\begin{aligned} {}^{W}\hat{\boldsymbol{C}}^{T}_{B(k+1)}\boldsymbol{g} &= \boldsymbol{\Phi}_k^{(3,3)}\,{}^{W}\hat{\boldsymbol{C}}^{T}_{B(k)}\boldsymbol{g} \\ \boldsymbol{\Phi}_k^{(3,3)} &= {}^{B(k+1)}\hat{\boldsymbol{C}}_{B(K)}. \end{aligned} \tag{4.65}$$

The requirements for the first and the second rows are

$$\mathbf{\Phi}^{13W}\hat{\boldsymbol{C}}^{T}_{B(k)}\boldsymbol{g} = \mathbf{0} \tag{4.66}$$

$$\mathbf{\Phi}^{23W}\hat{\boldsymbol{C}}^{T}_{B(k)}\boldsymbol{g} = \mathbf{0}. \tag{4.67}$$

These expressions are a special case of expression that has the form of $\mathbf{Au} = \mathbf{w}$, where $\mathbf{w} = \mathbf{0}$. In order to full fill the constraint, the perturbation, $\mathbf{A}^*$ should be computed such that

$$\min_{\mathbf{A}^*} = \|\mathbf{A}^* - \mathbf{A}\|^2_{\Im}, \text{ s.t } \mathbf{A}^*\mathbf{u} = \mathbf{w}, \tag{4.68}$$

where $\|.\|^2_{\Im}$ represents the Frobenius matrix norm. The closed form solution for $\mathbf{A}^*$ that satisfies (4.68) can be calculated as [23]

$$\mathbf{A}^* = \mathbf{A} - (\mathbf{Au} - \mathbf{w})(\mathbf{u}^T\mathbf{u})^{-1}\mathbf{u}^T. \tag{4.69}$$

Once $\mathbf{\Phi}^{(1,3)}_k$ and $\mathbf{\Phi}^{(2,3)}_k$ are calculated using (4.69), the constrained discrete-time state transition matrix are constructed and conduct the covariance propagation expressed in (4.17).

4.4.2 Modification of $\mathbf{H}_k$

The observability constraint should be applied to the measurement Jacobian, **H** based on the null space vectors of each scenario. **Scenario 1** automatically satisfies this condition. Therefore there is no need to modify **H**. Under **Scenario 4**, the third null vector, ${}^4\boldsymbol{\mathcal{N}}_{k,(:,3)}$ violates (4.59), and therefore **H** must be modified.

$$\mathbf{H}_k{}^4\boldsymbol{\mathcal{N}}_{k,(:,3)} =$$

$$= \begin{bmatrix} \mathbf{0_3} & -\boldsymbol{K_d} & \mathbf{0_3} & \mathbf{0_3} & \boldsymbol{I_3} \\ \mathbf{R}_2 & \mathbf{0_3} & \mathbf{0_3} & \mathbf{0_3} & \mathbf{0_3} \end{bmatrix} \begin{bmatrix} ({}^W\hat{\boldsymbol{r}}_1 \times {}^W\hat{\boldsymbol{r}}_2) \\ \mathbf{0}_{3\times1} \\ \mathbf{0}_{3\times1} \\ \mathbf{0}_{3\times1} \\ \mathbf{0}_{3\times1} \end{bmatrix} = \mathbf{0}_{6\times1}, \tag{4.70}$$

where $\mathbf{R}_2 = \left[\frac{{}^W\boldsymbol{r}_1}{r_1}, \frac{{}^W\boldsymbol{r}_2}{r_2}\right]^T$.

The first block element of (4.70) requires that $\mathbf{R}_2(\hat{\boldsymbol{r}}_1 \times \hat{\boldsymbol{r}}_2) = \mathbf{0}_{2\times1}$. This constraint has the form of $\mathbf{Au} = \mathbf{0}$. We calculate the optimal $\mathbf{A}^*$ that satisfies the condition using the solution in (4.69) and modify the $\mathbf{R}_2$ of the measurement Jacobian. After modifying the Jacobian, proceed with the update step of the EKF.

4.5 Simulation Results

Average NEES and the average root mean square error (RMSE) are used to evaluate the consistency of the estimator. NEES of a consistent estimator with M-states χ^2 distribution with M degrees of freedom. Therefore, the average NEES of a large set of Monte-Carlo simulations will be close to the number of states. For example, the average NEES for the MAV location will be close to three if the estimator is consistent. A large deviation of the NEES from the expected value means a large inconsistency of the estimator.

The MATLAB simulator developed in Section 3.4 was used to simulate unobservable trajectories. Four different types of trajectories were used for the simulation. The first trajectory is a fully observable circular trajectory with a varying altitude, and the range anchors are placed at random locations. During the second trajectory, the MAV is kept stationary, and it is used for scenarios 1 and 4. The third trajectory has a vertical climb, and it is used for **Scenario 3** and **Scenario 6**. Since anchor locations do not contribute to unobservability under scenarios 1, 3, 4, and 6, the second and the third trajectories use the same range anchor locations as the first trajectory. The final trajectory is a circular trajectory with constant altitude, and it is used for **Scenario 4**. The two range anchors are placed on the same plane as the trajectory since it invokes unobservability. The first, third, and fourth trajectories are shown in Fig 4.1.

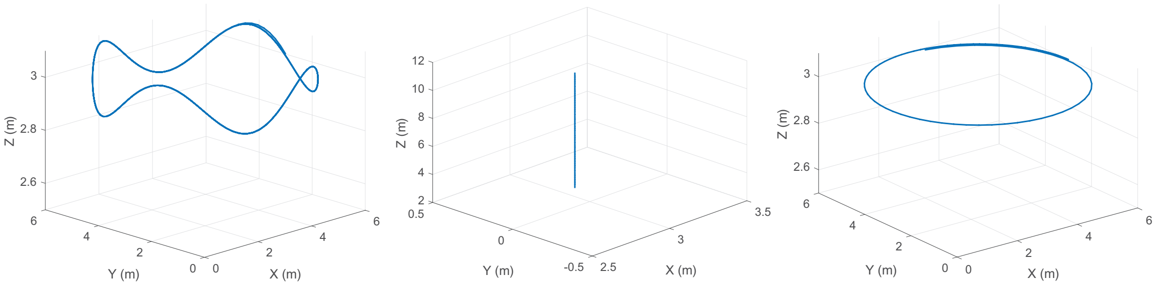

(a) (b) (c)

Fig. 4.1: Trajectories used in the simulation. (a) First trajectory: Circular with varying altitude, (b) Third trajectory: Vertical climb, (c) Fourth trajectory: Circular with constant altitude

Figure 4.2 shows the average NEES of the states for EKF-RINS with two and three range measurements. The MAV is flying on the first trajectory (Figure 4.1), and since the first trajectory is observable, the average NEES should have a value close to three. In Figure 4.2, it is evident that average NEES values are closer to the expected value, and these values will be used as the baseline of a consistent estimator.

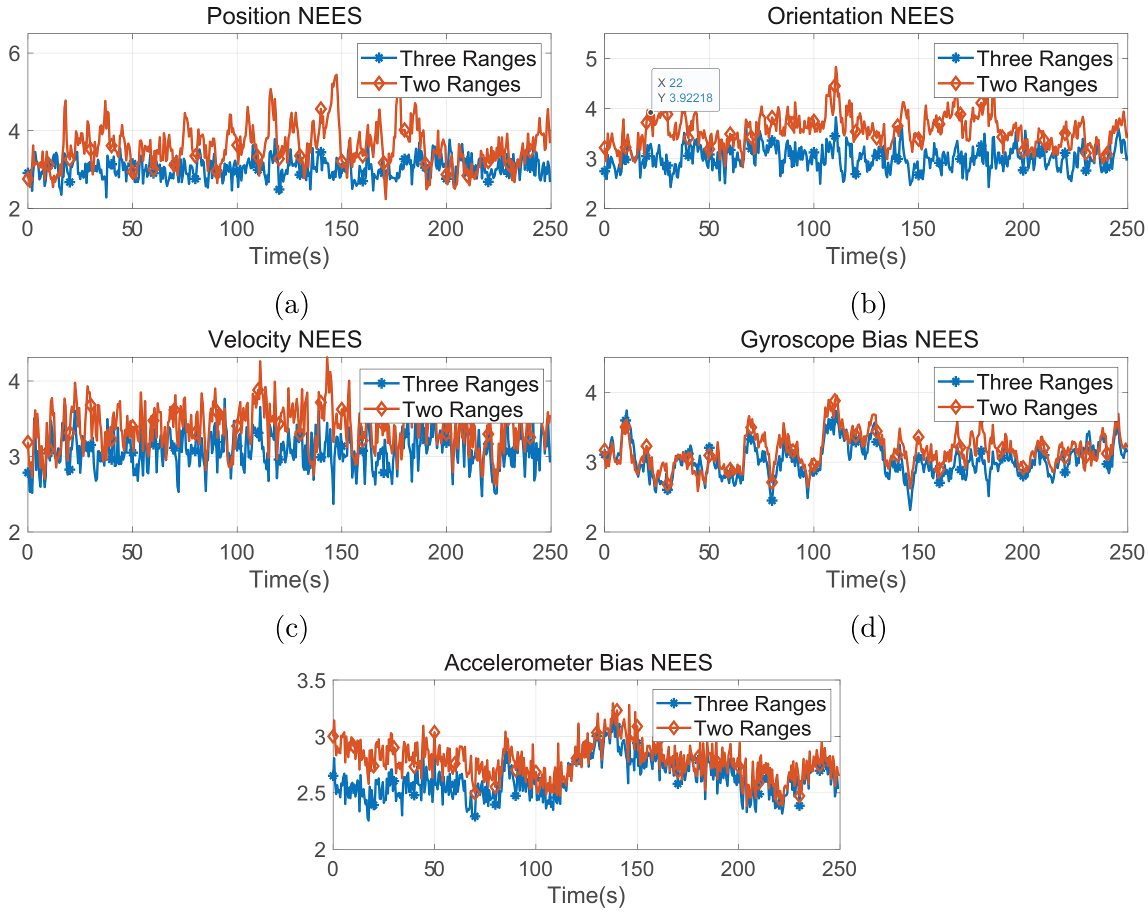

(a) (b) (c) (d) (e)

Fig. 4.2: Average NEES of 50 Monte-carlo simulations, under observable trajectory shown in Fig. 4.1a. (a) Position NEES, (b) Orientation NEES, (c) Velocity NEES, (d) Gyroscope bias NEES, (d) Accelerometer bias NEES.

Figure 4.3a shows the orientation NEES of the estimator under **Scenario 1**. When the MAV is stationary, the orientation NEES of the standard EKF-RINS increases. It can be seen that the orientation NEES of the EKF-RINS with the observability constraints also increases, but at a much lower rate than the standard EKF-RINS. A similar observation can be made with the NEES of the gyroscope bias in Figure 4.3c. There is a significant improvement in NEES when the observability constraints are applied. Figure 4.3b and Figure 4.3d show that the average RMSE of the angle and gyroscope bias estimates have decreased in observability constrained RINS compared to the standard EKF-RINS. These results imply that the consistency of the estimator has been improved by applying the observability constraints under **Scenario 1**.

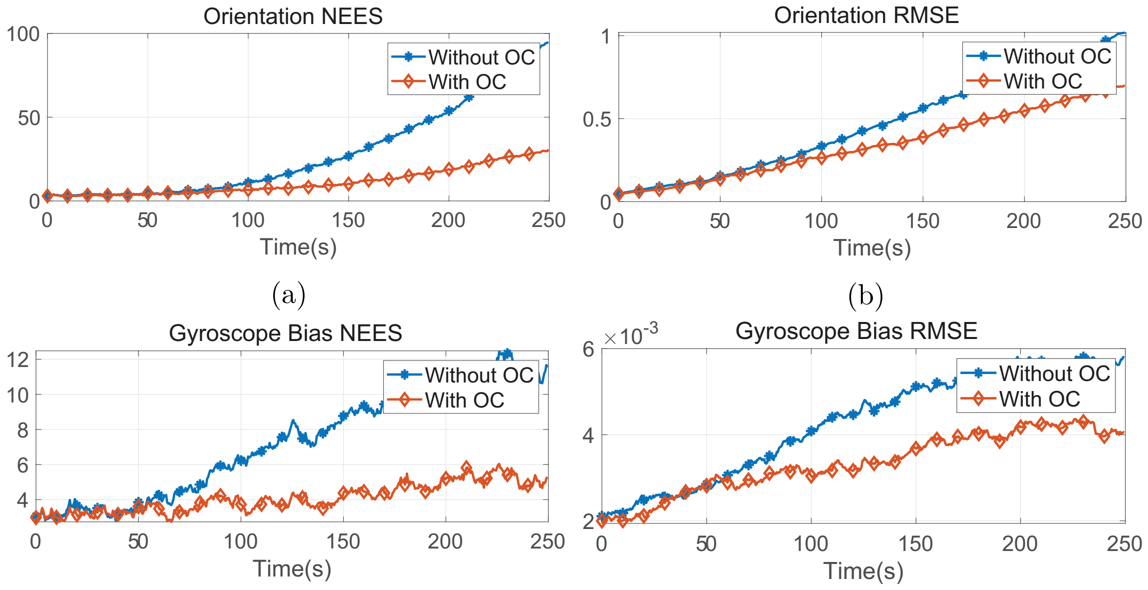

(a) (b)

(c) (d)

Fig. 4.3: **Scenario 1**: MAV is stationary with three range anchors. (a) Average orientation NEES, (b) Average orientation RMSE, (c) Average gyroscope bias NEES, (d) Average gyroscope bias RMSE.[3]

Figure 4.4 shows the results for **Scenario 3**, and it has two unobservable directions, rotation about the gravity and the gyroscope bias. Figure 4.4a, Figure 4.4b shows the NEES and RMSE of the orientation estimate. It is visible that there is a noticeable improvement when the observability constraints are applied. Similarly, improvement can be seen in the gyroscope bias estimate. Therefore, it is evident that applying observability constraints has improved the estimator's consistency under **Scenario 3**.

---

[3] OC: Observability Constraints.

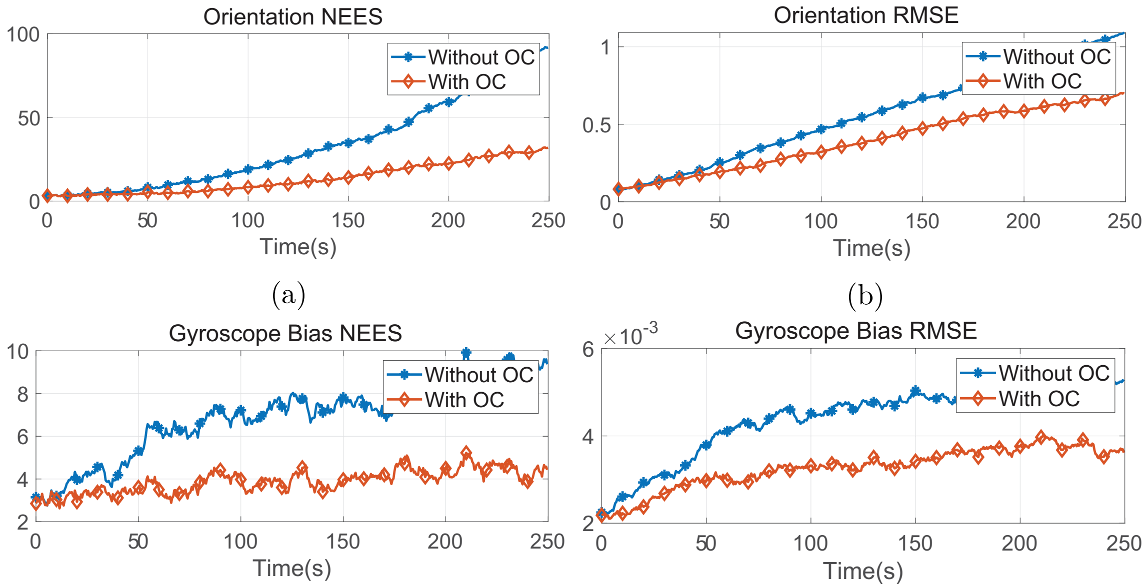

(a) (b) (c) (d)

Fig. 4.4: **Scenario 3**: MAV is flying vertically with three range anchors. (a) Average orientation NEES, (b) Average orientation RMSE, (c) Average gyroscope bias NEES, (d) Average gyroscope bias RMSE.

Under **Scenario 4**, the MAV is stationary with two range measurements, and the system has three unobservable directions, position, orientation of the MAV, and gyroscope bias. Figure 4.5a shows the NEES of the position estimate. The position NEES of standard EKF is significantly higher than the NEES values of other scenarios. However, the position NEES decreases substantially when the observability constraints are applied. Similarly, the position RMSE of the EKF with observability constraints is lower compared to the standard EKF Figure 4.5b. Orientation and gyroscope bias estimates also show improvements when the observability constraints are applied. Hence it is clear that the consistency of the EKF is improved under **Scenario 4**.

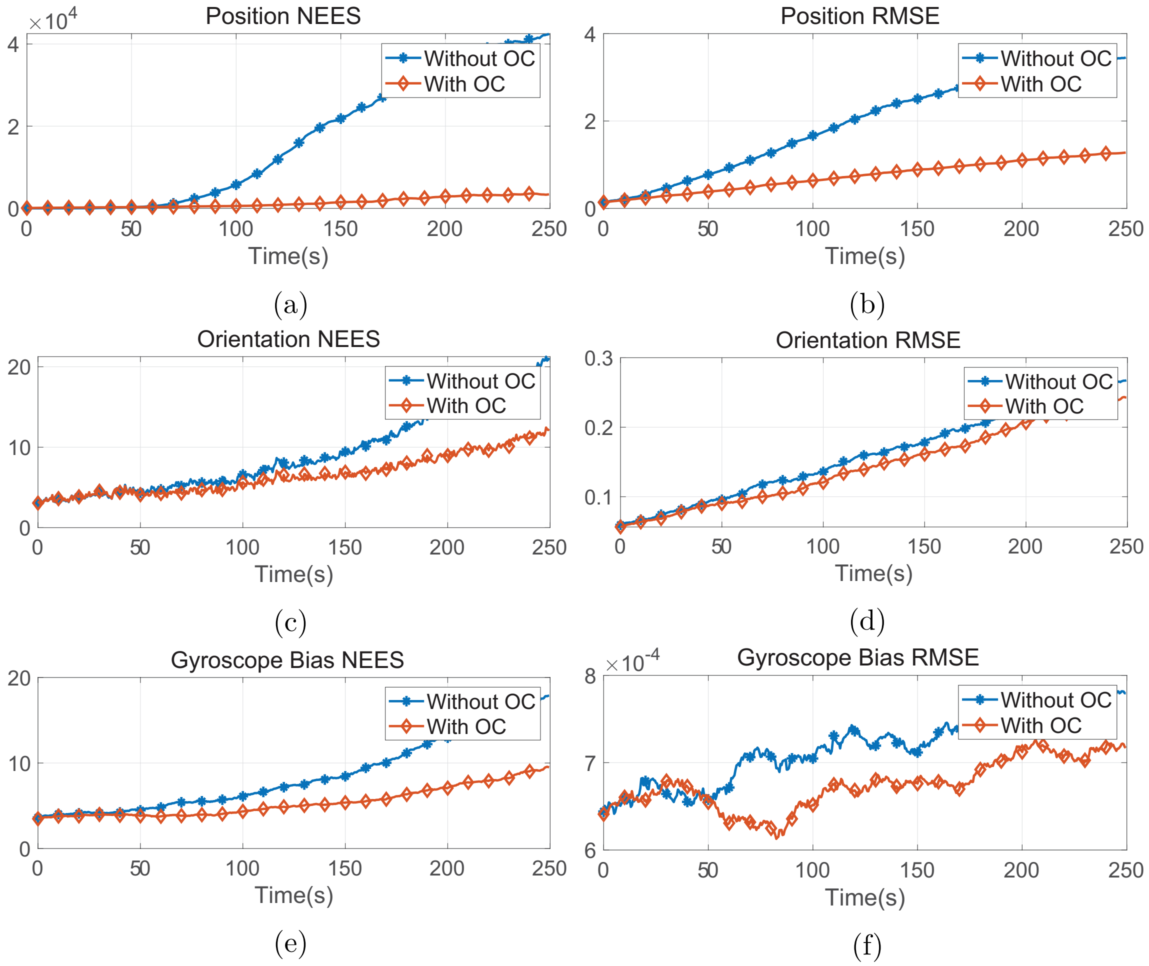

(a) (b)

(c) (d)

(e) (f)

Fig. 4.5: **Scenario 4**: MAV is stationary with two range anchors. (a) Average position NEES, (b) Average position RMSE, (c) Average orientation NEES, (d) Average orientation RMSE, (e) Average gyroscope bias NEES, (f) Average gyroscope bias RMSE.

The position of the MAV in the perpendicular direction to the plane of the MAV and the two anchors is unobservable in **Scenario 5**. Figure 4.6 shows an improvement in both position NEES and RMSE in observability constrained EKF. This shows that the consistency of the estimator is improved under **Scenario 5**.

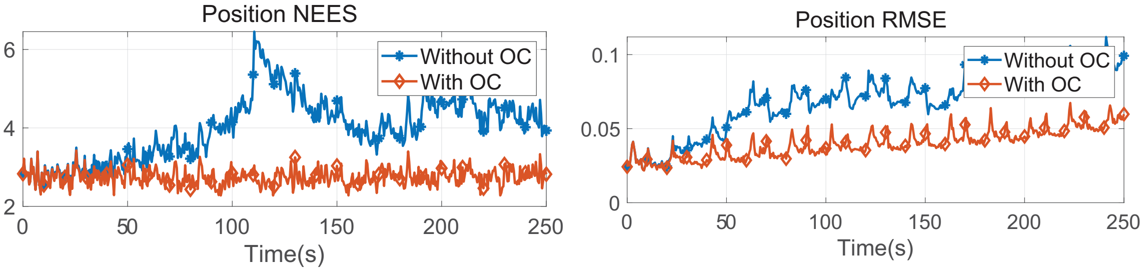

(a) (b)

Fig. 4.6: **Scenario 5**: MAV is flying on the plane of the MAV and the two anchors. (a) Average position NEES, (b) Average position RMSE.

Both **Scenario 6** and **Scenario 3** have the same unobservable directions. Results in Figure 4.7 show that there is improvement in both NEES and RMSE of the orientation and gyroscope bias estimates. Similar to **Scenario 3**, the observability constraints have improved the consistency of the estimation under **Scenario 6**.

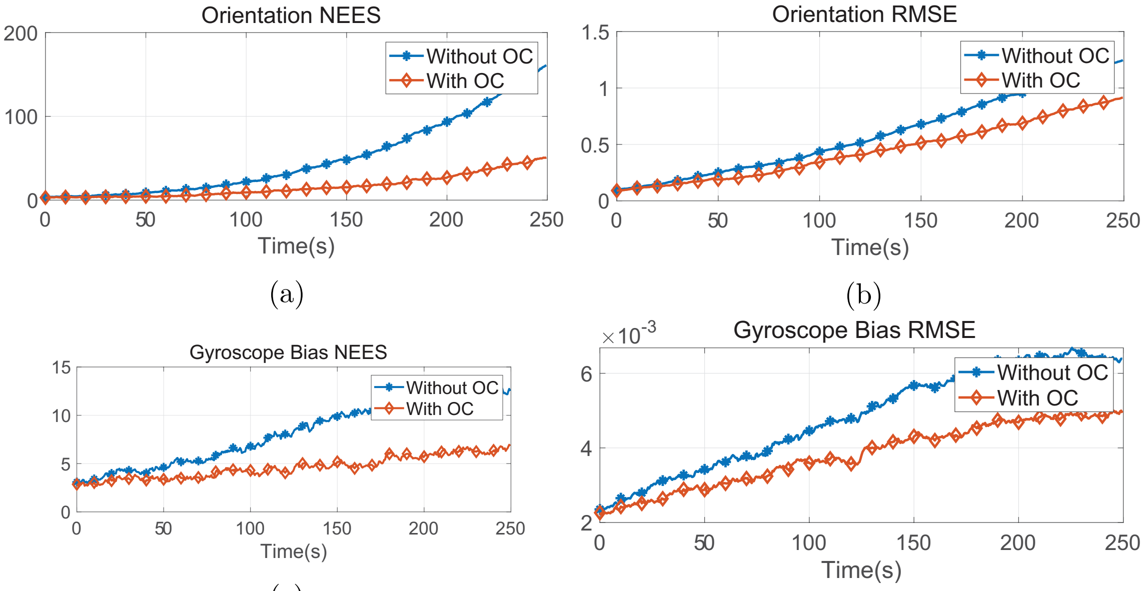

(c) (d)

Fig. 4.7: **Scenario 6**: MAV is flying vertically with two range anchors. (a) Average orientation NEES, (b) Average orientation RMSE, (c) Average gyroscope bias NEES, (d) Average gyroscope bias RMSE.

4.6 Summary

This chapter analyzes the consistency of the EKF implementation of the RINS with two and three range measurements and improves the consistency of the EKF during unobservable trajectories. In order to observe a significant increase in NEES of an unobservable state, the MAV should be flown on the unobservable trajectory for a longer duration. However, it is challenging to mimic the unobservable conditions for such a time span, and therefore, numerical simulations were used to verify the consistency improvement. The simulation results have shown significant improvement in the consistency of the estimator after applying the observability constraints. Additionally, the estimation accuracy has improved compared to the unconstrained EKF. When the consistency of the estimator is improved, the states are estimated with proper confidence levels. Therefore proper decisions can be made based on the more accurate state estimates and the corresponding covariances.

Chapter 5

Single Range Assisted Inertial Navigation System: Design and Observability Analysis

This chapter focuses on developing a range assisted inertial navigation system for MAVs using the least possible number of sensors. Two RINS formulations are presented where the first RINS uses the minimum number of sensors, i.e. a single range sensor, while the second RINS uses a magnetometer in addition to the single range sensor. An Observability study is carried out for both formulations to identify the feasibility and limitations of the design. Numerical simulations are conducted to evaluate the performance of the proposed inertial navigation systems.

5.1 Single Range assisted Inertial Navigation System

The range assisted inertial navigation system with a single range sensor has the same state vector as the two and three range assisted INS developed in section 3.2.1, and can be expressed as

$$\mathbf{x} = \begin{bmatrix} {}^{W}\boldsymbol{p}_{B}^{T} & {}^{B}\boldsymbol{v}^{T} & {}^{W}\boldsymbol{q}_{B}^{T} & {}^{B}\boldsymbol{b}_{g}^{T} & {}^{B}\boldsymbol{b}_{a}^{T} \end{bmatrix}^{T}, \tag{5.1}$$

The system model used for the RINS with a single range is similar to the two and three range assisted INS, and therefore, the evolution of the system states can be expressed as[1]

$$\begin{bmatrix} {}^{W}\dot{\boldsymbol{p}}_{B} \\ {}^{B}\dot{\boldsymbol{v}} \\ {}^{W}\dot{\boldsymbol{q}}_{B} \\ {}^{B}\dot{\boldsymbol{b}}_{g} \\ {}^{B}\dot{\boldsymbol{b}}_{a} \end{bmatrix} = \begin{bmatrix} {}^{W}\boldsymbol{C}_{B}{}^{B}\boldsymbol{v} \\ \lfloor {}^{B}\boldsymbol{v} \rfloor_{\times} \left({}^{B}\boldsymbol{\omega}_{m} - {}^{B}\boldsymbol{b}_{g} - \boldsymbol{\eta}_{\boldsymbol{\omega}} \right) - \boldsymbol{K}_{\boldsymbol{d}}{}^{B}\boldsymbol{v} + b_{az}\grave{\boldsymbol{e}}_{\boldsymbol{3}} - {}^{W}\boldsymbol{C}_{B}^{T}\boldsymbol{g} \\ \frac{1}{2}\boldsymbol{\Xi}(\boldsymbol{q}) \left[0 \ \left({}^{B}\boldsymbol{\omega}_{m} - {}^{B}\boldsymbol{b}_{g} - \boldsymbol{\eta}_{\boldsymbol{\omega}} \right)^{T} \right]^{T} \\ \boldsymbol{\eta}_{\boldsymbol{gb}} \\ \boldsymbol{\eta}_{\boldsymbol{ab}} \end{bmatrix}. \tag{5.2}$$

The measurement model of the RINS with a single range includes the accelerometer and a single range measurement to a ranging anchor at a known location, and it can be expressed as

$$\mathbf{y} = \begin{bmatrix} \mathbf{h}_{a}(\mathbf{x}) \\ \mathbf{h}_{r}(\mathbf{x}) \end{bmatrix} = \begin{bmatrix} -\boldsymbol{K}_{\boldsymbol{d}}{}^{B}\boldsymbol{v} + {}^{B}\boldsymbol{b}_{a} + \boldsymbol{\eta}_{\boldsymbol{a}} \\ r_{1} + \eta_{r1} \end{bmatrix}. \tag{5.3}$$

---

[1] See sections 3.2.1 and 3.2.2 for details.

5.1.1 Observability Analysis of RINS with a Single Range

Nonlinear observability analysis of the RINS with a single range measurement is carried out using the same techniques used for the two and three range assisted INS in Section 3.3. The system model of the single range assisted INS is the same as the RINS with three and two range measurements [see (3.44)]. The modified state vector with the Gibbs parameterization and the control affine form of the modified state space model in (5.2) can be expressed as

$$\mathbf{x} = \begin{bmatrix} {}^{W}\boldsymbol{p}_{B}^{T} & {}^{B}\boldsymbol{v}^{T} & {}^{W}\boldsymbol{s}_{B}^{T} & {}^{B}\boldsymbol{b}_{g}^{T} & {}^{B}\boldsymbol{b}_{a}^{T} \end{bmatrix}^{T}, \tag{5.4}$$

$$\begin{bmatrix} {}^{W}\dot{\boldsymbol{p}}_{B} \\ {}^{B}\dot{\boldsymbol{v}} \\ {}^{W}\dot{\boldsymbol{s}}_{B} \\ {}^{B}\dot{\boldsymbol{b}}_{g} \\ {}^{B}\dot{\boldsymbol{b}}_{a} \end{bmatrix} = \underbrace{\begin{bmatrix} {}^{W}\boldsymbol{C}_{B}{}^{B}\boldsymbol{v} \\ -\left\lfloor {}^{B}\boldsymbol{v} \right\rfloor_{\times} {}^{B}\boldsymbol{b}_{g} - \boldsymbol{K}_{\boldsymbol{d}}{}^{B}\boldsymbol{v} + b_{az}\grave{\mathbf{e}}_{\mathbf{3}} - {}^{W}\boldsymbol{C}_{B}^{T}\boldsymbol{g} \\ -\boldsymbol{D}^{B}\boldsymbol{b}_{g} \\ \mathbf{0}_{3\times1} \\ \mathbf{0}_{3\times1} \end{bmatrix}}_{\mathbf{f_0}} + \underbrace{\begin{bmatrix} \mathbf{0}_{3\times3} \\ \left\lfloor {}^{B}\boldsymbol{v} \right\rfloor_{\times} \\ \boldsymbol{D} \\ \mathbf{0}_{3\times3} \\ \mathbf{0}_{3\times3} \end{bmatrix}}_{\mathbf{f_1}} {}^{B}\boldsymbol{\omega}_{m}. \tag{5.5}$$

The modified range measurement model that replaces r_1 with $r^2/2$ can be expressed as

$$\mathbf{y} = \mathbf{h}(\mathbf{x}) = \begin{bmatrix} -\boldsymbol{K}_{\boldsymbol{d}}{}^{B}\boldsymbol{v} + {}^{B}\boldsymbol{b}_{a} \\ \frac{1}{2}r_{1}^{2} \end{bmatrix} = \begin{bmatrix} -\boldsymbol{K}_{\boldsymbol{d}}{}^{B}\boldsymbol{v} + {}^{B}\boldsymbol{b}_{a} \\ \frac{1}{2}\left({}^{W}\boldsymbol{p}_{B} - {}^{W}\boldsymbol{p}_{1}\right)^{T}\left({}^{W}\boldsymbol{p}_{B} - {}^{W}\boldsymbol{p}_{1}\right) \end{bmatrix}. \tag{5.6}$$

The nonlinear observability matrix for the RINS with the single range measurement is defined as follows [2]

$$\boldsymbol{\mathcal{O}} = \begin{bmatrix} \nabla \mathfrak{L}^0 \mathbf{h} \\ \nabla \mathfrak{L}^1_{\mathbf{f_0}} \mathbf{h} \\ \nabla \mathfrak{L}^2_{\mathbf{f_0 f_0}} \mathbf{h} \\ \nabla \mathfrak{L}^3_{\mathbf{f_0 f_0 f_0}} \mathbf{h} \end{bmatrix}. \tag{5.7}$$

A detailed calculation of the nonlinear observability matrix is given in Appendix C. Using (C.4),(C.7)(C.9), and (C.11), the observability matrix can be expressed as

$$\boldsymbol{\mathcal{O}}_{1R} =$$

$$\begin{bmatrix}
\mathbf{0}_{3\times3} & -\boldsymbol{K_d} & \mathbf{0}_{3\times3} & \mathbf{0}_{3\times3} & \boldsymbol{I_3} \\
{}^{W}\boldsymbol{r}_1^T & \mathbf{0}_{1\times3} & \mathbf{0}_{1\times3} & \mathbf{0}_{1\times3} & \mathbf{0}_{1\times3} \\
\mathbf{0}_{3\times3} & \boldsymbol{K_d}\left(\boldsymbol{K_d} - \lfloor {}^{B}\boldsymbol{b}_g \rfloor_\times\right) & \boldsymbol{K_d}\left\lfloor {}^{W}\boldsymbol{C}_B^T \boldsymbol{g} \right\rfloor_\times \boldsymbol{D}^{-1} & \boldsymbol{K_d}\lfloor {}^{B}\boldsymbol{v} \rfloor_\times & \boldsymbol{K_d}\boldsymbol{I}_{33} \\
({}^{W}\boldsymbol{C}_B {}^{B}\boldsymbol{v})^T & {}^{W}\boldsymbol{r}_1^{T\,W}\boldsymbol{C}_B & -{}^{W}\boldsymbol{r}_1^T \lfloor {}^{B}\boldsymbol{v} \rfloor_\times \left(\boldsymbol{D}^T\right)^{-1} & \mathbf{0}_{1\times3} & \mathbf{0}_{1\times3} \\
\mathbf{0}_{3\times3} & -\boldsymbol{K_d}\left(\boldsymbol{K_d} - \lfloor {}^{B}\boldsymbol{b}_g \rfloor_\times\right)^2 & \boldsymbol{\Theta} & \boldsymbol{\Phi} & \boldsymbol{K_d}\left(\boldsymbol{K_d} - \lfloor {}^{B}\boldsymbol{b}_g \rfloor_\times\right)\boldsymbol{I}_{33} \\
{}^{W}\ddot{\boldsymbol{p}}_B^T & 2{}^{B}\boldsymbol{v}^T - {}^{W}\boldsymbol{r}_1^{T\,W}\boldsymbol{C}_B\boldsymbol{K_d} & \boldsymbol{\Lambda_1} & \mathbf{0}_{1\times3} & {}^{W}\boldsymbol{r}_1^{T\,W}\boldsymbol{C}_B\boldsymbol{I}_{33} \\
\mathbf{0}_{3\times3} & \boldsymbol{K_d}\left(\boldsymbol{K_d} - \lfloor {}^{B}\boldsymbol{b}_g \rfloor_\times\right)^3 & \boldsymbol{\Pi}_1 & \boldsymbol{\Pi}_2 & -\boldsymbol{K_d}\left(\boldsymbol{K_d} - \lfloor {}^{B}\boldsymbol{b}_g \rfloor_\times\right)^2\boldsymbol{I}_{33} \\
\boldsymbol{\Pi}_3 & \boldsymbol{\Pi}_4 & \boldsymbol{\Pi}_5 & \boldsymbol{\Pi}_6 & \boldsymbol{\Pi}_7
\end{bmatrix} \tag{5.8}$$

The block elements $\boldsymbol{\Pi}_1$ to $\boldsymbol{\Pi}_7$ are defined in (C.12) - (C.18).

Lemma 5.1. *When the MAV is flying in a generic trajectory, the unobservable subspace of the observability matrix* $\boldsymbol{\mathcal{O}}_{1R}$ *is spanned by the following direction*

$${}^{7}\boldsymbol{\mathcal{N}} = \begin{bmatrix} (\boldsymbol{g} \times {}^{W}\boldsymbol{r}_1)^T & \mathbf{0}_{1\times3} & (\boldsymbol{D}^{W}\boldsymbol{C}_B^T\boldsymbol{g})^T & \mathbf{0}_{1\times3} & \mathbf{0}_{1\times3} \end{bmatrix}^T. \tag{5.9}$$

---

[2] Since the measurement function is four dimensional, the gradient of the third order Lie derivative is required to construct the observability matrix that has sufficient rows to have the rank.

Proof. First, let's prove that the second, fourth, and fifth block columns do not contribute to forming the basis of the null space of $\boldsymbol{\mathcal{O}}_{1R}$ when the MAV is flying in a generic trajectory. The first element of the second and the fifth block columns are diagonal matrices, and therefore, each block column has full rank. Additionally, by looking at the $\boldsymbol{\mathcal{O}}_{1R_{(3,2)}}$, and $\boldsymbol{\mathcal{O}}_{1R_{(3,5)}}$, it is obvious that the second and the fifth block columns are independent. Hence, the second and the fifth block columns do not contribute to the basis of the null space. The non-zero block elements of the second block column can be expressed as

$$\boldsymbol{\mathcal{O}}'_{\mathbf{1}\boldsymbol{R}_{(:,4)}} = \left[\; (\boldsymbol{K_d} \lfloor {}^{B}\boldsymbol{v} \rfloor_{\times})^T \quad \boldsymbol{\Phi}^T \quad \boldsymbol{\Pi}_2^T \quad \boldsymbol{\Pi}_6^T \; \right]^T \tag{5.10}$$

By analyzing the elements of (5.10), it is straightforward to show that the fourth block column has full rankHence, the second, fourth and fifth block columns do not contribute to the basis of the null space under a generic trajectory.

The fact that ${}^{7}\boldsymbol{\mathcal{N}}$ spans the unobservable subspace of $\boldsymbol{\mathcal{O}}_{1R}$ can be verified by multiplying each block row of $\boldsymbol{\mathcal{O}}_{1R}$ with ${}^{7}\boldsymbol{\mathcal{N}}$. It is straightforward to show that $\boldsymbol{\mathcal{O}}_{1R_{(2,:)}}{}^{7}\boldsymbol{\mathcal{N}} = 0$, and $\boldsymbol{\mathcal{O}}_{1R_{(j,:)}}{}^{7}\boldsymbol{\mathcal{N}} = \mathbf{0}_{3\times 1},\ j = 3, 5, 7$.

$$\begin{aligned} \boldsymbol{\mathcal{O}}_{1R_{(4,:)}}{}^{7}\boldsymbol{\mathcal{N}} &= ({}^{W}\boldsymbol{C}_{B}{}^{B}\boldsymbol{v})^T(\boldsymbol{g} \times {}^{W}\boldsymbol{r}_1) - {}^{W}\boldsymbol{r}_1^T \lfloor {}^{W}\boldsymbol{C}_{B}{}^{B}\boldsymbol{v} \rfloor_{\times} \left(\boldsymbol{D}^T\right)^{-1} \boldsymbol{D}{}^{W}\boldsymbol{C}_{B}^T\boldsymbol{g} \\ &= ({}^{W}\boldsymbol{C}_{B}{}^{B}\boldsymbol{v})^T(\boldsymbol{g} \times {}^{W}\boldsymbol{r}_1) - {}^{W}\boldsymbol{r}_1^T({}^{W}\boldsymbol{C}_{B}{}^{B}\boldsymbol{v} \times \boldsymbol{g}) \\ &= 0 \end{aligned} \tag{5.11}$$

$$\begin{aligned} \boldsymbol{\mathcal{O}}_{1R_{(7,:)}}{}^{7}\boldsymbol{\mathcal{N}} &= {}^{W}\ddot{\boldsymbol{p}}_{B}^T(\boldsymbol{g} \times {}^{W}\boldsymbol{r}_1) - \boldsymbol{\Lambda_1}\boldsymbol{D}{}^{W}\boldsymbol{C}_{B}^T\boldsymbol{g} \\ &= \left({}^{W}\boldsymbol{C}_{B}\left(-\boldsymbol{K_d}{}^{B}\boldsymbol{v} + b_{az}\grave{\boldsymbol{e}}_{\mathbf{3}}\right)\right)^T\left(\boldsymbol{g} \times {}^{W}\boldsymbol{r}_1\right) - {}^{W}\boldsymbol{r}_1^T\left(\lfloor {}^{W}\boldsymbol{C}_{B}\left(-\boldsymbol{K_d}{}^{B}\boldsymbol{v} + b_{az}\grave{\boldsymbol{e}}_{\mathbf{3}}\right)\rfloor_{\times}\right)\boldsymbol{g} \\ &= 0 \end{aligned} \tag{5.12}$$

Following similar steps, it can be shown that $\boldsymbol{\mathcal{O}}_{1R_{(8,:)}}{}^{7}\boldsymbol{\mathcal{N}} = 0$. Hence ${}^{7}\boldsymbol{\mathcal{N}}$ spans the null space of the RINS with a single range measurement. □

Lemma 5.1 shows that the RINS with a single range measurement is unobservable under any generic trajectory. The unobservable direction ${}^{7}\boldsymbol{\mathcal{N}}$ can be interpreted as the orientation about the gravity vector and the perpendicular direction to both gravity and the range vectors. It should be noted that under special trajectories, i.e., MAV being stationary, constant velocity, etc., the dimension of the unobservable subspace can increase.

5.1.2 Simulation Results

The Matlab simulator developed in Section 3.4 was used to simulate the MAV flying on a circular trajectory with varying altitudes (Fig. 5.4a), and the RINS with a single range measurement was used to estimate the pose of the MAV. Fig. 5.2a, and Fig. 5.2b show the total position error and the total orientation error of the single range INS for five different range anchor locations.

The location of the single range anchor for the five simulations are given in Table 5.1(Fig. 5.1).

Table 5.1: Location of the single range anchor used for single range assisted INS

	Location (m)
Simulation 1	(2.7, 2.1, 8.8)
Simulation 2	(4.5, 8.7, 2.2)
Simulation 3	(9.5, 2.7, 1.8)
Simulation 4	(6.3, 6.8, 2.1)
Simulation 5	(1.2, 0.9, 1.8)

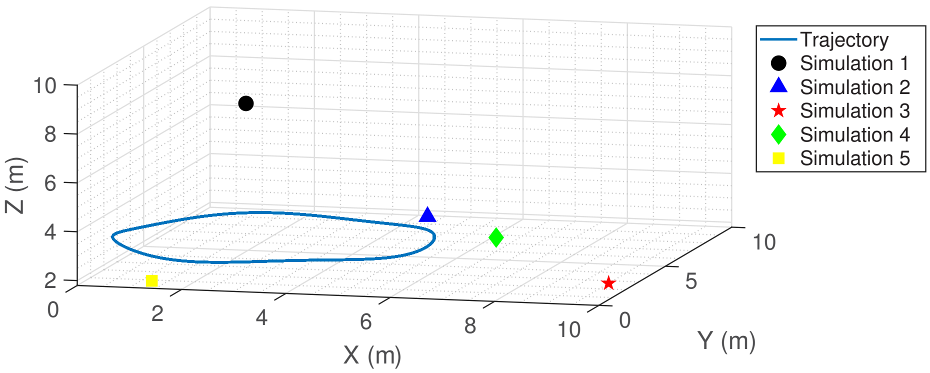

Fig. 5.1: Locations of the single range anchor used in the five simulations of single range INS

In Fig. 5.2a, it can be observed that the position error covariance does not diverge, even though the position state is unobservable along the direction of $(\boldsymbol{g} \times {}^{W}\boldsymbol{r}_1)^T$ (See (5.9)). Since the MAV is flying in a circular trajectory, the direction $(\boldsymbol{g} \times {}^{W}\boldsymbol{r}_1)^T$ always changes. Therefore, as Fig. 5.2a shows the position covariance increases during a portion of the circle and decreases during the rest. On the other hand, the orientation about the gravity vector does not change based on the trajectory. In Fig 5.2b there is a slight increase in the total angle covariance as the trajectory progresses.

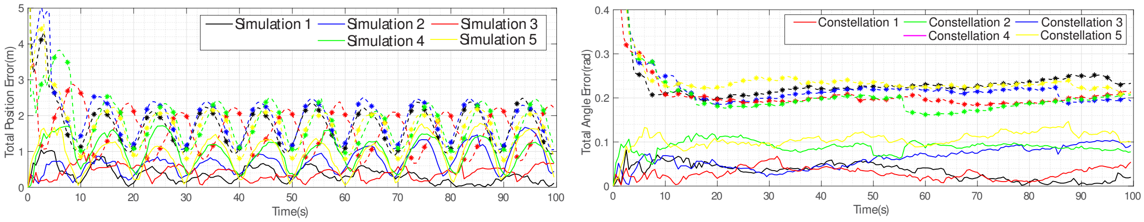

(a) (b)

Fig. 5.2: Single range assisted INS (a) Total Position error and 3σ boundary, (b) Total Angle Error and 3σ boundary. (—) is total error, and (-∗-) is 3σ boundary.

Fig. 5.3 shows the mean absolute orientation error of 25 Monte-Carlo simulations. The range anchor location of the Constellation 1 is used for the simulations. In Fig. 5.3 it is clearly visible that the covariance of the yaw angle (rotation about the gravity) error diverges while the covariance of the roll and pitch estimates remain bounded.

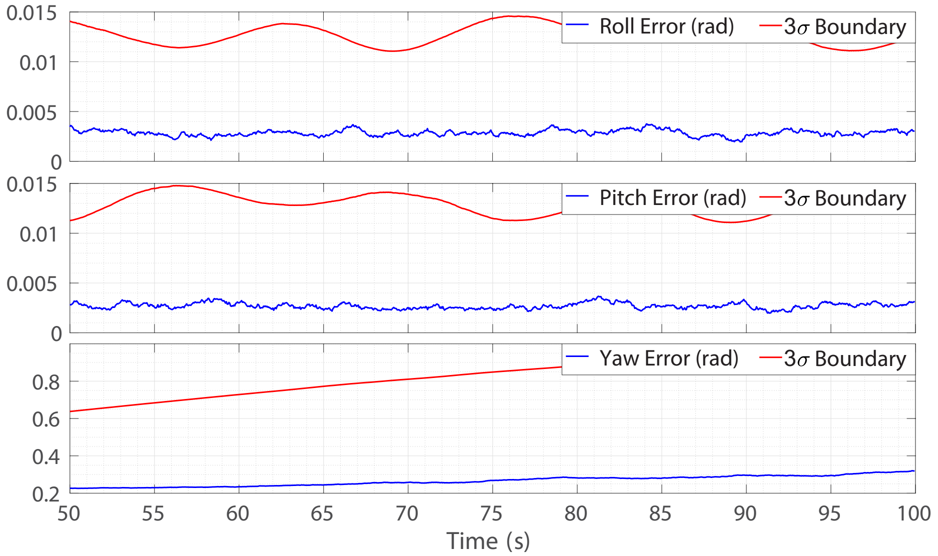

Fig. 5.3: Single range assisted INS orientation error and the 3σ boundary of 25 Monte-Carlo simulations

5.2 Single Range and Magnetometer Assisted Inertial Navigation System

Since the RINS with a single range measurement is unobservable for any trajectory, this section proposes a RINS design that utilizes a magnetometer in addition to the single range measurement (M-RINS). An observability study is carried out to show that the proposed RINS is observable during a generic trajectory, and to identify specific trajectories that render the system unobservable.

5.2.1 System Model

The states of the proposed RINS with single range and magnetometer measurements consist of the position, velocity, orientation of the MAV, and the accelerometer bias.

The 13 dimensional state vector is expressed as

$$\mathbf{x} = \begin{bmatrix} {}^{W}\boldsymbol{p}_{B}^{T} & {}^{B}\boldsymbol{v}^{T} & {}^{W}\boldsymbol{q}_{B}^{T} & {}^{B}\boldsymbol{b}_{a}^{T} \end{bmatrix}^{T}. \tag{5.13}$$

The proposed RINS does not include the gyroscope bias for two main reasons. The most important reason being the gyroscope bias is observable in an attitude and heading reference system (AHRS) that incorporates the magnetometer measurements (See Appendix D). Secondly, omitting the gyroscope bias simplifies the observability analysis. Since the gyroscope bias is observable under any trajectory, the unobservable conditions identified in the observability analysis will hold true even when the gyroscope bias is incorporated into the system model. This can be clearly seen in the simulation results shown in Section 5.2.5.

The system model without the gyroscope bias can be expressed as

$$\begin{bmatrix} {}^{W}\dot{\boldsymbol{p}}_{B} \\ {}^{B}\dot{\boldsymbol{v}} \\ {}^{W}\dot{\boldsymbol{q}}_{B} \\ {}^{B}\dot{\boldsymbol{b}}_{a} \end{bmatrix} = \begin{bmatrix} {}^{W}\boldsymbol{C}_{B}{}^{B}\boldsymbol{v} \\ \left\lfloor {}^{B}\boldsymbol{v} \right\rfloor_{\times} \left({}^{B}\boldsymbol{\omega}_{m} - \boldsymbol{\eta}_{\omega} \right) - \boldsymbol{K}_{\boldsymbol{d}}{}^{B}\boldsymbol{v} + b_{az}\grave{\mathbf{e}}_{\mathbf{3}} - {}^{W}\boldsymbol{C}_{B}^{T}\boldsymbol{g} \\ \frac{1}{2}\boldsymbol{\Xi}(\boldsymbol{q}) \left[0 \; \left({}^{B}\boldsymbol{\omega}_{m} - \boldsymbol{\eta}_{\omega} \right)^{T} \right]^{T} \\ \boldsymbol{\eta}_{\boldsymbol{ab}} \end{bmatrix}. \tag{5.14}$$

5.2.2 Measurement Model

A magnetometer measures the local magnetic field present around the MAV. Generally, the local magnetic field comprises the earth's magnetic field ${}^{W}\boldsymbol{\mu}$, and the local magnetic effects $\boldsymbol{\mu}_{ext}$. The local magnetic effects can be categorized as hard iron or soft iron effects. The impact of these effects on the magnetometer reading can be minimized through offline calibration of the magnetometer [101], or auto-calibration during the flight [102]. In this thesis, it is assumed that the magnetometer is calibrated and measures the earth's magnetic field ${}^{W}\boldsymbol{\mu}$. The mathematical model of the magnetometer measurement can be expressed as

$$
{}^{B}\boldsymbol{\mu} = {}^{W}\boldsymbol{C}_{B}^{T}\,{}^{W}\boldsymbol{\mu} + \boldsymbol{\eta}_{\boldsymbol{\mu}}, \tag{5.15}
$$

where ${}^{B}\boldsymbol{\mu}$ is the magnetometer measurement, and $\boldsymbol{\eta}_{\boldsymbol{\mu}}$ is the zero-mean white Gaussian noise with a standard deviation of $\boldsymbol{\sigma}_{\boldsymbol{\mu}}$.

The measurement model for the single range and magnetometer assisted INS can be expressed as

$$
\mathbf{y} = \begin{bmatrix} \mathbf{h}_a(\mathbf{x}) \\ \mathbf{h}_\mu(\mathbf{x}) \\ \mathbf{h}_r(\mathbf{x}) \end{bmatrix} = \begin{bmatrix} -\boldsymbol{K_d}\,{}^{B}\boldsymbol{v} + {}^{B}\boldsymbol{b}_a + \boldsymbol{\eta_a} \\ {}^{W}\boldsymbol{C}_{B}^{T}\,{}^{W}\boldsymbol{\mu} + \boldsymbol{\eta}_{\boldsymbol{\mu}} \\ r_1 + \eta_{r1} \end{bmatrix}, \tag{5.16}
$$

5.2.3 Observability Analysis

The state vector and the control affine form of the system model used for the nonlinear observability analysis can be expressed as

$$
\mathbf{x} = \begin{bmatrix} {}^{W}\boldsymbol{p}_{B}^{T} & {}^{B}\boldsymbol{v}^{T} & {}^{W}\boldsymbol{s}_{B}^{T} & {}^{B}\boldsymbol{b}_{g}^{T} & {}^{B}\boldsymbol{b}_{a}^{T} \end{bmatrix}^{T}, \tag{5.17}
$$

$$
\begin{bmatrix} {}^{W}\dot{\boldsymbol{p}}_{B} \\ {}^{B}\dot{\boldsymbol{v}} \\ {}^{W}\dot{\boldsymbol{s}}_{B} \\ {}^{B}\dot{\boldsymbol{b}}_{a} \end{bmatrix} = \underbrace{\begin{bmatrix} {}^{W}\boldsymbol{C}_{B}\,{}^{B}\boldsymbol{v} \\ -\boldsymbol{K_d}\,{}^{B}\boldsymbol{v} + b_{az}\grave{\boldsymbol{e}}_{\mathbf{3}} - {}^{W}\boldsymbol{C}_{B}^{T}\boldsymbol{g} \\ \mathbf{0}_{3\times 1} \\ \mathbf{0}_{3\times 1} \end{bmatrix}}_{\mathbf{f_0}} + \underbrace{\begin{bmatrix} \mathbf{0}_{3\times 3} \\ \lfloor {}^{B}\boldsymbol{v} \rfloor_{\times} \\ \boldsymbol{D} \\ \mathbf{0}_{3\times 3} \end{bmatrix}}_{\mathbf{f_1}} {}^{B}\boldsymbol{\omega}_m \tag{5.18}
$$

Similar to the previous analysis, the range measurement is substituted by the square of the range measurement. The measurement model used for the observability analysis can be expressed as

$$\mathbf{y} = \mathbf{h}(\mathbf{x}) = \begin{bmatrix} -\boldsymbol{K_d}\,{}^{B}\boldsymbol{v} + {}^{B}\boldsymbol{b}_a \\ \\ {}^{W}\boldsymbol{C}_{B}^{T}\,{}^{W}\boldsymbol{\mu} \\ \\ \frac{1}{2}r_1^2 \end{bmatrix} = \begin{bmatrix} -\boldsymbol{K_d}\,{}^{B}\boldsymbol{v} + {}^{B}\boldsymbol{b}_a \\ \\ {}^{W}\boldsymbol{C}_{B}^{T}\,{}^{W}\boldsymbol{\mu} \\ \\ \frac{1}{2}\left({}^{W}\boldsymbol{p}_{B} - {}^{W}\boldsymbol{p}_1\right)^{T}\left({}^{W}\boldsymbol{p}_{B} - {}^{W}\boldsymbol{p}_1\right) \end{bmatrix}. \tag{5.19}$$

The zeroth order Lie derivative and its gradient of (5.19) can be expressed as

$$\mathfrak{L}^0\mathbf{h} = \mathbf{h}(\mathbf{x}) \tag{5.20}$$

$$\nabla\mathfrak{L}^0\mathbf{h} = \begin{bmatrix} \mathbf{0}_{3\times3} & -\boldsymbol{K_d} & \mathbf{0}_{3\times3} & \boldsymbol{I_3} \\ \\ \mathbf{0}_{3\times3} & \mathbf{0}_{3\times3} & \left\lfloor {}^{W}\boldsymbol{C}_{B}^{T}\,{}^{W}\boldsymbol{\mu} \right\rfloor_{\times} \boldsymbol{D}^{-1} & \mathbf{0}_{3\times3} \\ \\ {}^{W}\boldsymbol{r}_1^{T} & \mathbf{0}_{1\times3} & \mathbf{0}_{1\times3} & \mathbf{0}_{1\times3} \end{bmatrix}, \tag{5.21}$$

The first order Lie derivatives with respect to $\mathbf{f_0}$ can be expressed as

$$\mathfrak{L}^1_{\mathbf{f_0}}\mathbf{h} = \nabla\mathfrak{L}^0\mathbf{h}\cdot\mathbf{f_0} = \begin{bmatrix} -\boldsymbol{K_d}\left(-\boldsymbol{K_d}\,{}^{B}\boldsymbol{v} + b_{az}\grave{\mathbf{e}}_{\mathbf{3}} - {}^{W}\boldsymbol{C}_{B}^{T}\boldsymbol{g}\right) \\ \\ \mathbf{0}_{3\times1} \\ \\ {}^{W}\boldsymbol{r}_1^{T}\,{}^{W}\boldsymbol{C}_{B}\,{}^{B}\boldsymbol{v} \end{bmatrix} = \begin{bmatrix} -\boldsymbol{K_d}\,{}^{W}\boldsymbol{C}_{B}^{T}\,{}^{W}\ddot{\boldsymbol{p}}_{B} \\ \\ \mathbf{0}_{3\times1} \\ \\ \left({}^{W}\boldsymbol{C}_{B}^{T}\,{}^{W}\boldsymbol{r}_1\right)^{T}\,{}^{B}\boldsymbol{v} \end{bmatrix}, \tag{5.22}$$

where ${}^{W}\ddot{\boldsymbol{p}}_{B} = {}^{W}\boldsymbol{C}_{B}\left(-\boldsymbol{K_d}\,{}^{B}\boldsymbol{v} + b_{az}\grave{\mathbf{e}}_{\mathbf{3}} - {}^{W}\boldsymbol{C}_{B}^{T}\boldsymbol{g}\right)$.

Since the second block row of $\mathfrak{L}^1_{\mathbf{f_0}}\mathbf{h}$ is zero, it does not contribute to the higher order Lie derivatives. Therefore the second block row is left out in the next calculations.

The gradient of the $\mathfrak{L}^1_{\mathbf{f_0}}\mathbf{h}$ can be expressed as

$$\nabla\mathfrak{L}^1_{\mathbf{f_0}}\mathbf{h} = \begin{bmatrix} \mathbf{0}_{3\times3} & \boldsymbol{K}_{\boldsymbol{d}}^2 & \boldsymbol{K}_{\boldsymbol{d}}\left\lfloor {}^{W}\boldsymbol{C}_{B}^{T}\boldsymbol{g}\right\rfloor_{\times}\boldsymbol{D}^{-1} & -\boldsymbol{K}_{\boldsymbol{d}}\boldsymbol{I}_{33} \\ ({}^{W}\boldsymbol{C}_{B}{}^{B}\boldsymbol{v})^{T} & ({}^{W}\boldsymbol{C}_{B}^{T\,W}\boldsymbol{r}_1)^{T} & {}^{B}\boldsymbol{v}^{T}\left\lfloor {}^{W}\boldsymbol{C}_{B}^{T\,W}\boldsymbol{r}_1\right\rfloor_{\times}\boldsymbol{D}^{-1} & \mathbf{0}_{1\times3} \end{bmatrix}, \tag{5.23}$$

Similarly, higher order Lie derivatives and their gradients can be calculated as

$$\mathfrak{L}^2_{\mathbf{f_0}\mathbf{f_0}}\mathbf{h} = \nabla\mathfrak{L}^1_{\mathbf{f_0}}\mathbf{h}\cdot\mathbf{f_0} = \begin{bmatrix} \boldsymbol{K}_{\boldsymbol{d}}^{2\,W}\boldsymbol{C}_{B}^{T\,W}\ddot{\boldsymbol{p}}_{B} \\ {}^{B}\boldsymbol{v}^{T\,B}\boldsymbol{v} + ({}^{W}\boldsymbol{C}_{B}^{T\,W}\boldsymbol{r}_1)^{T\,W}\boldsymbol{C}_{B}^{T\,W}\ddot{\boldsymbol{p}}_{B} \end{bmatrix} \tag{5.24}$$

$$\nabla\mathfrak{L}^2_{\mathbf{f_0}\mathbf{f_0}}\mathbf{h} = \begin{bmatrix} \mathbf{0}_{3\times3} & -\boldsymbol{K}_{\boldsymbol{d}}^3 & -\boldsymbol{K}_{\boldsymbol{d}}^2\left\lfloor {}^{W}\boldsymbol{C}_{B}^{T}\boldsymbol{g}\right\rfloor_{\times}\boldsymbol{D}^{-1} & \boldsymbol{K}_{\boldsymbol{d}}^2\boldsymbol{I}_{33} \\ {}^{W}\ddot{\boldsymbol{p}}_{B}^{T} & \left(2{}^{B}\boldsymbol{v} - \boldsymbol{K}_{\boldsymbol{d}}{}^{W}\boldsymbol{C}_{B}^{T\,W}\boldsymbol{r}_1\right)^{T}\boldsymbol{K}_{\boldsymbol{d}} & (-\boldsymbol{K}_{\boldsymbol{d}}{}^{B}\boldsymbol{v} + b_{az}\grave{\boldsymbol{e}}_{\mathbf{3}})^{T}\left\lfloor {}^{W}\boldsymbol{C}_{B}^{T\,W}\boldsymbol{r}_1\right\rfloor_{\times}\boldsymbol{D}^{-1} & \mathbf{0}_{1\times3} \end{bmatrix}. \tag{5.25}$$

$$\mathfrak{L}^3_{\mathbf{f_0}\mathbf{f_0}\mathbf{f_0}}\mathbf{h} = \nabla\mathfrak{L}^2_{\mathbf{f_0}\mathbf{f_0}}\mathbf{h}\cdot\mathbf{f_0} = \begin{bmatrix} \boldsymbol{K}_{\boldsymbol{d}}^{3\,W}\boldsymbol{C}_{B}^{T\,W}\ddot{\boldsymbol{p}}_{B} \\ \left({}^{W}\boldsymbol{C}_{B}^{T\,W}\ddot{\boldsymbol{p}}_{B}\right)^{T}\left(3{}^{B}\boldsymbol{v} - \boldsymbol{K}_{\boldsymbol{d}}({}^{W}\boldsymbol{C}_{B}^{T\,W}\boldsymbol{r}_1)\right) \end{bmatrix} \tag{5.26}$$

$$\nabla\mathfrak{L}^3_{\mathbf{f_0}\mathbf{f_0}\mathbf{f_0}}\mathbf{h} = \begin{bmatrix} \mathbf{0}_{3\times3} & -\boldsymbol{K}_{\boldsymbol{d}}^3 & -\boldsymbol{K}_{\boldsymbol{d}}^2\left\lfloor {}^{W}\boldsymbol{C}_{B}^{T}\boldsymbol{g}\right\rfloor_{\times}\boldsymbol{D}^{-1} & \boldsymbol{K}_{\boldsymbol{d}}^2\boldsymbol{I}_{33} \\ \left({}^{W}\boldsymbol{C}_{B}\boldsymbol{K}_{\boldsymbol{d}}{}^{W}\boldsymbol{C}_{B}^{T\,W}\ddot{\boldsymbol{p}}_{B}\right)^{T} & \boldsymbol{\Pi}_8 & \boldsymbol{\Pi}_9 & \mathbf{0}_{1\times3} \end{bmatrix}, \tag{5.27}$$

where

$$\boldsymbol{\Pi}_8 = 3\left({}^{W}\boldsymbol{C}_{B}^{T\,W}\ddot{\boldsymbol{p}}_{B}\right)^{T} + \left({}^{W}\boldsymbol{C}_{B}^{T\,W}\boldsymbol{r}_1\right)^{T}\boldsymbol{K}_{\boldsymbol{d}}^2 - 3{}^{B}\boldsymbol{v}^{T}\boldsymbol{K}_{\boldsymbol{d}} \tag{5.28}$$

$$\boldsymbol{\Pi}_9 = \left(-3{}^{B}\boldsymbol{v} + \boldsymbol{K}_{\boldsymbol{d}}{}^{W}\boldsymbol{C}_{B}^{T\,W}\boldsymbol{r}_1\right)^{T}\left\lfloor {}^{W}\boldsymbol{C}_{B}^{T}\boldsymbol{g}\right\rfloor_{\times}\boldsymbol{D}^{-1} - \left(\boldsymbol{K}_{\boldsymbol{d}}{}^{W}\boldsymbol{C}_{B}^{T\,W}\ddot{\boldsymbol{p}}_{B}\right)\left\lfloor {}^{W}\boldsymbol{C}_{B}^{T\,W}\boldsymbol{r}_1\right\rfloor_{\times}\boldsymbol{D}^{-1} \tag{5.29}$$

The nonlinear observability matrix for the M-RINS can be constructed using (5.21), (5.23), (5.25) and (5.27) as

$$\boldsymbol{\mathcal{O}}_{\boldsymbol{1RM}} =$$

$$\begin{bmatrix} \mathbf{0}_{3\times3} & -\boldsymbol{K_d} & \mathbf{0}_{3\times3} & \boldsymbol{I_3} \\ \mathbf{0}_{3\times3} & \mathbf{0}_{3\times3} & \left\lfloor {}^{W}\boldsymbol{C}_{B}^{T\,W}\boldsymbol{\mu}\right\rfloor_{\times} \boldsymbol{D}^{-1} & \mathbf{0}_{3\times3} \\ {}^{W}\boldsymbol{r}_1^T & \mathbf{0}_{1\times3} & \mathbf{0}_{1\times3} & \mathbf{0}_{1\times3} \\ \mathbf{0}_{3\times3} & \boldsymbol{K_d^2} & \boldsymbol{K_d}\left\lfloor {}^{W}\boldsymbol{C}_{B}^{T}\boldsymbol{g}\right\rfloor_{\times} \boldsymbol{D}^{-1} & -\boldsymbol{K_d}\boldsymbol{I}_{33} \\ ({}^{W}\boldsymbol{C}_{B}{}^{B}\boldsymbol{v})^T & ({}^{W}\boldsymbol{C}_{B}^{T\,W}\boldsymbol{r}_1)^T & {}^{B}\boldsymbol{v}^T\left\lfloor {}^{W}\boldsymbol{C}_{B}^{T\,W}\boldsymbol{r}_1\right\rfloor_{\times} \boldsymbol{D}^{-1} & \mathbf{0}_{1\times3} \\ \mathbf{0}_{3\times3} & -\boldsymbol{K_d^3} & -\boldsymbol{K_d^2}\left\lfloor {}^{W}\boldsymbol{C}_{B}^{T}\boldsymbol{g}\right\rfloor_{\times} \boldsymbol{D}^{-1} & \boldsymbol{K_d^2}\boldsymbol{I}_{33} \\ {}^{W}\ddot{\boldsymbol{p}}_B^T & 2{}^{B}\boldsymbol{v}^T - ({}^{W}\boldsymbol{C}_{B}^{T\,W}\boldsymbol{r}_1)^T\boldsymbol{K_d} & (-\boldsymbol{K_d}{}^{B}\boldsymbol{v} + b_{az}\grave{\boldsymbol{e}}_{\boldsymbol{3}})^T\left\lfloor {}^{W}\boldsymbol{C}_{B}^{T\,W}\boldsymbol{r}_1\right\rfloor_{\times} \boldsymbol{D}^{-1} & \mathbf{0}_{1\times3} \\ \mathbf{0}_{3\times3} & -\boldsymbol{K_d^3} & -\boldsymbol{K_d^2}\left\lfloor {}^{W}\boldsymbol{C}_{B}^{T}\boldsymbol{g}\right\rfloor_{\times} \boldsymbol{D}^{-1} & \boldsymbol{K_d^2}\boldsymbol{I}_{33} \\ \left({}^{W}\boldsymbol{C}_{B}\boldsymbol{K_d}{}^{W}\boldsymbol{C}_{B}^{T\,W}\ddot{\boldsymbol{p}}_{B}\right)^T & \boldsymbol{\Pi}_8 & \boldsymbol{\Pi}_9 & \mathbf{0}_{1\times3} \end{bmatrix} \tag{5.30}$$

Lemma 5.2. *The M-RINS is locally weakly observable for all the trajectories except when the MAV is stationary, flying towards the range anchor, or MAV flying at a constant velocity.*

Proof. First, let's focus on the third block column of $\boldsymbol{\mathcal{O}}_{\boldsymbol{1RM}}$. Since the earth's magnetic field, ${}^{W}\boldsymbol{\mu}$ and the gravity vector $\boldsymbol{g}$ are not parallel with each other, the matrix $\left[\left(\left\lfloor {}^{W}\boldsymbol{C}_{B}^{T\,W}\boldsymbol{\mu}\right\rfloor_{\times} \boldsymbol{D}^{-1}\right)^T \; \left(\boldsymbol{K_d}\left\lfloor {}^{W}\boldsymbol{C}_{B}^{T}\boldsymbol{g}\right\rfloor_{\times} \boldsymbol{D}^{-1}\right)^T\right]^T$ has full rank of three. Therefore, the third block column has full rank irrespective of the trajectory of the MAV. The first block elements of the second and the fourth block columns ($\boldsymbol{\mathcal{O}}_{\boldsymbol{1RM}_{(1,2)}}$, and $\boldsymbol{\mathcal{O}}_{\boldsymbol{1RM}_{(1,4)}}$) are diagonal matrices. Therefore, each block column has full rank independently. Additionally, the structure of the fourth block row of the observability matrix, $\boldsymbol{\mathcal{O}}_{\boldsymbol{1RM}_{(4,:)}}$ shows that the second and fourth columns are linearly independent. Therefore, the second and the fourth block columns have full rank irrespective of the trajectory.

$\boldsymbol{\mathcal{O}}''_{\boldsymbol{1RM}_{(:,1)}}$ shows the non-zero block elements of the first column

$$\boldsymbol{\mathcal{O}}''_{\boldsymbol{1RM}_{(:,1)}} = \begin{bmatrix} {}^{W}\boldsymbol{r}_1^T \\ ({}^{W}\boldsymbol{C}_B{}^{B}\boldsymbol{v})^T \\ {}^{W}\ddot{\boldsymbol{p}}_B^T \\ \left({}^{W}\boldsymbol{C}_B\boldsymbol{K}_{\boldsymbol{d}}{}^{W}\boldsymbol{C}_B^{T}{}^{W}\ddot{\boldsymbol{p}}_B\right)^T \end{bmatrix}. \tag{5.31}$$

It is straightforward to show that $\boldsymbol{\mathcal{O}}'_{\boldsymbol{1RM}_{(:,1)}}$ loses rank if ${}^{W}\boldsymbol{C}_B{}^{B}\boldsymbol{v} = \mathbf{0}_{1\times3}$, or ${}^{W}\ddot{\boldsymbol{p}}_B = \mathbf{0}_{1\times3}$, or ${}^{W}\boldsymbol{r}_1 \parallel {}^{W}\boldsymbol{C}_B{}^{B}\boldsymbol{v} \parallel {}^{W}\ddot{\boldsymbol{p}}_B$. These conditions correspond to the MAV being stationary, the MAV flying at a constant speed, and the MAV flying toward the range anchor. Therefore, the nonlinear observability matrix has a rank of 12 under a generic trajectory, and the M-RINS is locally weakly observable. □

5.2.4 Unobservable Scenarios

This section presents the unobservable trajectories and the corresponding unobservable directions of the RINS with a single range and magnetometer measurements.

5.2.4.1 Scenario 7: MAV is stationary with a single range measurement

Lemma 5.3. *When the MAV is stationary with a single range and magnetometer measurement, the M-RINS becomes unobservable, and the unobservable sub-space is spanned by*

$${}^{8}\boldsymbol{\mathcal{N}} = \begin{bmatrix} \boldsymbol{n}_1^T & \mathbf{0}_{1\times3} & \mathbf{0}_{1\times3} & \mathbf{0}_{1\times3} \\ \boldsymbol{n}_2^T & \mathbf{0}_{1\times3} & \mathbf{0}_{1\times3} & \mathbf{0}_{1\times3} \end{bmatrix}^T, \tag{5.32}$$

where $\boldsymbol{n}_1, \boldsymbol{n}_2 \in \mathbb{R}^3$*, and* $\boldsymbol{n}_1 \cdot {}^{W}\boldsymbol{r}_1 = \boldsymbol{n}_2 \cdot {}^{W}\boldsymbol{r}_1 = \boldsymbol{n}_1 \cdot \boldsymbol{n}_1 = 0.$

Proof. When the MAV is stationary, the velocity, ${}^{B}\boldsymbol{v}$, and the acceleration of the MAV, ${}^{W}\ddot{\boldsymbol{p}}_{B}$ are zero. As a result, the first block column of $\boldsymbol{\mathcal{O}}_{\boldsymbol{1RM}}$ can be expressed as

$$\boldsymbol{\mathcal{O}}'_{\boldsymbol{1RM}_{(:,1)}} = [\ \mathbf{0}_{3\times6} \quad {}^{W}\boldsymbol{r}_1 \quad \mathbf{0}_{3\times12}\ ]^T \tag{5.33}$$

The rank of $\boldsymbol{\mathcal{O}}'_{\boldsymbol{1RM}_{(:,1)}}$ is one, and the total rank of the observability matrix $\boldsymbol{\mathcal{O}}_{\boldsymbol{1RM}}$ becomes 10. Therefore the M-RINS is unobservable when the MAV is stationary.

Since $\boldsymbol{n}_1$ and $\boldsymbol{n}_2$ are perpendicular to the range vector, it is straightforward to show that $\boldsymbol{\mathcal{O}}_{\boldsymbol{1RM}_{(:,1)}}{}^{8}\boldsymbol{\mathcal{N}}_{(1,:)} = \mathbf{0}_{19\times2}$. This shows that the unobservable sub-space of **Scenario 7** is spanned by ${}^{8}\boldsymbol{\mathcal{N}}$. □

Lemma 5.3 proves that the M-RINS is unobservable when the MAV is stationary. The unobservable directions in (5.32) show that the position of the MAV in any direction perpendicular to the range vector is unobservable under **Scenario 7**.

5.2.4.2 Scenario 8: MAV is flying at a constant velocity with a single range measurement

Lemma 5.4. *When the MAV is flying at a constant velocity, the M-RINS becomes unobservable, and the unobservable sub-space is spanned by*

$${}^{9}\boldsymbol{\mathcal{N}} = \left[({}^{W}\boldsymbol{r}_1 \times {}^{W}\boldsymbol{C}_{B}{}^{B}\boldsymbol{v})^T \quad \mathbf{0}_{1\times3} \quad \mathbf{0}_{1\times3} \quad \mathbf{0}_{1\times3} \right]^T, \tag{5.34}$$

Proof. When the MAV is flying at a constant velocity, the acceleration of the MAV is zero, i.e., ${}^{W}\ddot{\boldsymbol{p}}_{B} = \mathbf{0}_{3\times1}$. Therefore the first column of the observability matrix can be expressed as

$$\boldsymbol{\mathcal{O}}'_{\boldsymbol{1RM}_{(:,1)}} = [\ \mathbf{0}_{3\times6} \quad {}^{W}\boldsymbol{r}_1 \quad {}^{W}\boldsymbol{C}_{B}{}^{B}\boldsymbol{v} \quad \mathbf{0}_{3\times9}\ ]^T. \tag{5.35}$$

Since there are only two non-zero rows in $\boldsymbol{\mathcal{O}}'_{\mathbf{1}\boldsymbol{RM}_{(:,1)}}$, the rank becomes two[3], and the rank of $\boldsymbol{\mathcal{O}}_{\mathbf{1}\boldsymbol{RM}}$ becomes 11. Therefore the M-RINS is unobservable when the MAV is flying at a constant velocity.

Since ${}^{W}\boldsymbol{r}_1 \times {}^{W}\boldsymbol{C}_{B}{}^{B}\boldsymbol{v}$ is the perpendicular direction to both ${}^{W}\boldsymbol{r}_1$, and ${}^{W}\boldsymbol{C}_{B}{}^{B}\boldsymbol{v}$, it is straightforward to show that $\boldsymbol{\mathcal{O}}_{\mathbf{1}\boldsymbol{RM}_{(:,1)}}({}^{W}\boldsymbol{r}_1 \times {}^{W}\boldsymbol{C}_{B}{}^{B}\boldsymbol{v}) = \mathbf{0}_{19\times1}$. This shows that the unobservable sub-space of **Scenario 8** is spanned by ${}^{9}\boldsymbol{\mathcal{N}}$. $\square$

The null vector ${}^{9}\boldsymbol{\mathcal{N}}$ shows that position in the perpendicular direction to both range and velocity vectors is unobservable under **Scenario 8**.

5.2.4.3 Scenario 9: MAV is flying towards the range anchor with a single range measurement

Lemma 5.5. *When the MAV is flying towards the range anchor, the M-RINS becomes unobservable, and the unobservable direction sub-space is spanned by*

$$ {}^{10}\boldsymbol{\mathcal{N}} = \left[\left({}^{W}\boldsymbol{r}_1 \times {}^{W}\boldsymbol{C}_{B}\boldsymbol{K}_{\boldsymbol{d}}{}^{W}\boldsymbol{C}_{B}^{T}{}^{W}\ddot{\boldsymbol{p}}_{B} \right)^{T} \quad \mathbf{0}_{1\times3} \quad \mathbf{0}_{1\times3} \quad \mathbf{0}_{1\times3} \right]^{T}, \tag{5.36} $$

Proof. When the MAV is flying towards the single range anchor, the velocity and the acceleration of the MAV are parallel to the range vector. This can be expressed as

$$ {}^{W}\boldsymbol{C}_{B}{}^{B}\boldsymbol{v} = \alpha{}^{W}\boldsymbol{r}_1, \qquad {}^{W}\ddot{\boldsymbol{p}}_{B} = \beta^{W}\boldsymbol{r}_1. \tag{5.37} $$

Under these conditions, the rank of the first block column shown in (5.31) loses a rank. The total rank of the observability matrix becomes 11, and therefore the M-RINS is unobservable when the MAV is flying towards the range anchor.

---

[3] The rank of $\boldsymbol{\mathcal{O}}'_{\mathbf{1}\boldsymbol{RM}_{(:,1)}}$ will become one if ${}^{W}\boldsymbol{r}_1 \parallel {}^{W}\boldsymbol{C}_{B}{}^{B}\boldsymbol{v}$, and this condition is discussed in **Scenario 9**

Since ${}^{10}\boldsymbol{\mathcal{N}}_{(1,1)}$ represents a perpendicular vector to ${}^{W}\boldsymbol{r}_1$, and ${}^{W}\boldsymbol{C}_{B}\boldsymbol{K}_{\boldsymbol{d}}{}^{W}\boldsymbol{C}_{B}^{T\,W}\ddot{\boldsymbol{p}}_{B}$ it is straightforward to show that $\boldsymbol{\mathcal{O}}_{\boldsymbol{1RM}_{(:,1)}}{}^{10}\boldsymbol{\mathcal{N}}_{(1,1)} = \boldsymbol{0}_{19\times 1}$. $\square$

If the MAV is flying towards the range anchor at a constant velocity, the range vector, and the MAV velocity are parallel, i.e., ${}^{W}\boldsymbol{r}_1 \parallel {}^{W}\boldsymbol{C}_{B}{}^{B}\boldsymbol{v}$. Under these conditions, the unobservable directions would be the position perpendicular to the range vector.

A summary of the observability analysis of M-RINS is given in Table 5.2.

Table 5.2: Summary of the observability analysis of M-RINS

Case	**Scenario**	**Unobservable Directions**
Single range and heading measurements	**Scenario 7:** Hovering	• Position perpendicular to the range vector
	Scenario 8: Flying at a constant velocity	• Position in the perpendicular direction to both velocity and range vector
	Scenario 9: Flying towards the range anchor	• Position along $\left({}^{W}\boldsymbol{r}_1 \times {}^{W}\boldsymbol{C}_{B}\boldsymbol{K}_{\boldsymbol{d}}{}^{W}\boldsymbol{C}_{B}^{T\,W}\ddot{\boldsymbol{p}}_{B}\right)$

5.2.5 Simulation Results

The M-RINS implementation follows the EKF implementation of the three and two range assisted RINS presented in Section 4.1.2. The M-RINS implementation includes the gyroscope bias in the EKF mechanization equations.

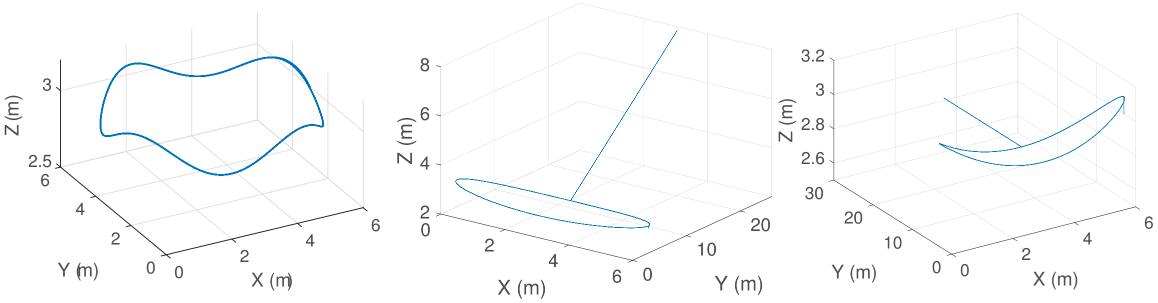

(a) (b) (c)

Fig. 5.4: Trajectories used in the simulations of single range and heading assisted INS. (a) Observable Circular with varying altitude, (b) Trajectory used in **Scenario 8** (c) Trajectory used in **Scenario 9**

First, five simulations are performed, in which the MAV is flown in the observable circular trajectory shown in Fig 5.4a. For each simulation, the range anchor location is selected randomly, and the five locations are given in Table 5.3 (Fig. 5.5). Fig 5.6 clearly shows that the total angle and position estimation errors are bounded and are well within the 3σ boundary for all the five simulations. This shows when the MAV is flying in an observable trajectory, the M-RINS is able to estimate the pose of the MAV, irrespective of the anchor position.

Table 5.3: Location of the single range anchor used for M-RINS

	Location (m)
Simulation 1	(4.7, 8.2, 1.9)
Simulation 2	(1.3, 0.2, 9.2)
Simulation 3	(8.6, 2.5, 4.4)
Simulation 4	(6.3, 8.1, 1.7)
Simulation 5	(9.0, 1.9, 6.8)

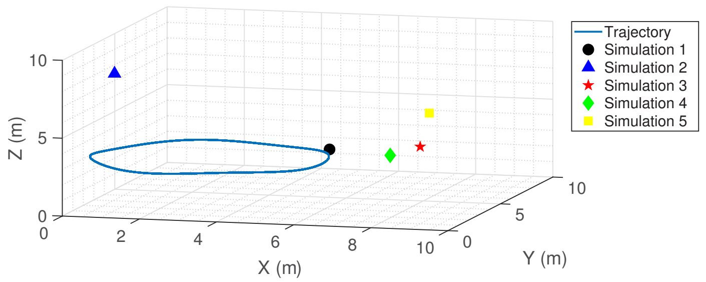

Fig. 5.5: Locations of the single range anchor used in the five simulations of M-RINS

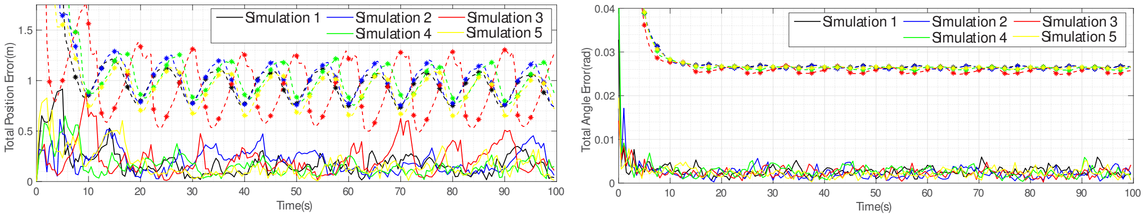

(a) (b)

Fig. 5.6: RINS with a single range and heading measurements with five different anchor locations. (a) Total Position error and the 3σ boundary, (b) Total Angle Error and the 3σ boundary. (—) Error, (-$*$-) 3σ boundary.

Next, 25 Monte-Carlo simulations were conducted using the same trajectory and the anchor location as Simulation 1 in Table 3.2. The MAE of the estimated states and the 3σ boundaries are shown in Fig. 5.7. As explained in Section 5.2.1, including the gyroscope bias does not affect the observability of the M-RINS. This is evident in Fig. 5.7 where all the state estimation errors, including the gyroscope bias errors (Fig. 5.7d) are bounded and well within the 3σ confidence interval.

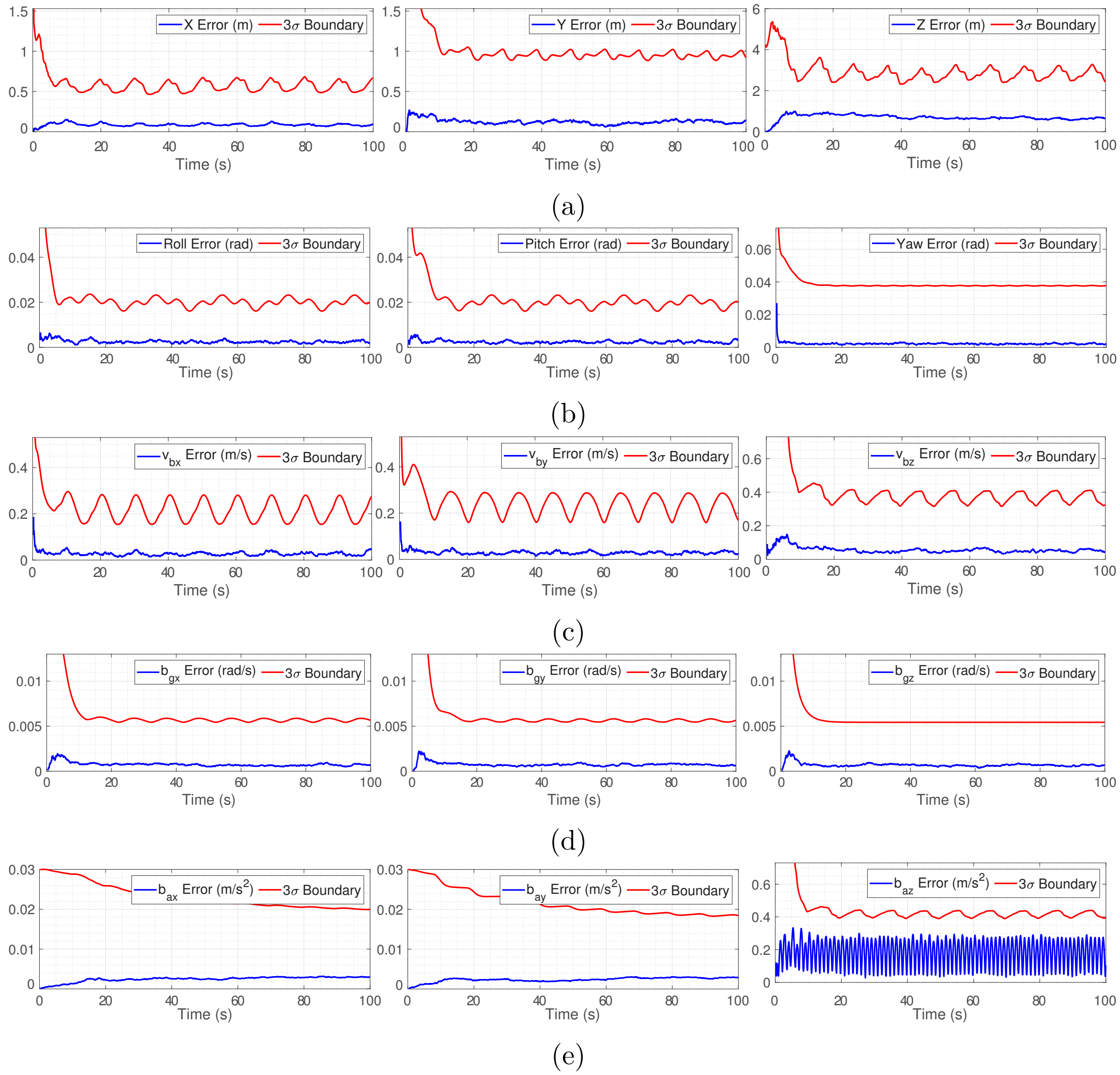

(a)

(b)

(c)

(d)

(e)

Fig. 5.7: Simulation 1, 25 Monte-Carlo simulations: MAE and 3σ boundary (a) Position, (b) Orientation, (c) Body frame velocity, (d) Gyroscope bias, (e) Accelerometer bias.

5.2.5.1 Unobservable Scenarios

Similar to simulations conducted in section 3.4, the simulated trajectories have two parts, the first segment (0 - 50s) of the trajectory is the observable, height varying circular trajectory, and the second segment (50s - 100s) is the unobservable trajectory. The anchor locations are selected such that during unobservable trajectories, the unobservable directions coincide with the main axes of $\{W\}$. The simulation results show the MAE of the estimates of 25 Monte-Carlo simulations and the average of 3σ confidence boundary.

For **Scenario 7**, the MAV is kept stationary at (3, 0, 3.1) m, and the range anchor is placed at (3, 0, 9) m. In this simulation, the range vector is vertical and based on the observability analysis of the **Scenario 7** (Lemma 5.3), position perpendicular to the range vector, i.e. along the $x - y$ plane is unobservable.

Fig 5.8 shows the x and y estimation errors, and the estimation covariances diverge rapidly in the first few seconds. As time progress, the range vector based on the estimated states does not lie parallel to the z axis due to the estimation errors. Therefore the plane perpendicular to the estimated range vector is no longer parallel to the $x - y$ plane. This can be seen clearly in Fig 5.8, where the z estimation error and covariance start to diverge during the latter portion of the trajectory.

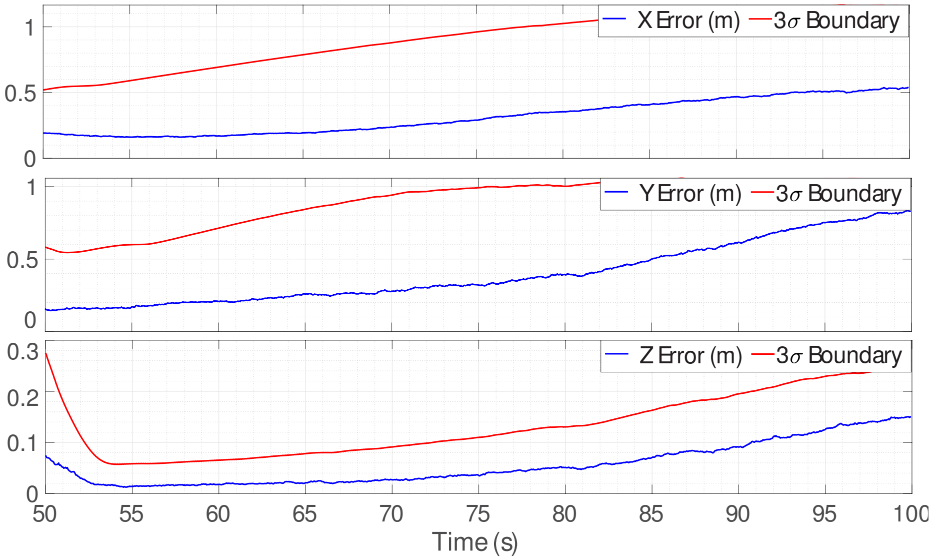

Fig. 5.8: **Scenario 7**: Position estimation error and the 3σ boundary

The MAV is flown on the trajectory shown in Fig 5.4b for the **Scenario 8**. During the second portion of the trajectory, the MAV moves in a straight line on the $y-z$ plane at a constant velocity. The range anchor is placed at (3, -1, 9), such that the range and the velocity vectors lie on the $y-z$ plane. Lemma 5.4 shows that the unobservable direction is perpendicular to both the range and the velocity vectors under **Scenario 8**. Based on the trajectory and the beacon location, x is the unobservable direction. Fig. 5.9 clearly shows the divergence of the x position estimate covariance. Similar to the results of **Scenario 7**, there is a slight increase in the z error and the covariance during the latter part of the trajectory.

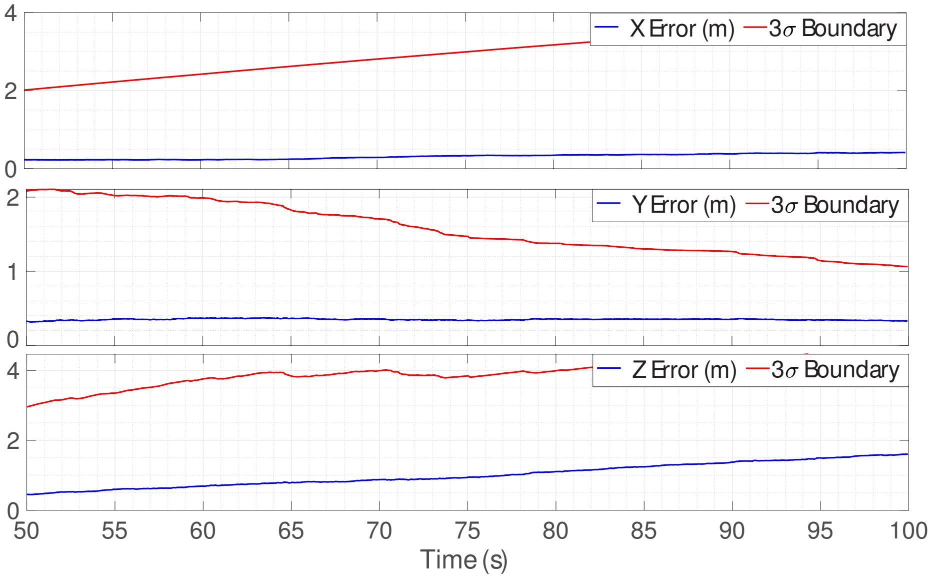

Fig. 5.9: **Scenario 8**: Position estimation error and the 3σ boundary

The trajectory shown in Fig. 5.4c is used to visualize the unobservable directions under **Scenario 9**. The straight line portion of the trajectory is horizontal, and the MAV moves at constant acceleration towards the beacon at (3, 40, 2.9) m. The unobservable directions of the **Scenario 9** are given in (5.35). The drag coefficient matrix $\boldsymbol{K_d}$ has the structure shown in (3.29), and therefore, the x, y components of ${}^{W}\boldsymbol{C}_{B}\boldsymbol{K_d}{}^{W}\boldsymbol{C}_{B}^{T}{}^{W}\ddot{\boldsymbol{p}}_{B}$ are in the same direction as ${}^{W}\ddot{\boldsymbol{p}}_{B}$, the only difference is in the z component. Therefore, during the unobservable trajectory ${}^{W}\boldsymbol{r}_{1} \times {}^{W}\boldsymbol{C}_{B}\boldsymbol{K_d}{}^{W}\boldsymbol{C}_{B}^{T}{}^{W}\ddot{\boldsymbol{p}}_{B}$ is parallel to x axis. Fig. 5.10 clearly shows a significant increase in the covariance of the x estimate. Additionally, there is a slight increase in the y, and z estimate covariances due to the estimation errors.

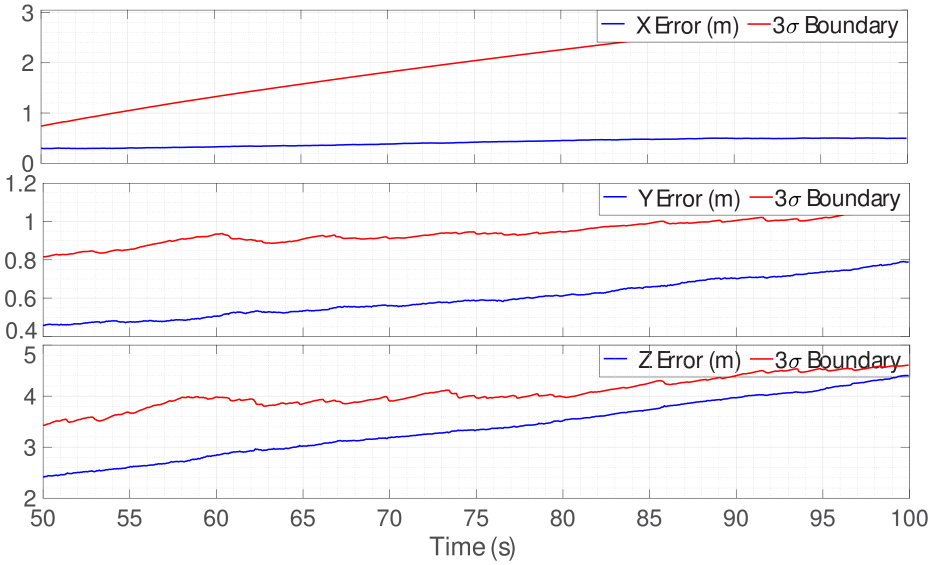

Fig. 5.10: **Scenario 9**: Position estimation error and the 3σ boundary

5.3 Summary

This chapter presented a design of a single range assisted inertial navigation system. A detailed observability analysis showed that the RINS with only a single range measurement is unobservable for any trajectory. The second INS proposed in this chapter, M-RINS is locally weakly observable for a generic trajectory, and it incorporates magnetometer measurements in addition to the single range measurement. An observability study was carried out on the proposed M-RINS, and identified three special trajectories that render the M-RINS unobservable and the corresponding unobservable directions. All of these findings were validated through numerical simulations.

Chapter 6

Conclusion and Outlook

This chapter summarizes the main contributions achieved in this thesis and discusses several future research directions. The main issue this thesis attempts to address is the localization problem of multi-rotor MAVs in indoor environments using a computationally efficient, robust, and easy to deploy technique. The research study conducted an extensive literature review on the existing and the state of the art indoor localization techniques used in MAV applications. The outcome of the literature review indicated that range assisted inertial navigation systems do satisfy the criterion this study prefers in a localization technique. However, to the author's knowledge, there are no studies on RINS that utilize less than four range measurements and no other types of sensors. In order to address the lack of knowledge, this research was conducted to achieve three primary objectives:

1. Development of tree and two range assisted INS for multi-rotor MAVs,
2. Development of trajectory dependent observability constrained RINS with three and two range measurements,
3. Development of a single range assisted INS for multi-rotor MAVs,

Research contributions related to each objective are summarized in the following sections.

6.1 Research Summary Based on Objective1

The first objective of this research focused on developing a range assisted inertial navigation system that can localize the multi-rotor MAV with three or two range measurements to known locations. The design of the RINS incorporated the unique aerodynamic forces, specifically the blade flapping drag force acting on the MAV. This enabled the RINS to function without having to use a velocity sensor. A nonlinear observability analysis was conducted to identify the observability properties of the proposed RINS. The analysis was carried out for two cases, *Case 1*: with three range measurements, and *Case 2*: with two range measurements. The analysis showed that the proposed RINS is locally weakly observable for a generic trajectory under both cases. However, three scenarios (trajectories) were identified for each case that renders the proposed RINS unobservable. The identified scenarios are not exhaustive, but they are the most practical scenarios that a MAV will experience in a typical operating condition. The other plausible unobservable conditions can be found using the analytical expressions of observability matrices derived in section 3.3. However, the MAV will remain in the unobservable mode momentarily and, therefore, will not affect the overall performance of the simulator. One such scenario is when the MAV moves in a straight line. The gyroscope bias will be unobservable if the gyroscope bias vector is parallel to the body frame velocity of the MAV. By nature, the gyroscope bias has characteristics of a random walk process. Therefore the bias vector will not remain parallel to the body frame velocity for a considerable time period. The performance of the proposed RINS was evaluated numerically as well as experimentally for observable trajectories, and the experimental results showed that the RINS is capable of estimating the pose of the MAV with reasonable accuracy. Additionally, unobservable directions of the unobservable scenarios were determined and numerically validated. These unobservable directions will be used for the fulfillment of Objective 2.

6.2 Research Summary Based on Objective 2

An estimator implemented on an unobservable system can gain spurious information along the unobservable directions and can impact the consistency and the accuracy of the estimation. Therefore, the second objective focused on analyzing and improving the consistency of the three and two range assisted INS during the unobservable scenarios identified under objective 1. First, the unobservable directions identified were verified using the unobservable transformations corresponding to the unobservable directions. The outcome of this verification showed that not all the unobservable directions identified through the Lie derivative based observability analysis are truly unobservable. Lie derivative based analysis is a good starting point to determine the unobservable direction but should be verified using unobservable transformations corresponding to the unobservable directions. Then it was shown that the linearized model used for the EKF implementation does not have the same unobservable directions as the nonlinear system during the unobservable scenarios. Finally, consistency rules for the filter were determined for each unobservable trajectory and applied in the observability constrained RINS. These rules ensure the linearized system has the same observability properties as the nonlinear system and prevent the filter from updating along the unobservable directions. The simulation results show significant improvement in the consistency of the estimator after applying the observability constraints. Additionally, the estimation accuracy has improved compared to the EKF implementation without observability constraints. When the consistency of the estimator is improved, the states are estimated with proper confidence levels. Therefore proper decisions can be made based on the more accurate state estimates and the corresponding covariances.

6.3 Research Summary Based on Objective 3

The third objective focuses on developing a RINS with a single range measurement, and the research study presents two RINS designs to fulfill the objective. The first RINS developed used just a single range measurement, and the observability study on the RINS showed that the RINS is unobservable for all the trajectories. The unobservable direction includes the position in the perpendicular direction to the range and the gravity vector. The second RINS design was developed to overcome the observability limitation of the previous design. The M-RINS incorporated a magnetometer measurement in addition to the single range measurement. The observability analysis on the M-RINS showed that the system is locally weakly observable for a generic trajectory. Additionally, three unobservable trajectories were identified that render the M-RINS unobservable. Numerical results showed that the developed M-RINS is able to estimate the pose of the MAV with reasonable accuracy and validated the unobservable directions identified in the observability analysis.

6.4 Contributions

To summarize, this thesis made the following contributions in range assisted localization for multi-rotor micro aerial vehicles in indoor environments, fulfilling all of the outlined research objectives.

1. **Contributions related to Objective 1.**
    - (a) Design of a RINS for MAV, which is capable of estimating with three or two range measurements.
    - (b) An observability analysis to determine the overall observability, unobservable trajectories, and unobservable directions of the RINS.
    - (c) Experimental and numerical validation of the RINS with three and two range measurements.
2. **Contributions related to Objective 2.**
    - (a) Consistency analysis of the EKF implementation of the RINS under unobservable trajectories.
    - (b) Development of trajectory dependent observability constrained RINS.
3. **Contributions related to Objective 3.**
    - (a) Design and observability study on RINS for MAVs using a single range measurement.
    - (b) Design of a RINS for MAVs using heading and single range measurement.
    - (c) Observability analysis and unobservable mode identification of M-RINS.

6.4.1 List of Publications

This research led to the following scientific articles and publications:

- Erange Fernando, Oscar De Silva, George K. Mann, and Raymond Gosine, Trajectory Dependent Consistency Improvement of Two/Three Range Assisted INS for Micro Aerial Vehicles", Journal of Intelligent & Robotic Systems, 2022 (Submitted and under review).

- Erange Fernando, Oscar De Silva, George K. Mann, and Raymond Gosine, "Towards Developing an Indoor Localization System for MAVs using Two or Three RF Range Anchors: An Observability Based Approach", IEEE Sensors Journal, vol 22, no 6, pp.5173 - 5187,2022.

- Eranga Fernando, Oscar De Silva, George K. Mann, and Raymond Gosine, "Observability Analysis of Position Estimation for Quadrotors With Modified Dynamics and Range Measurements", 2019 IEEE/RSJ International Conference on Intelligent Robots and Systems (IROS), 2019, pp. 2783-2788.

- Eranga Fernando, George K. Mann, Oscar De Silva, and Raymond Gosine. Gosine,"Range Assisted Inertial Navigation System for QuadrotorLocalization: Observability Analysis and Experimental Validation", 28th Annual Newfoundland Electrical and Computer Engineering Conference (NECEC), Nov. 2019.

- Eranga Fernando, George K. Mann, Oscar De Silva and Raymond Gosine, "Design and analysis of a pose estimator for quadrotor MAVs with modified dynamics and range measurements", ASME 2017 Dynamic Systems and Control Conference.

6.5 Future Research Directions

The research work presented in this thesis has a number of potential extensions. These future developments aim at improving the practicality of the developed RINS in real-world applications.

Incorporating additional sensor inputs: One of the main goals of this study was to utilize the least number of sensor measurements to develop a functional RINS for MAVs. Towards achieving this goal, this study utilized IMU, range, and magnetometer (only for M-RINS) measurements. However, additional sensors can be incorporated to improve the performance of the RINS. One example would be the propeller speed sensor which is generally integrated into the electronic speed controllers of the MAV. Having propeller speed information allows the RINS to accurately model the drag force effects and decouple the thrust and accelerometer bias.

Wind disturbance estimation: A key assumption made in this study is the no wind conditions. Even though the no wind assumption is valid for most indoor environments, there can be instances where this assumption is violated. Studies have shown that the drag force model-based INS performance can degrade under windy conditions. Therefore it is important to estimate the wind disturbances for robust operation [103]. It will be interesting to investigate how capable the RINS with fewer range measurements is in estimating the wind disturbances. Based on the investigation, additional sensors can be incorporated to overcome any limitations. Accurate disturbance estimation can extend the use of the RINS into outdoor environments where the wind is unavoidable.

RINS integration with VINS: VINS has become the go-to localization system for MAVs. However, VINS suffer from drift of the estimates over a long period of time due to error accumulation. Loop closure and global pose graph optimization are two widely used techniques to mitigate the drift at the cost of computational resources. Since the RINS require less computational overhead and provide the global position estimates, RINS can be used to reduce the drift in the VINS estimates. Further research can be conducted on the adaptive sensor fusion of VINS and RINS. This will enable the switching between VINS and RINS depending on the trajectory, external disturbances, measurement noise, etc. Since vision and range sensors complement each other, adaptive sensor fusion can also be developed as a fault tolerance system for MAV localization.

Appendix A

Rotation about vector $\boldsymbol{a}$

Assume that the current orientation of the MAV is given by the Gibbs vector $\boldsymbol{\rho}$, and the vector ${}^{B}\boldsymbol{a}$ is expressed in the body frame of the MAV, $\{B\}$. Then the MAV is rotated about the vector ${}^{B}\boldsymbol{a}$ by an angle of θ. This rotation can be represented using Gibbs vector as

$$\boldsymbol{\varrho} = \frac{{}^{B}\boldsymbol{a}}{\|{}^{B}\boldsymbol{a}\|}\tan\left(\frac{\theta}{2}\right) \tag{A.1}$$

Since any rotation of any vector about itself gives the same vector, it is trivial to show that

$$\boldsymbol{C}(\boldsymbol{\rho}\oplus\boldsymbol{\varrho})^{B}\boldsymbol{a} = \boldsymbol{C}(\boldsymbol{\rho})^{B}\boldsymbol{a}, \tag{A.2}$$

where, $\boldsymbol{\rho}\oplus\boldsymbol{\varrho}$ is the composition of two Gibbs vectors, $\boldsymbol{\rho}$, and $\boldsymbol{\varrho}$. The composition operator $\oplus$ is defined as [84]

$$\boldsymbol{\rho}\oplus\boldsymbol{\varrho} = \frac{\boldsymbol{\rho}+\boldsymbol{\varrho}-\boldsymbol{\varrho}\times\boldsymbol{\rho}}{1-\boldsymbol{\varrho}^{T}\boldsymbol{\rho}}. \tag{A.3}$$

(A.3) can be simplified as

$$\boldsymbol{\rho}\oplus\boldsymbol{\varrho} = \frac{\boldsymbol{\rho}+\boldsymbol{\varrho}-\boldsymbol{\varrho}\times\boldsymbol{\rho}}{1-\boldsymbol{\varrho}^{T}\boldsymbol{\rho}}$$

$$
\begin{aligned}
&= \frac{\boldsymbol{\rho} + \left(\boldsymbol{I_3} + \lfloor \boldsymbol{\rho} \rfloor_\times\right) \boldsymbol{\varrho} + \boldsymbol{\rho}\boldsymbol{\rho}^T \boldsymbol{\varrho} - \boldsymbol{\rho}\boldsymbol{\rho}^T \boldsymbol{\varrho}}{1 - \boldsymbol{\varrho}^T \boldsymbol{\rho}} \\
&= \frac{\left(\boldsymbol{\rho} - \boldsymbol{\rho}\boldsymbol{\rho}^T \boldsymbol{\varrho}\right) + \left(\boldsymbol{I_3} + \lfloor \boldsymbol{\rho} \rfloor_\times + \boldsymbol{\rho}\boldsymbol{\rho}^T\right) \boldsymbol{\varrho}}{1 - \boldsymbol{\varrho}^T \boldsymbol{\rho}} \\
&= \frac{\boldsymbol{\rho}\left(1 - \boldsymbol{\varrho}^T \boldsymbol{\rho}\right) + \boldsymbol{D}\boldsymbol{\varrho}}{1 - \boldsymbol{\varrho}^T \boldsymbol{\rho}}
\end{aligned}
$$

$$
\boldsymbol{\rho} \oplus \boldsymbol{\varrho} = \boldsymbol{\rho} + \lambda \boldsymbol{D}\boldsymbol{\varrho}, \qquad \lambda = \frac{1}{1 - \boldsymbol{\varrho}^T \boldsymbol{\rho}} \in \mathbb{R}. \tag{A.4}
$$

(A.4) shows that the composition of two Gibbs vectors can be expressed as an algebraic sum, and $\lambda^* \boldsymbol{D}\,{}^B\boldsymbol{a}$ represents the rotation about the vector ${}^B\boldsymbol{a}$, where $\lambda^* = \dfrac{\tan(\theta/2)}{\|{}^B\boldsymbol{a}\|\left(1 - \boldsymbol{\varrho}^T \boldsymbol{\rho}\right)}$.

Appendix B

Output Function and its Derivatives

The output function of the RINS with three and two range measurements comprise of the accelerometer measurements and the range measurements between the MAV and the anchors. During the observability analysis, we define the output function $\mathbf{h}(\mathbf{x})$ as

$$\mathbf{y} = \mathbf{h}(\mathbf{x}) = \begin{bmatrix} \mathbf{h}_a(\mathbf{x}) \\ \mathbf{h}_r(\mathbf{x}) \end{bmatrix}, \qquad \mathbf{h}_r(\mathbf{x}) = \begin{bmatrix} \mathbf{h}_1(\mathbf{x}) \\ \vdots \\ \mathbf{h}_j(\mathbf{x}) \end{bmatrix}. \tag{B.1}$$

$\mathbf{h}_a(\mathbf{x})$ denotes the accelerometer measurements defined as

$$\mathbf{h}_a(\mathbf{x}) = -\boldsymbol{K_d}{}^{B}\boldsymbol{v} + {}^{B}\boldsymbol{b}_a. \tag{B.2}$$

The n^{th} order time derivatives of $h_1(\mathbf{x})$ can be calculated as

$$\mathbf{h}_a^{(n)}(\mathbf{x}) = -\boldsymbol{K_d}{}^{B}\boldsymbol{v}^{(n)}. \tag{B.3}$$

First and the second order derivatives of ${}^{B}\boldsymbol{v}$ can be expressed as

$$ {}^{B}\boldsymbol{v}^{(1)} = \lfloor {}^{B}\boldsymbol{v} \rfloor_{\times} \left({}^{B}\boldsymbol{\omega}_{m} - {}^{B}\boldsymbol{b}_{g} \right) - \boldsymbol{K_{d}}{}^{B}\boldsymbol{v} + b_{az}\grave{\boldsymbol{e}}_{\mathbf{3}} - {}^{W}\boldsymbol{C}_{B}^{T}\boldsymbol{g} \tag{B.4} $$

$$ {}^{B}\boldsymbol{v}^{(2)} = \lfloor {}^{B}\boldsymbol{v} \rfloor_{\times} {}^{B}\boldsymbol{\omega}_{m}^{(1)} - \lfloor {}^{B}\boldsymbol{\omega}_{m} - {}^{B}\boldsymbol{b}_{g} \rfloor_{\times} {}^{B}\boldsymbol{v}^{(1)} - \boldsymbol{K_{d}}{}^{B}\boldsymbol{v}^{(1)} - {}^{W}\boldsymbol{C}_{B}^{(1)T}\boldsymbol{g}. \tag{B.5} $$

Third and higher order terms of ${}^{B}\boldsymbol{v}$ depends on ${}^{B}\boldsymbol{v}, {}^{B}\boldsymbol{\omega}_{m}, {}^{B}\boldsymbol{b}_{g}, {}^{W}\boldsymbol{C}_{B}^{(3)}$ and their higher order terms.

Since the range measurement to the j^{th} anchor, r_j and it's square are strictly positive and have one-to-one correspondence, we chose the following definition instead of r_j for the consistency analysis.

$$ \mathbf{h}_{i}(\mathbf{x}) = \frac{1}{2}r_{i}^{2} = \frac{1}{2}{}^{W}\boldsymbol{r}_{i}^{T}{}^{W}\boldsymbol{r}_{j}. \tag{B.6} $$

The n^{th} order derivative of $\mathbf{h}_j(\mathbf{x})$ can be expressed as a function of ${}^{W}\boldsymbol{r}_j$ and it's derivatives up to n^{th} order as

$$ \mathbf{h}_{j}^{(n)}(\mathbf{x}) = g(\boldsymbol{r}_{j}, ..., \boldsymbol{r}_{j}^{(n)}). \tag{B.7} $$

Appendix C

Observability Analysis of Single Range Assisted INS

Nonlinear Observability Matrix Calculation

Control affine form of the single range assisted INS and the measurement model are expressed as

$$\begin{bmatrix} {}^{W}\dot{\boldsymbol{p}}_{B} \\ {}^{W}\dot{\boldsymbol{q}}_{B} \\ {}^{B}\dot{\boldsymbol{v}} \\ {}^{B}\dot{\boldsymbol{b}}_{g} \\ {}^{B}\dot{\boldsymbol{b}}_{a} \end{bmatrix} = \begin{bmatrix} {}^{W}\boldsymbol{C}_{B}{}^{B}\boldsymbol{v} \\ \frac{1}{2}\boldsymbol{\Xi}(\boldsymbol{q})\left[0 \ ({}^{B}\boldsymbol{\omega}_{m} - {}^{B}\boldsymbol{b}_{g} - \boldsymbol{\eta}_{\omega})^{T}\right]^{T} \\ \lfloor {}^{B}\boldsymbol{v} \rfloor_{\times}\left({}^{B}\boldsymbol{\omega}_{m} - {}^{B}\boldsymbol{b}_{g} - \boldsymbol{\eta}_{\omega}\right) - \boldsymbol{K_{d}}{}^{B}\boldsymbol{v} + b_{az}\grave{\boldsymbol{e}}_{\boldsymbol{3}} - {}^{W}\boldsymbol{C}_{B}^{T}\boldsymbol{g} \\ \boldsymbol{\eta_{gb}} \\ \boldsymbol{\eta_{ab}} \end{bmatrix}. \tag{C.1}$$

$$\mathbf{y} = \begin{bmatrix} \mathbf{h}_{a}(\mathbf{x}) \\ \mathbf{h}_{r}(\mathbf{x}) \end{bmatrix} = \begin{bmatrix} -\boldsymbol{K_{d}}{}^{B}\boldsymbol{v} + {}^{B}\boldsymbol{b}_{a} + \boldsymbol{\eta_{a}} \\ r_{1} + \eta_{r1} \end{bmatrix}. \tag{C.2}$$

The zeroth order Lie derivatives of the measurement function can be expressed as

$$\mathfrak{L}^0\mathbf{h} = \mathbf{h}(\mathbf{x}). \tag{C.3}$$

Gradient of $\mathfrak{L}^0\mathbf{h}$ with respect to the state vector can be calculated as

$$\nabla\mathfrak{L}^0\mathbf{h} = \begin{bmatrix} \mathbf{0}_{3\times3} & -\boldsymbol{K_d} & \mathbf{0}_{3\times3} & \mathbf{0}_{3\times3} & \boldsymbol{I_3} \\ {}^{W}\boldsymbol{r}_1^T & \mathbf{0}_{1\times3} & \mathbf{0}_{1\times3} & \mathbf{0}_{1\times3} & \mathbf{0}_{1\times3} \end{bmatrix}. \tag{C.4}$$

The first order Lie derivative with respect to $\mathbf{f_0}$ can be calculated as

$$\mathfrak{L}^1_{\mathbf{f_0}}\mathbf{h} = \nabla\mathfrak{L}^0\mathbf{h}\cdot\mathbf{f_0} = \begin{bmatrix} \boldsymbol{K_d}{}^{B}\dot{\boldsymbol{v}}' \\ {}^{W}\boldsymbol{r}_1^{T\,W}\boldsymbol{C}_{B}{}^{B}\boldsymbol{v} \end{bmatrix}, \tag{C.5}$$

where

$${}^{B}\dot{\boldsymbol{v}}' = -\left\lfloor {}^{B}\boldsymbol{v} \right\rfloor_{\times} {}^{B}\boldsymbol{b}_g - \boldsymbol{K_d}{}^{B}\boldsymbol{v} + b_{az}\grave{\mathbf{e}}_{\mathbf{3}} - {}^{W}\boldsymbol{C}_{B}^{T}\boldsymbol{g}. \tag{C.6}$$

The span of the $\mathfrak{L}^1_{\mathbf{f_0}}\mathbf{h}$ can be calculated as

$$\nabla\mathfrak{L}^1_{\mathbf{f_0}}\mathbf{h} = \begin{bmatrix} \mathbf{0}_{3\times3} & \boldsymbol{K_d}\left(\boldsymbol{K_d} - \left\lfloor {}^{B}\boldsymbol{b}_g \right\rfloor_{\times}\right) & \boldsymbol{K_d}\left\lfloor {}^{W}\boldsymbol{C}_{B}^{T}\boldsymbol{g} \right\rfloor_{\times}\boldsymbol{D}^{-1} & \boldsymbol{K_d}\left\lfloor {}^{B}\boldsymbol{v} \right\rfloor_{\times} & \boldsymbol{K_d}\boldsymbol{I}_{33} \\ ({}^{W}\boldsymbol{C}_{B}{}^{B}\boldsymbol{v})^T & {}^{W}\boldsymbol{r}_1^{T\,W}\boldsymbol{C}_{B} & -{}^{W}\boldsymbol{r}_1^{T}\left\lfloor {}^{W}\boldsymbol{C}_{B}{}^{B}\boldsymbol{v} \right\rfloor_{\times}\left(\boldsymbol{D}^{T}\right)^{-1} & \mathbf{0}_{1\times3} & \mathbf{0}_{1\times3} \end{bmatrix}. \tag{C.7}$$

The second order Lie derivative of $\mathfrak{L}^1_{\mathbf{f_0}}\mathbf{h}$ with respect to $\mathbf{f_0}$ and it's gradient can be expressed as

$$\mathfrak{L}^2_{\mathbf{f_0}\mathbf{f_0}}\mathbf{h} = \nabla\mathfrak{L}^1_{\mathbf{f_0}}\mathbf{h}\cdot\mathbf{f_0} = \begin{bmatrix} \left(\boldsymbol{K}_{\boldsymbol{d}}^2 - \boldsymbol{K}_{\boldsymbol{d}}\left\lfloor {}^{B}\boldsymbol{b}_g\right\rfloor_\times\right){}^{B}\dot{\boldsymbol{v}} - \boldsymbol{K}_{\boldsymbol{d}}\left\lfloor {}^{W}\boldsymbol{C}_{B}^{T}\boldsymbol{g}\right\rfloor_\times {}^{B}\boldsymbol{b}_g \\ {}^{B}\boldsymbol{v}^{T\,B}\boldsymbol{v} + {}^{W}\boldsymbol{r}_1^{T\,W}\boldsymbol{C}_{B}{}^{B}\dot{\boldsymbol{v}}' + {}^{W}\boldsymbol{r}_1^{T\,W}\boldsymbol{C}_{B}\left\lfloor {}^{B}\boldsymbol{v}\right\rfloor_\times {}^{B}\boldsymbol{b}_g \end{bmatrix}, \tag{C.8}$$

$$\nabla\mathfrak{L}^2_{\mathbf{f_0}\mathbf{f_0}}\mathbf{h} = \begin{bmatrix} \mathbf{0}_{3\times3} & -\boldsymbol{K}_{\boldsymbol{d}}\left(\boldsymbol{K}_{\boldsymbol{d}} - \left\lfloor {}^{B}\boldsymbol{b}_g\right\rfloor_\times\right)^2 & \boldsymbol{\Theta} & \boldsymbol{\Phi} & \boldsymbol{K}_{\boldsymbol{d}}\left(\boldsymbol{K}_{\boldsymbol{d}} - \left\lfloor {}^{B}\boldsymbol{b}_g\right\rfloor_\times\right)\boldsymbol{I}_{33} \\ {}^{W}\ddot{\boldsymbol{p}}_{B}^{T} & 2{}^{B}\boldsymbol{v}^{T} - {}^{W}\boldsymbol{r}_1^{T\,W}\boldsymbol{C}_{B}\boldsymbol{K}_{\boldsymbol{d}} & \boldsymbol{\Lambda}_{\mathbf{1}} & \mathbf{0}_{3\times3} & {}^{W}\boldsymbol{r}_1^{T\,W}\boldsymbol{C}_{B}\boldsymbol{I}_{33} \end{bmatrix}, \tag{C.9}$$

where

$$\begin{aligned} \boldsymbol{\Theta} &= -\boldsymbol{K}_{\boldsymbol{d}}\left(\boldsymbol{K}_{\boldsymbol{d}} - 2\left\lfloor {}^{B}\boldsymbol{b}_g\right\rfloor_\times\right)\left\lfloor {}^{W}\boldsymbol{C}_{B}^{T}\boldsymbol{g}\right\rfloor_\times \boldsymbol{D}^{-1} \\ \boldsymbol{\Phi} &= \boldsymbol{K}_{\boldsymbol{d}}\left\lfloor\left(-\boldsymbol{K}_{\boldsymbol{d}}{}^{B}\boldsymbol{v} + b_{az}\grave{\boldsymbol{e}}_{\mathbf{3}} - 2{}^{W}\boldsymbol{C}_{B}^{T}\boldsymbol{g}\right)\right\rfloor_\times - \boldsymbol{K}_{\boldsymbol{d}}\left(\boldsymbol{K}_{\boldsymbol{d}} - \left\lfloor {}^{B}\boldsymbol{b}_g\right\rfloor_\times\right)\left\lfloor {}^{B}\boldsymbol{v}\right\rfloor_\times + \boldsymbol{K}_{\boldsymbol{d}}\left\lfloor\left\lfloor {}^{B}\boldsymbol{b}_g\right\rfloor_\times {}^{B}\boldsymbol{v}\right\rfloor_\times \\ \boldsymbol{\Lambda}_{\mathbf{1}} &= -{}^{W}\boldsymbol{r}_1^{T}\left(\left\lfloor {}^{W}\boldsymbol{C}_{B}\left(-\boldsymbol{K}_{\boldsymbol{d}}{}^{B}\boldsymbol{v} + b_{az}\grave{\boldsymbol{e}}_{\mathbf{3}}\right)\right\rfloor_\times\right)\left(\boldsymbol{D}^{T}\right)^{-1}, \\ {}^{W}\ddot{\boldsymbol{p}}_{B} &= {}^{W}\boldsymbol{C}_{B}\left(-\boldsymbol{K}_{\boldsymbol{d}}{}^{B}\boldsymbol{v} + b_{az}\grave{\boldsymbol{e}}_{\mathbf{3}} - {}^{W}\boldsymbol{C}_{B}^{T}\boldsymbol{g}\right). \end{aligned}$$

Similarly, the third order Lie derivative of $\mathfrak{L}^2_{\mathbf{f_0}\mathbf{f_0}}\mathbf{h}$ and it's gradient can be expressed as

$$\begin{aligned} \mathfrak{L}^3_{\mathbf{f_0}\mathbf{f_0}\mathbf{f_0}}\mathbf{h} &= \nabla\mathfrak{L}^2_{\mathbf{f_0}\mathbf{f_0}}\mathbf{h}\cdot\mathbf{f_0} \\ &= \begin{bmatrix} -\boldsymbol{K}_{\boldsymbol{d}}\left(\boldsymbol{K}_{\boldsymbol{d}} - \left\lfloor {}^{B}\boldsymbol{b}_g\right\rfloor_\times\right)^2 {}^{B}\dot{\boldsymbol{v}}' + \boldsymbol{K}_{\boldsymbol{d}}\left(\boldsymbol{K}_{\boldsymbol{d}} - 2\left\lfloor {}^{B}\boldsymbol{b}_g\right\rfloor_\times\right)\left\lfloor {}^{W}\boldsymbol{C}_{B}^{T}\boldsymbol{g}\right\rfloor_\times {}^{B}\boldsymbol{b}_g \\ {}^{W}\ddot{\boldsymbol{p}}_{B}^{T\,W}\boldsymbol{C}_{B}{}^{B}\boldsymbol{v} + \left(2{}^{B}\boldsymbol{v}^{T} - {}^{W}\boldsymbol{r}_1^{T\,W}\boldsymbol{C}_{B}\boldsymbol{K}_{\boldsymbol{d}}\right){}^{B}\dot{\boldsymbol{v}}' + {}^{W}\boldsymbol{r}_1^{T\,W}\boldsymbol{C}_{B}\left\lfloor -\boldsymbol{K}_{\boldsymbol{d}}{}^{B}\boldsymbol{v} + b_{az}\grave{\boldsymbol{e}}_{\mathbf{3}}\right\rfloor_\times {}^{B}\boldsymbol{b}_g \end{bmatrix}, \end{aligned} \tag{C.10}$$

$$\nabla \mathfrak{L}^3_{\mathbf{f_0 f_0 f_0}} \mathbf{h} = \begin{bmatrix} \mathbf{0}_{3\times 3} & \boldsymbol{K_d}\left(\boldsymbol{K_d} - \lfloor {}^{B}\boldsymbol{b}_g \rfloor_\times\right)^3 & \mathbf{\Pi}_1 & \mathbf{\Pi}_2 & -\boldsymbol{K_d}\left(\boldsymbol{K_d} - \lfloor {}^{B}\boldsymbol{b}_g \rfloor_\times\right)^2 \boldsymbol{I}_{33} \\ \mathbf{\Pi}_3 & \mathbf{\Pi}_4 & \mathbf{\Pi}_5 & \mathbf{\Pi}_6 & \mathbf{\Pi}_7 \end{bmatrix}, \tag{C.11}$$

where

$$\mathbf{\Pi}_1 = \boldsymbol{K_d}\left(\boldsymbol{K_d} - \lfloor {}^{B}\boldsymbol{b}_g \rfloor_\times\right)^2 \left\lfloor {}^{W}\boldsymbol{C}_{B}^{T}\boldsymbol{g} \right\rfloor_\times \boldsymbol{D}^{-1} - \boldsymbol{K_d}\left(\boldsymbol{K_d} - 2\lfloor {}^{B}\boldsymbol{b}_g \rfloor_\times\right) \lfloor {}^{B}\boldsymbol{b}_g \rfloor_\times \left\lfloor {}^{W}\boldsymbol{C}_{B}^{T}\boldsymbol{g} \right\rfloor_\times \boldsymbol{D}^{-1} \tag{C.12}$$

$$\begin{aligned} \mathbf{\Pi}_2 = {} & \boldsymbol{K}_{\boldsymbol{d}}^{3} \lfloor {}^{B}\boldsymbol{v} \rfloor_\times + \boldsymbol{K}_{\boldsymbol{d}}^{2}\left(-\lfloor {}^{B}\boldsymbol{b}_g \rfloor_\times \lfloor {}^{B}\boldsymbol{v} \rfloor_\times - \left\lfloor \lfloor {}^{B}\boldsymbol{b}_g \rfloor_\times {}^{B}\boldsymbol{v} \right\rfloor_\times\right) \\ & + \boldsymbol{K_d}\left(-\lfloor {}^{B}\boldsymbol{b}_g \rfloor_\times \boldsymbol{K_d} \lfloor {}^{B}\boldsymbol{v} \rfloor_\times - \left\lfloor \boldsymbol{K_d} \lfloor {}^{B}\boldsymbol{b}_g \rfloor_\times {}^{B}\boldsymbol{v} \right\rfloor_\times\right) - \frac{\partial}{\partial {}^{B}\boldsymbol{b}_g}\left(\boldsymbol{K_d} \lfloor {}^{B}\boldsymbol{b}_g \rfloor_\times^{3} {}^{B}\boldsymbol{v}\right) \end{aligned} \tag{C.13}$$

$$\mathbf{\Pi}_3 = -({}^{W}\boldsymbol{C}_{B}\boldsymbol{K_d}{}^{B}\dot{\boldsymbol{v}}')^T + \left({}^{W}\boldsymbol{C}_{B} \lfloor (-\boldsymbol{K_d}{}^{B}\boldsymbol{v} + b_{az}\grave{\boldsymbol{e}}_{\boldsymbol{3}}) \rfloor_\times {}^{B}\boldsymbol{b}_g\right)^T \tag{C.14}$$

$$\mathbf{\Pi}_4 = 3\left(-2\boldsymbol{K_d}{}^{B}\boldsymbol{v} + b_{az}\grave{\boldsymbol{e}}_{\boldsymbol{3}} - {}^{W}\boldsymbol{C}_{B}\boldsymbol{g}\right)^T - {}^{W}\boldsymbol{r}_1^{T\,W}\boldsymbol{C}_{B}\left(-\boldsymbol{K}_{\boldsymbol{d}}^{2} + \boldsymbol{K_d}\lfloor {}^{B}\boldsymbol{b}_g \rfloor_\times - \lfloor {}^{B}\boldsymbol{b}_g \rfloor_\times \boldsymbol{K_d}\right) \tag{C.15}$$

$$\begin{aligned} \mathbf{\Pi}_5 = {} & -3{}^{B}\boldsymbol{v}^T \left\lfloor {}^{W}\boldsymbol{C}_{B}^{T}\boldsymbol{g} \right\rfloor_\times \boldsymbol{D}^{-1} - \left[\left(\left(-\boldsymbol{K_d} + \lfloor {}^{B}\boldsymbol{b}_g \rfloor_\times\right) {}^{B}\boldsymbol{v} + b_{az}\grave{\boldsymbol{e}}_{\boldsymbol{3}}\right)\right]^T \left\lfloor {}^{W}\boldsymbol{C}_{B}^{T\,W}\boldsymbol{r}_1 \right\rfloor_\times \boldsymbol{D}^{-1} \\ & + \left({}^{W}\boldsymbol{C}_{B}^{T\,W}\boldsymbol{r}_1\right)^T \boldsymbol{K_d} \left\lfloor {}^{W}\boldsymbol{C}_{B}^{T}\boldsymbol{g} \right\rfloor_\times \boldsymbol{D}^{-1} + \left(\boldsymbol{K_d}{}^{W}\boldsymbol{C}_{B}^{T}\boldsymbol{g}\right)^T \left\lfloor {}^{W}\boldsymbol{C}_{B}^{T\,W}\boldsymbol{r}_1 \right\rfloor_\times \boldsymbol{D}^{-1} \\ & + \left(\lfloor -\boldsymbol{K_d}{}^{B}\boldsymbol{v} + b_{az}\grave{\boldsymbol{e}}_{\boldsymbol{3}} \rfloor_\times {}^{B}\boldsymbol{b}_g\right)^T \left\lfloor {}^{W}\boldsymbol{C}_{B}^{T\,W}\boldsymbol{r}_1 \right\rfloor_\times \boldsymbol{D}^{-1} \end{aligned} \tag{C.16}$$

$$\mathbf{\Pi}_6 = {}^{W}\boldsymbol{r}_1^{T\,W}\boldsymbol{C}_{B}\left(\boldsymbol{K_d}\lfloor {}^{B}\boldsymbol{v} \rfloor_\times + \lfloor -\boldsymbol{K_d}{}^{B}\boldsymbol{v} + b_{az}\grave{\boldsymbol{e}}_{\boldsymbol{3}} \rfloor_\times\right) \tag{C.17}$$

$$\mathbf{\Pi}_7 = 3{}^{B}\boldsymbol{v}^T\boldsymbol{I}_{33} - ({}^{W}\boldsymbol{C}_{B}^{T\,W}\boldsymbol{r}_1)^T\left(K + \lfloor {}^{B}\boldsymbol{b}_g \rfloor_\times\right)\boldsymbol{I}_{33} \tag{C.18}$$

Using (aC.4),(C.7)(C.9), and (C.11), the observability matrix can be expressed as

$$\boldsymbol{\mathcal{O}}_{1R} =$$

$$\begin{bmatrix}
\mathbf{0}_{3\times3} & -\boldsymbol{K_d} & \mathbf{0}_{3\times3} & \mathbf{0}_{3\times3} & \boldsymbol{I_3} \\
{}^{W}\boldsymbol{r}_1^T & \mathbf{0}_{1\times3} & \mathbf{0}_{1\times3} & \mathbf{0}_{1\times3} & \mathbf{0}_{1\times3} \\
\mathbf{0}_{3\times3} & \boldsymbol{K_d}\left(\boldsymbol{K_d} - \lfloor {}^{B}\boldsymbol{b}_g \rfloor_\times\right) & \boldsymbol{K_d}\left\lfloor {}^{W}\boldsymbol{C}_{B}^T\boldsymbol{g} \right\rfloor_\times \boldsymbol{D}^{-1} & \boldsymbol{K_d}\lfloor {}^{B}\boldsymbol{v} \rfloor_\times & \boldsymbol{K_d}\boldsymbol{I}_{33} \\
({}^{W}\boldsymbol{C}_{B}{}^{B}\boldsymbol{v})^T & {}^{W}\boldsymbol{r}_1^{T\,W}\boldsymbol{C}_{B} & -{}^{W}\boldsymbol{r}_1^T \lfloor {}^{W}\boldsymbol{C}_{B}{}^{B}\boldsymbol{v} \rfloor_\times \left(\boldsymbol{D}^T\right)^{-1} & \mathbf{0}_{1\times3} & \mathbf{0}_{1\times3} \\
\mathbf{0}_{3\times3} & -\boldsymbol{K_d}\left(\boldsymbol{K_d} - \lfloor {}^{B}\boldsymbol{b}_g \rfloor_\times\right)^2 & \boldsymbol{\Theta} & \boldsymbol{\Phi} & \boldsymbol{K_d}\left(\boldsymbol{K_d} - \lfloor {}^{B}\boldsymbol{b}_g \rfloor_\times\right)\boldsymbol{I}_{33} \\
{}^{W}\ddot{\boldsymbol{p}}_{B}^T & 2{}^{B}\boldsymbol{v}^T - {}^{W}\boldsymbol{r}_1^{T\,W}\boldsymbol{C}_{B}\boldsymbol{K_d} & \boldsymbol{\Lambda_1} & \mathbf{0}_{1\times3} & {}^{W}\boldsymbol{r}_1^{T\,W}\boldsymbol{C}_{B}\boldsymbol{I}_{33} \\
\mathbf{0}_{3\times3} & \boldsymbol{K_d}\left(\boldsymbol{K_d} - \lfloor {}^{B}\boldsymbol{b}_g \rfloor_\times\right)^3 & \boldsymbol{\Pi}_1 & \boldsymbol{\Pi}_2 & -\boldsymbol{K_d}\left(\boldsymbol{K_d} - \lfloor {}^{B}\boldsymbol{b}_g \rfloor_\times\right)^2 \boldsymbol{I}_{33} \\
\boldsymbol{\Pi}_3 & \boldsymbol{\Pi}_4 & \boldsymbol{\Pi}_5 & \boldsymbol{\Pi}_6 & \boldsymbol{\Pi}_7
\end{bmatrix} \tag{C.19}$$

Appendix D

Observability Analysis of AHRS

A attitude and heading reference system consists of three axis gyroscope, three axis accelerometer, and three axis magnetometer to estimate the orientation. Since this thesis take the aerodynamic drag forces acting on the MAV into consideration, the velocity of the MAV is included as a state of the AHRS. The AHRS with the aerodynamic drag forces effects has the following state vector[1]

$$\mathbf{x} = \begin{bmatrix} {}^{B}\boldsymbol{v}^T & {}^{W}\boldsymbol{s}_B^T & {}^{B}\boldsymbol{b}_g^T & {}^{B}\boldsymbol{b}_a^T \end{bmatrix}^T, \tag{D.1}$$

Using the definitions given in (3.34), (3.36), (3.41), and (3.47) the nonlinear state space model of the AHRS can be expressed as

---

[1] The orientation is parameterized using Gibbs parameterization due to the ease of conducting the observability analysis. An implementation of the AHRS would use the quaternion parameterization to represent the orientation.

$$\begin{bmatrix} {}^B\dot{\boldsymbol{v}} \\ {}^W\dot{\boldsymbol{s}}_B \\ {}^B\dot{\boldsymbol{b}}_g \\ {}^B\dot{\boldsymbol{b}}_a \end{bmatrix} = \begin{bmatrix} \lfloor {}^B\boldsymbol{v} \rfloor_\times ({}^B\boldsymbol{\omega}_m - {}^B\boldsymbol{b}_g - \boldsymbol{\eta}_\omega) - \boldsymbol{K_d}{}^B\boldsymbol{v} + b_{az}\grave{\boldsymbol{e}}_{\boldsymbol{3}} - {}^W\boldsymbol{C}_B^T\boldsymbol{g} \\ \boldsymbol{D}({}^B\boldsymbol{\omega}_m - {}^B\boldsymbol{b}_g - \boldsymbol{\eta}_\omega) \\ \boldsymbol{\eta_{gb}} \\ \boldsymbol{\eta_{ab}} \end{bmatrix} \tag{D.2}$$

The control affine form the state space model in (D.2) can be expressed as

$$\begin{bmatrix} {}^B\dot{\boldsymbol{v}} \\ {}^W\dot{\boldsymbol{s}}_B \\ {}^B\dot{\boldsymbol{b}}_g \\ {}^B\dot{\boldsymbol{b}}_a \end{bmatrix} = \underbrace{\begin{bmatrix} -\lfloor {}^B\boldsymbol{v} \rfloor_\times {}^B\boldsymbol{b}_g - \boldsymbol{K_d}{}^B\boldsymbol{v} + b_{az}\grave{\boldsymbol{e}}_{\boldsymbol{3}} - {}^W\boldsymbol{C}_B^T\boldsymbol{g} \\ -\boldsymbol{D}{}^B\boldsymbol{b}_g \\ \mathbf{0}_{3\times1} \\ \mathbf{0}_{3\times1} \end{bmatrix}}_{\mathbf{f_0}} + \underbrace{\begin{bmatrix} \lfloor {}^B\boldsymbol{v} \rfloor_\times \\ \boldsymbol{D} \\ \mathbf{0}_{3\times3} \\ \mathbf{0}_{3\times3} \end{bmatrix}}_{\mathbf{f_1}} {}^B\boldsymbol{\omega}_m. \tag{D.3}$$

The measurement model of the AHRS includes the accelerometer and magnetometer measurements. Using the definitions given in (3.42), and (5.15), the measurement model can be expressed as

$$\mathbf{y} = \mathbf{h}(\mathbf{x}) = \begin{bmatrix} \mathbf{h}_a(\mathbf{x}) \\ \mathbf{h}_\mu(\mathbf{x}) \end{bmatrix} = \begin{bmatrix} -\boldsymbol{K_d}{}^B\boldsymbol{v} + {}^B\boldsymbol{b}_a + \boldsymbol{\eta_a} \\ {}^W\boldsymbol{C}_B^{T\,W}\boldsymbol{\mu} + \boldsymbol{\eta_\mu} \end{bmatrix}, \tag{D.4}$$

Observability Analysis

The nonlinear observability analysis of the AHRS is conducted by constructing the observability matrix and determining the rank of the observability matrix. The Lie derivatives of the output function and their gradients can be calculated as follows

$$\mathfrak{L}^0\mathbf{h} = \mathbf{h}(\mathbf{x}) \tag{D.5}$$

$$\nabla\mathfrak{L}^0\mathbf{h} = \begin{bmatrix} -\boldsymbol{K_d} & \mathbf{0}_{3\times3} & \mathbf{0}_{3\times3} & \boldsymbol{I_3} \\ \mathbf{0}_{3\times3} & \left\lfloor {}^{W}\boldsymbol{C}_{B}^{T}\,{}^{W}\boldsymbol{\mu} \right\rfloor_\times \boldsymbol{D}^{-1} & \mathbf{0}_{3\times3} & \mathbf{0}_{3\times3} \end{bmatrix} \tag{D.6}$$

$$\mathfrak{L}^1_{\mathbf{f_0}}\mathbf{h} = \nabla\mathfrak{L}^0\mathbf{h}\cdot\mathbf{f_0} = \begin{bmatrix} \boldsymbol{K_d}\,{}^{B}\dot{\boldsymbol{v}}' \\ -\left\lfloor {}^{W}\boldsymbol{C}_{B}^{T}\,{}^{W}\boldsymbol{\mu} \right\rfloor_\times {}^{B}\boldsymbol{b}_g \end{bmatrix}, \tag{D.7}$$

where ${}^{B}\dot{\boldsymbol{v}}' = -\left\lfloor {}^{B}\boldsymbol{v} \right\rfloor_\times {}^{B}\boldsymbol{b}_g - \boldsymbol{K_d}\,{}^{B}\boldsymbol{v} + b_{az}\grave{\boldsymbol{e}}_{\boldsymbol{3}} - {}^{W}\boldsymbol{C}_{B}^{T}\boldsymbol{g}$.

$$\nabla\mathfrak{L}^1_{\mathbf{f_0}}\mathbf{h} =$$

$$\begin{bmatrix} \boldsymbol{K_d}\left(\boldsymbol{K_d} - \left\lfloor {}^{B}\boldsymbol{b}_g \right\rfloor_\times\right) & \boldsymbol{K_d}\left\lfloor {}^{W}\boldsymbol{C}_{B}^{T}\boldsymbol{g} \right\rfloor_\times \boldsymbol{D}^{-1} & \boldsymbol{K_d}\left\lfloor {}^{B}\boldsymbol{v} \right\rfloor_\times & -\boldsymbol{K_d}\boldsymbol{I}_{33} \\ \mathbf{0}_{3\times3} & \left\lfloor {}^{B}\boldsymbol{b}_g \right\rfloor_\times \left\lfloor {}^{W}\boldsymbol{C}_{B}^{T}\,{}^{W}\boldsymbol{\mu} \right\rfloor_\times \boldsymbol{D}^{-1} & -\left\lfloor {}^{W}\boldsymbol{C}_{B}^{T}\,{}^{W}\boldsymbol{\mu} \right\rfloor_\times & \mathbf{0}_{3\times3} \end{bmatrix} \tag{D.8}$$

$$\mathfrak{L}^2_{\mathbf{f_0}\mathbf{f_0}}\mathbf{h} = \nabla\mathfrak{L}^1_{\mathbf{f_0}}\mathbf{h}\cdot\mathbf{f_0} = \begin{bmatrix} \boldsymbol{K_d}\left(\boldsymbol{K_d} - \left\lfloor {}^{B}\boldsymbol{b}_g \right\rfloor_\times\right) {}^{B}\dot{\boldsymbol{v}} - \boldsymbol{K_d}\left\lfloor {}^{W}\boldsymbol{C}_{B}^{T}\boldsymbol{g} \right\rfloor_\times {}^{B}\boldsymbol{b}_g \\ -\left\lfloor {}^{B}\boldsymbol{b}_g \right\rfloor_\times \left\lfloor {}^{W}\boldsymbol{C}_{B}^{T}\,{}^{W}\boldsymbol{\mu} \right\rfloor_\times {}^{B}\boldsymbol{b}_g \end{bmatrix} \tag{D.9}$$

$$\nabla\mathfrak{L}^2_{\mathbf{f_0}\mathbf{f_0}}\mathbf{h} =$$

$$\begin{bmatrix} -\boldsymbol{K_d}\left(\boldsymbol{K_d} - \left\lfloor {}^{B}\boldsymbol{b}_g \right\rfloor_\times\right)^2 & \boldsymbol{\Theta} & \boldsymbol{\Phi} & \boldsymbol{K_d}\left(\boldsymbol{K_d} - \left\lfloor {}^{B}\boldsymbol{b}_g \right\rfloor_\times\right)\boldsymbol{I}_{33} \\ \mathbf{0}_{3\times3} & \left\lfloor {}^{B}\boldsymbol{b}_g \right\rfloor_\times^2 \left\lfloor {}^{W}\boldsymbol{C}_{B}^{T}\,{}^{W}\boldsymbol{\mu} \right\rfloor_\times \boldsymbol{D}^{-1} & \boldsymbol{\Delta} & \mathbf{0}_{3\times3} \end{bmatrix}, \tag{D.10}$$

where

$$
\begin{aligned}
\boldsymbol{\Theta} &= -\boldsymbol{K_d}\left(\boldsymbol{K_d} - 2\left\lfloor {}^{B}\boldsymbol{b}_g \right\rfloor_\times\right)\left\lfloor {}^{W}\boldsymbol{C}_B^T\boldsymbol{g}\right\rfloor_\times \boldsymbol{D}^{-1} \\
\boldsymbol{\Phi} &= \boldsymbol{K_d}\left\lfloor\left(-\boldsymbol{K_d}{}^{B}\boldsymbol{v} + b_{az}\grave{\boldsymbol{e}}_{\boldsymbol{3}} - 2{}^{W}\boldsymbol{C}_B^T\boldsymbol{g}\right)\right\rfloor_\times - \boldsymbol{K_d}\left(\boldsymbol{K_d} - \left\lfloor {}^{B}\boldsymbol{b}_g \right\rfloor_\times\right)\left\lfloor {}^{B}\boldsymbol{v}\right\rfloor_\times \ \ldots \\
&\qquad\qquad \ldots \ + \boldsymbol{K_d}\left\lfloor \left\lfloor {}^{B}\boldsymbol{b}_g \right\rfloor_\times {}^{B}\boldsymbol{v}\right\rfloor_\times \\
\boldsymbol{\Delta} &= -\left\lfloor {}^{B}\boldsymbol{b}_g \right\rfloor_\times \left\lfloor {}^{W}\boldsymbol{C}_B^{T\,W}\boldsymbol{\mu}\right\rfloor_\times - \left\lfloor \left\lfloor {}^{B}\boldsymbol{b}_g \right\rfloor_\times {}^{W}\boldsymbol{C}_B^{T\,W}\boldsymbol{\mu}\right\rfloor_\times
\end{aligned}
$$

The observability matrix is calculated by concatenating the gradients (D.6), (D.8), (D.10), and can be expressed as

$$
\boldsymbol{\mathcal{O}_{AHRS}} = \begin{bmatrix} \nabla\mathfrak{L}^0\mathbf{h} \\ \nabla\mathfrak{L}^1_{\mathbf{f_0}}\mathbf{h} \\ \nabla\mathfrak{L}^2_{\mathbf{f_0}\mathbf{f_0}}\mathbf{h} \end{bmatrix}, \tag{D.11}
$$

$$
\boldsymbol{\mathcal{O}_{AHRS}} =
$$
$$
\begin{bmatrix}
-\boldsymbol{K_d} & \mathbf{0}_{3\times3} & \mathbf{0}_{3\times3} & \boldsymbol{I_3} \\
\mathbf{0}_{3\times3} & \left\lfloor {}^{W}\boldsymbol{C}_B^{T\,W}\boldsymbol{\mu}\right\rfloor_\times \boldsymbol{D}^{-1} & \mathbf{0}_{3\times3} & \mathbf{0}_{3\times3} \\
\boldsymbol{K_d}\left(\boldsymbol{K_d} - \left\lfloor {}^{B}\boldsymbol{b}_g \right\rfloor_\times\right) & \boldsymbol{K_d}\left\lfloor {}^{W}\boldsymbol{C}_B^T\boldsymbol{g}\right\rfloor_\times \boldsymbol{D}^{-1} & \boldsymbol{K_d}\left\lfloor {}^{B}\boldsymbol{v}\right\rfloor_\times & -\boldsymbol{K_d}\boldsymbol{I}_{33} \\
\mathbf{0}_{3\times3} & \left\lfloor {}^{B}\boldsymbol{b}_g \right\rfloor_\times \left\lfloor {}^{W}\boldsymbol{C}_B^{T\,W}\boldsymbol{\mu}\right\rfloor_\times \boldsymbol{D}^{-1} & -\left\lfloor {}^{W}\boldsymbol{C}_B^{T\,W}\boldsymbol{\mu}\right\rfloor_\times & \mathbf{0}_{3\times3} \\
-\boldsymbol{K_d}\left(\boldsymbol{K_d} - \left\lfloor {}^{B}\boldsymbol{b}_g \right\rfloor_\times\right)^2 & \boldsymbol{\Theta} & \boldsymbol{\Phi} & \boldsymbol{K_d}\left(\boldsymbol{K_d} - \left\lfloor {}^{B}\boldsymbol{b}_g \right\rfloor_\times\right)\boldsymbol{I}_{33} \\
\mathbf{0}_{3\times3} & \left\lfloor {}^{B}\boldsymbol{b}_g \right\rfloor_\times^2 \left\lfloor {}^{W}\boldsymbol{C}_B^{T\,W}\boldsymbol{\mu}\right\rfloor_\times \boldsymbol{D}^{-1} & \boldsymbol{\Delta} & \mathbf{0}_{3\times3}
\end{bmatrix}. \tag{D.12}
$$

Lemma D.1. *The AHRS which incorporates the aerodynamic drag forces acting on the MAV is locally weakly observable under any trajectory.*

Proof. The rank of the observability matrix is determined by calculating the rank of each block column of $\boldsymbol{\mathcal{O}_{AHRS}}$. The first block elements of the first and the fourth block columns, ($\boldsymbol{\mathcal{O}}_{\boldsymbol{AHRS},(1,1)}$, and $\boldsymbol{\mathcal{O}}_{\boldsymbol{AHRS},(1,4)}$) are diagonal matrices. Therefore, the first and the fourth block columns each has a rank of three. Furthermore, it is straight forward to show that the first and the fourth block columns are linearly independent. Since the earth's magnetic field, ${}^{W}\boldsymbol{\mu}$ and the gravity vector $\boldsymbol{g}$ are not parallel with each other, the matrix $\left[\, \left(\left\lfloor {}^{W}\boldsymbol{C}_{B}^{T\,W}\boldsymbol{\mu}\right\rfloor_{\times} \boldsymbol{D}^{-1}\right)^{T} \;\; \left(\boldsymbol{K_{d}} \left\lfloor {}^{W}\boldsymbol{C}_{B}^{T}\boldsymbol{g}\right\rfloor_{\times} \boldsymbol{D}^{-1}\right)^{T} \,\right]^{T}$ has full rank of three. Therefore, the second block column has full rank. By analyzing the non-zero block elements of the third block column of $\boldsymbol{\mathcal{O}}_{\boldsymbol{AHRS}}$, it can be seen that the third block column has full rank under any trajectory of the MAV (even when the MAV is stationary). Therefore, each block column has full rank irrespective of the MAV's trajectory. Therefore the AHRS is locally weakly observable. $\square$

References

[1] F. Mancini, M. Dubbini, M. Gattelli, F. Stecchi, S. Fabbri, and G. Gabbianelli, “Using unmanned aerial vehicles (uav) for high-resolution reconstruction of topography: The structure from motion approach on coastal environments,” *Remote Sensing*, vol. 5, no. 12, Dec 2013.

[2] M. Mittal, R. Mohan, W. Burgard, and A. Valada, “Vision-based autonomous uav navigation and landing for urban search and rescue,” *arXiv preprint arXiv:1906.01304*, 2019.

[3] A. Patrik, G. Utama, A. A. S. Gunawan, A. Chowanda, J. S. Suroso, R. Shofiyanti, and W. Budiharto, “Gnss-based navigation systems of autonomous drone for delivering items,” *Journal of Big Data*, vol. 6, no. 1, pp. 1–14, 2019.

[4] J. Grzybowski, K. Latos, and R. Czyba, “Low-cost autonomous uav-based solutions to package delivery logistics,” in *Advanced, Contemporary Control.* Springer, 2020, pp. 500–507.

[5] J. Li, Y. Bi, K. Li, K. Wang, F. Lin, and B. M. Chen, “Accurate 3d localization for mav swarms by uwb and imu fusion,” in *2018 IEEE 14th International Conference on Control and Automation (ICCA).* IEEE, 2018, pp. 100–105.

[6] F. Dietrich, J. Marzat, M. Sanfourche, S. Bertrand, A. Bernard-Brunel, and A. Eudes, “Mav tele-operation constrained on virtual surfaces for inspection of infrastructures,” in *2020 25th IEEE International Conference on Emerging Technologies and Factory Automation (ETFA)*, vol. 1. IEEE, 2020, pp. 1519–1525.

[7] F. Hoffmann, N. Goddemeier, and T. Bertram, “Attitude estimation and control of a quadrocopter,” in *2010 IEEE/RSJ International Conference on Intelligent Robots and Systems.* IEEE, 2010, pp. 1072–1077.

[8] L. Arreola, A. M. De Oca, A. Flores, J. Sanchez, and G. Flores, “Improvement in the uav position estimation with low-cost gps, ins and vision-based system: Application to a quadrotor uav,” in *2018 International Conference on Unmanned Aircraft Systems (ICUAS).* IEEE, 2018, pp. 1248–1254.

[9] H. Durrant-Whyte and T. Bailey, "Simultaneous localization and mapping: part i," *IEEE robotics & automation magazine*, vol. 13, no. 2, pp. 99–110, 2006.

[10] W. G. Aguilar, G. A. Rodríguez, L. Álvarez, S. Sandoval, F. Quisaguano, and A. Limaico, "Visual slam with a rgb-d camera on a quadrotor uav using on-board processing," in *International Work-Conference on Artificial Neural Networks*. Springer, 2017, pp. 596–606.

[11] T. Qin, P. Li, and S. Shen, "Vins-mono: A robust and versatile monocular visual-inertial state estimator," *IEEE Transactions on Robotics*, vol. 34, no. 4, pp. 1004–1020, 2018.

[12] J.-Y. Lee and R. A. Scholtz, "Ranging in a dense multipath environment using an uwb radio link," *IEEE journal on selected areas in communications*, vol. 20, no. 9, pp. 1677–1683, 2002.

[13] B. Fang, "Simple solutions for hyperbolic and related position fixes," *IEEE Transactions on Aerospace and Electronic Systems*, vol. 26, no. 5, pp. 748–753, 1990.

[14] A. Benini, A. Mancini, and S. Longhi, "An imu/uwb/vision-based extended kalman filter for mini-uav localization in indoor environment using 802.15. 4a wireless sensor network," *Journal of Intelligent & Robotic Systems*, vol. 70, no. 1, pp. 461–476, 2013.

[15] M. Bangura, R. Mahony *et al.*, "Nonlinear dynamic modeling for high performance control of a quadrotor," , 2012.

[16] K. Guo, Z. Qiu, C. Miao, A. H. Zaini, C.-L. Chen, W. Meng, and L. Xie, "Ultra-wideband-based localization for quadcopter navigation," *Unmanned Systems*, vol. 4, no. 01, pp. 23–34, 2016.

[17] C. Wang, A. Xu, J. Kuang, X. Sui, Y. Hao, and X. Niu, "A high-accuracy indoor localization system and applications based on tightly coupled uwb/ins/floor map integration," *IEEE Sensors Journal*, vol. 21, no. 16, pp. 18 166–18 177, 2021.

[18] M. T. Sabet, H. M. Daniali, A. Fathi, and E. Alizadeh, "Identification of an autonomous underwater vehicle hydrodynamic model using the extended, cubature, and transformed unscented kalman filter," *IEEE Journal of Oceanic Engineering*, vol. 43, no. 2, pp. 457–467, 2017.

[19] R. Garcia, P. Pardal, H. Kuga, and M. Zanardi, "Nonlinear filtering for sequential spacecraft attitude estimation with real data: Cubature kalman filter, unscented kalman filter and extended kalman filter," *Advances in Space Research*, vol. 63, no. 2, pp. 1038–1050, 2019.

[20] Y. Bar-Shalom, X. R. Li, and T. Kirubarajan, *Estimation with applications to tracking and navigation: theory algorithms and software.* New York: John Wiley & Sons, 2004.

[21] G. P. Huang, A. I. Mourikis, and S. I. Roumeliotis, "Analysis and improvement of the consistency of extended kalman filter based slam," in *2008 IEEE International Conference on Robotics and Automation*, 2008, pp. 473–479.

[22] A. Nemra and N. Aouf, "Robust airborne 3d visual simultaneous localization and mapping with observability and consistency analysis," *Journal of Intelligent and Robotic Systems*, vol. 55, no. 4, pp. 345–376, 2009.

[23] J. A. Hesch, D. G. Kottas, S. L. Bowman, and S. I. Roumeliotis, "Observability-constrained vision-aided inertial navigation," *University of Minnesota, Dept. of Comp. Sci. & Eng., MARS Lab, Tech. Rep*, vol. 1, p. 6, 2012.

[24] Y. T. Tan, R. Gao, and M. Chitre, "Cooperative path planning for range-only localization using a single moving beacon," *IEEE Journal of Oceanic Engineering*, vol. 39, no. 2, pp. 371–385, 2014.

[25] F. Arrichiello, G. Antonelli, A. P. Aguiar, and A. Pascoal, "Observability metric for the relative localization of auvs based on range and depth measurements: Theory and experiments," in *2011 IEEE/RSJ International Conference on Intelligent Robots and Systems*, Sept 2011, pp. 3166–3171.

[26] A. S. Gadre and D. J. Stilwell, "Underwater navigation in the presence of unknown currents based on range measurements from a single location," in *Proceedings of the 2005, American Control Conference, 2005.*, June 2005, pp. 656–661 vol. 1.

[27] P. Batista, C. Silvestre, and P. Oliveira, "Single range aided navigation and source localization: Observability and filter design," *Systems & Control Letters*, vol. 60, no. 8, pp. 665–673, 2011.

[28] S. Van Der Helm, M. Coppola, K. N. McGuire, and G. C. de Croon, "On-board range-based relative localization for micro air vehicles in indoor leader–follower flight," *Autonomous Robots*, vol. 44, no. 3, pp. 415–441, 2020.

[29] N. Michael, D. Mellinger, Q. Lindsey, and V. Kumar, "The grasp multiple micro-uav testbed," *IEEE Robotics & Automation Magazine*, vol. 17, no. 3, pp. 56–65, 2010.

[30] V. Grabe, H. H. Bülthoff, and P. R. Giordano, "A comparison of scale estimation schemes for a quadrotor uav based on optical flow and imu measurements," in *2013 IEEE/RSJ international conference on intelligent robots and systems.* IEEE, 2013, pp. 5193–5200.

[31] S. Bouabdallah, P. Murrieri, and R. Siegwart, "Design and control of an indoor micro quadrotor," in *IEEE International Conference on Robotics and Automation, 2004. Proceedings. ICRA'04. 2004*, vol. 5. IEEE, 2004, pp. 4393–4398.

[32] P. McKerrow, "Modelling the draganflyer four-rotor helicopter," in *IEEE International Conference on Robotics and Automation, 2004. Proceedings. ICRA '04. 2004*, vol. 4, 2004, pp. 3596–3601 Vol.4.

[33] T. Bresciani, "Modelling, identification and control of a quadrotor helicopter," *MSc theses*, 2008.

[34] L. Derafa, T. Madani, and A. Benallegue, "Dynamic modelling and experimental identification of four rotors helicopter parameters," in *2006 IEEE international conference on industrial technology.* IEEE, 2006, pp. 1834–1839.

[35] G. Hoffmann, H. Huang, S. Waslander, and C. Tomlin, "Quadrotor helicopter flight dynamics and control: Theory and experiment," in *AIAA guidance, navigation and control conference and exhibit*, 2007, p. 6461.

[36] R. C. Leishman, J. C. Macdonald, R. W. Beard, and T. W. McLain, "Quadrotors and accelerometers: State estimation with an improved dynamic model," *IEEE Control Systems Magazine*, vol. 34, no. 1, pp. 28–41, 2014.

[37] D. Abeywardena, S. Kodagoda, G. Dissanayake, and R. Munasinghe, "Improved state estimation in quadrotor mavs: A novel drift-free velocity estimator," *IEEE Robotics & Automation Magazine*, vol. 20, no. 4, pp. 32–39, 2013.

[38] D. A. Mercado, G. Flores, P. Castillo, J. Escareno, and R. Lozano, "Gps/ins/optic flow data fusion for position and velocity estimation," in *2013 International Conference on Unmanned Aircraft Systems (ICUAS).* IEEE, 2013, pp. 486–491.

[39] M. J. Choi, Y. H. Kim, E. J. Kim, and J. W. Song, "Enhancement of heading accuracy for gps/ins by employing average velocity in low dynamic situations," *IEEE Access*, vol. 8, pp. 43 826–43 837, 2020.

[40] A. J. Davison, I. D. Reid, N. D. Molton, and O. Stasse, "Monoslam: Real-time single camera slam," *IEEE transactions on pattern analysis and machine intelligence*, vol. 29, no. 6, pp. 1052–1067, 2007.

[41] M. Blösch, S. Weiss, D. Scaramuzza, and R. Siegwart, "Vision based mav navigation in unknown and unstructured environments," in *2010 IEEE International Conference on Robotics and Automation.* IEEE, 2010, pp. 21–28.

[42] K. Schauwecker and A. Zell, "On-board dual-stereo-vision for autonomous quadrotor navigation," in *2013 International Conference on Unmanned Aircraft Systems (ICUAS).* IEEE, 2013, pp. 333–342.

[43] R. Ait-Jellal and A. Zell, “Outdoor obstacle avoidance based on hybrid visual stereo slam for an autonomous quadrotor mav,” in *2017 European Conference on Mobile Robots (ECMR)*. IEEE, 2017, pp. 1–8.

[44] P. Zhang, R. Li, Y. Shi, and L. He, “Indoor navigation for quadrotor using rgb-d camera,” in *Proceedings of 2018 Chinese Intelligent Systems Conference*. Springer, 2019, pp. 497–506.

[45] A. I. Mourikis, S. I. Roumeliotis *et al.*, “A multi-state constraint kalman filter for vision-aided inertial navigation.” in *ICRA*, vol. 2, 2007, p. 6.

[46] B. Williams, M. Cummins, J. Neira, P. Newman, I. Reid, and J. Tardós, “A comparison of loop closing techniques in monocular slam,” *Robotics and Autonomous Systems*, vol. 57, no. 12, pp. 1188–1197, 2009.

[47] O. G. Grasa, J. Civera, and J. Montiel, “Ekf monocular slam with relocalization for laparoscopic sequences,” in *2011 IEEE International Conference on Robotics and Automation*. IEEE, 2011, pp. 4816–4821.

[48] E. Xu, Z. Ding, and S. Dasgupta, “Source localization in wireless sensor networks from signal time-of-arrival measurements,” *IEEE Transactions on Signal Processing*, vol. 59, no. 6, pp. 2887–2897, 2011.

[49] H. Xiong, Z. Chen, W. An, and B. Yang, “Robust tdoa localization algorithm for asynchronous wireless sensor networks,” *International Journal of Distributed Sensor Networks*, vol. 11, no. 5, p. 598747, 2015.

[50] S. Tomic, M. Beko, and R. Dinis, “Rss-based localization in wireless sensor networks using convex relaxation: Noncooperative and cooperative schemes,” *IEEE Transactions on Vehicular Technology*, vol. 64, no. 5, pp. 2037–2050, 2014.

[51] R. S. Kshetrimayum, “An introduction to uwb communication systems,” *Ieee Potentials*, vol. 28, no. 2, pp. 9–13, 2009.

[52] Z. Low, J. Cheong, C. Law, W. Ng, and Y. Lee, “Pulse detection algorithm for line-of-sight (los) uwb ranging applications,” *IEEE Antennas and Wireless Propagation Letters*, vol. 4, pp. 63–67, 2005.

[53] A. Prorok, P. Tomé, and A. Martinoli, “Accommodation of nlos for ultra-wideband tdoa localization in single-and multi-robot systems,” in *2011 international conference on indoor positioning and indoor navigation*. IEEE, 2011, pp. 1–9.

[54] U. Ltd. (2022) Dimension4™ uwb real-time location system (rtls). [Online]. Available: https://ubisense.com/dimension4/

[55] Decawave. (2022) Decawave ultra-wideband rtls. [Online]. Available: https://www.decawave.com/products

[56] Sewio. (2022) Sewio uwb real-time localization system. [Online]. Available: https://www.sewio.net/real-time-location-system-rtls-on-uwb

[57] C.-Y. Shih and P. J. Marrón, "Cola: Complexity-reduced trilateration approach for 3d localization in wireless sensor networks," in *2010 Fourth International Conference on Sensor Technologies and Applications.* IEEE, 2010, pp. 24–32.

[58] S. Yiu, M. Dashti, H. Claussen, and F. Perez-Cruz, "Wireless rssi fingerprinting localization," *Signal Processing*, vol. 131, pp. 235–244, 2017.

[59] J. Xu, J. He, Y. Zhang, F. Xu, and F. Cai, "A distance-based maximum likelihood estimation method for sensor localization in wireless sensor networks," *International Journal of Distributed Sensor Networks*, vol. 12, no. 4, p. 2080536, 2016.

[60] S. Krishnan, P. Sharma, Z. Guoping, and O. H. Woon, "A uwb based localization system for indoor robot navigation," in *2007 IEEE International Conference on Ultra-Wideband.* IEEE, 2007, pp. 77–82.

[61] M. Hamer and R. D'Andrea, "Self-calibrating ultra-wideband network supporting multi-robot localization," *IEEE Access*, vol. 6, pp. 22 292–22 304, 2018.

[62] N. Macoir, J. Bauwens, B. Jooris, B. Van Herbruggen, J. Rossey, J. Hoebeke, and E. De Poorter, "Uwb localization with battery-powered wireless backbone for drone-based inventory management," *Sensors*, vol. 19, no. 3, p. 467, 2019.

[63] L. Barbieri, M. Brambilla, A. Trabattoni, S. Mervic, and M. Nicoli, "Uwb localization in a smart factory: augmentation methods and experimental assessment," *IEEE Transactions on Instrumentation and Measurement*, vol. 70, pp. 1–18, 2021.

[64] N. Trawny, X. S. Zhou, K. X. Zhou, and S. I. Roumeliotis, "3d relative pose estimation from distance-only measurements," in *2007 IEEE/RSJ International Conference on Intelligent Robots and Systems.* IEEE, 2007, pp. 1071–1078.

[65] N. Trawny, X. S. Zhou, K. Zhou, and S. I. Roumeliotis, "Interrobot transformations in 3-d," *IEEE Transactions on Robotics*, vol. 26, no. 2, pp. 226–243, 2010.

[66] B. Ferreira, A. Matos, and N. Cruz, "Single beacon navigation: Localization and control of the mares auv," in *OCEANS 2010 MTS/IEEE SEATTLE.* IEEE, 2010, pp. 1–9.

[67] G. Indiveri, D. De Palma, and G. Parlangeli, “Single range localization in 3-d: Observability and robustness issues,” *IEEE Transactions on Control Systems Technology*, vol. 24, no. 5, pp. 1853–1860, Sep. 2016.

[68] D. Unsal and K. Demirbas, “Estimation of deterministic and stochastic imu error parameters,” in *Proceedings of IEEE/ION PLANS 2012*, 2012, pp. 862–868.

[69] F. Berefelt, B. Boberg, J. Nygårds, P. Strömbäck, and S.-L. Wirkander, “Collaborative gps/ins navigation in urban environment,” in *Proceedings of the 2004 National Technical Meeting of The Institute of Navigation*, 2004, pp. 1114–1125.

[70] J. Wendel and G. F. Trommer, “Tightly coupled gps/ins integration for missile applications,” *Aerospace Science and Technology*, vol. 8, no. 7, pp. 627–634, 2004.

[71] J. D. Hol, F. Dijkstra, H. Luinge, and T. B. Schon, “Tightly coupled uwb/imu pose estimation,” in *2009 IEEE international conference on ultra-wideband.* IEEE, 2009, pp. 688–692.

[72] A. Goudar and A. P. Schoellig, “Online spatio-temporal calibration of tightly-coupled ultrawideband-aided inertial localization,” in *2021 IEEE/RSJ International Conference on Intelligent Robots and Systems (IROS).* IEEE, 2021, pp. 1161–1168.

[73] M. W. Mueller, M. Hamer, and R. D’Andrea, “Fusing ultra-wideband range measurements with accelerometers and rate gyroscopes for quadrocopter state estimation,” in *2015 IEEE International Conference on Robotics and Automation (ICRA).* IEEE, 2015, pp. 1730–1736.

[74] W. You, F. Li, L. Liao, and M. Huang, “Data fusion of uwb and imu based on unscented kalman filter for indoor localization of quadrotor uav,” *IEEE Access*, vol. 8, pp. 64 971–64 981, 2020.

[75] D. Feng, C. Wang, C. He, Y. Zhuang, and X.-G. Xia, “Kalman-filter-based integration of imu and uwb for high-accuracy indoor positioning and navigation,” *IEEE Internet of Things Journal*, vol. 7, no. 4, pp. 3133–3146, 2020.

[76] C. He, C. Tang, and C. Yu, “A federated derivative cubature kalman filter for imu-uwb indoor positioning,” *Sensors*, vol. 20, no. 12, p. 3514, 2020.

[77] C. Tang, C. He, and L. Dou, “An imu/odm/uwb joint localization system based on modified cubature kalman filtering,” *Sensors*, vol. 21, no. 14, p. 4823, 2021.

[78] S. Pfeiffer, C. De Wagter, and G. C. De Croon, “A computationally efficient moving horizon estimator for ultra-wideband localization on small quadrotors,” *IEEE Robotics and Automation Letters*, vol. 6, no. 4, pp. 6725–6732, 2021.

[79] Y. Li, Y. Ying, and W. Dong, “A computationally efficient moving horizon estimation for flying robots’ localization regarding a single anchor,” in *2021 IEEE International Conference on Robotics and Biomimetics (ROBIO)*. IEEE, 2021, pp. 675–680.

[80] R. E. Kalman, “On the general theory of control systems,” in *Proceedings First International Conference on Automatic Control, Moscow, USSR*, 1960, pp. 481–492.

[81] R. Hermann and A. Krener, “Nonlinear controllability and observability,” *IEEE Transactions on automatic control*, vol. 22, no. 5, pp. 728–740, 1977.

[82] O. De Silva, G. K. Mann, and R. G. Gosine, “Observability analysis of relative localization filters subjected to platform velocity constraints,” *Journal of Dynamic Systems, Measurement, and Control*, vol. 139, no. 5, 2017.

[83] J. A. Hesch, D. G. Kottas, S. L. Bowman, and S. I. Roumeliotis, “Camera-imu-based localization: Observability analysis and consistency improvement,” *The International Journal of Robotics Research*, vol. 33, no. 1, pp. 182–201, 2014.

[84] M. D. Shuster *et al.*, “A survey of attitude representations,” *Navigation*, vol. 8, no. 9, pp. 439–517, 1993.

[85] L. Palopoli and D. Fontanelli, “Global observability analysis of a nonholonomic robot using range sensors,” in *2020 European Control Conference (ECC)*, 2020, pp. 1300–1305.

[86] P. Batista, C. Silvestre, and P. Oliveira, “Single beacon navigation: Observability analysis and filter design,” in *Proceedings of the 2010 American Control Conference*. IEEE, 2010, pp. 6191–6196.

[87] S. J. Julier and J. K. Uhlmann, “A counter example to the theory of simultaneous localization and map building,” in *Proceedings 2001 ICRA. IEEE International Conference on Robotics and Automation (Cat. No. 01CH37164)*, vol. 4. IEEE, 2001, pp. 4238–4243.

[88] G. P. Huang, A. I. Mourikis, and S. I. Roumeliotis, “A first-estimates jacobian ekf for improving slam consistency,” in *Experimental Robotics*. Springer, 2009, pp. 373–382.

[89] K. Wu, T. Zhang, D. Su, S. Huang, and G. Dissanayake, “An invariant-ekf vins algorithm for improving consistency,” in *2017 IEEE/RSJ International Conference on Intelligent Robots and Systems (IROS)*. IEEE, 2017, pp. 1578–1585.

[90] Y. Song, Z. Zhang, J. Wu, Y. Wang, L. Zhao, and S. Huang, “A right invariant extended kalman filter for object based slam,” *IEEE Robotics and Automation Letters*, 2021.

[91] C. X. Guo and S. I. Roumeliotis, “Imu-rgbd camera 3d pose estimation and extrinsic calibration: Observability analysis and consistency improvement,” in *2013 IEEE International Conference on Robotics and Automation*. IEEE, 2013, pp. 2935–2942.

[92] D. Kim, S. Shin, and I. S. Kweon, “On-line initialization and extrinsic calibration of an inertial navigation system with a relative preintegration method on manifold,” *IEEE Transactions on Automation Science and Engineering*, vol. 15, no. 3, pp. 1272–1285, 2017.

[93] J. Svacha, J. Paulos, G. Loianno, and V. Kumar, “Imu-based inertia estimation for a quadrotor using newton-euler dynamics,” *IEEE Robotics and Automation Letters*, vol. 5, no. 3, pp. 3861–3867, 2020.

[94] H. Sommer, I. Gilitschenski, M. Bloesch, S. Weiss, R. Siegwart, and J. Nieto, “Why and how to avoid the flipped quaternion multiplication,” *Aerospace*, vol. 5, no. 3, p. 72, 2018.

[95] M. N. Duc, T. N. Trong, and Y. S. Xuan, “The quadrotor mav system using pid control,” in *2015 IEEE International Conference on Mechatronics and Automation (ICMA)*. IEEE, 2015, pp. 506–510.

[96] D. Abeywardena, Z. Wang, G. Dissanayake, S. L. Waslander, and S. Kodagoda, “Model-aided state estimation for quadrotor micro air vehicles amidst wind disturbances,” in *2014 IEEE/RSJ International Conference on Intelligent Robots and Systems*. IEEE, 2014, pp. 4813–4818.

[97] P. Petkov and T. Slavov, “Stochastic modeling of mems inertial sensors,” *Cybernetics and information technologies*, vol. 10, no. 2, pp. 31–40, 2010.

[98] M. Faessler, A. Franchi, and D. Scaramuzza, “Differential flatness of quadrotor dynamics subject to rotor drag for accurate tracking of high-speed trajectories,” *IEEE Robotics and Automation Letters*, vol. 3, no. 2, pp. 620–626, April 2018.

[99] J. Sola, “Quaternion kinematics for the error-state kalman filter,” *arXiv preprint arXiv:1711.02508*, 2017.

[100] N. Martínez and A. F. Villaverde, “Nonlinear observability algorithms with known and unknown inputs: analysis and implementation,” *Mathematics*, vol. 8, no. 11, p. 1876, 2020.

[101] M. Kok and T. B. Schön, “Magnetometer calibration using inertial sensors,” *IEEE Sensors Journal*, vol. 16, no. 14, pp. 5679–5689, 2016.

[102] Y. Wu, D. Zou, P. Liu, and W. Yu, "Dynamic magnetometer calibration and alignment to inertial sensors by kalman filtering," *IEEE Transactions on Control Systems Technology*, vol. 26, no. 2, pp. 716–723, 2017.

[103] M. A. Gomaa, O. De Silva, G. K. Mann, and R. G. Gosine, "Observability-constrained vins for mavs using interacting multiple model algorithm," *IEEE Transactions on Aerospace and Electronic Systems*, vol. 57, no. 3, pp. 1423–1442, 2020.